# Performance and optimization of analog and digital filtering algorithms for the Phase-II upgrade of the Hadronic End-Cap Calorimeter


**Alessandro Ambler**

Supervisor: Prof. Brigitte Vachon

Department of Physics
McGill University, Montreal

A thesis submitted to McGill University in partial fulfillment of the requirements of the degree of
*Master of Science*

April 2018

# Acknowledgements

All chapters in this thesis have been written by me, the main author. I would like to take the time to acknowledge the contributions of everybody who helped me in this endeavor.

First and foremost I would like to thank my supervisor, Professor Brigitte Vachon, for her guidance and support in all aspects of my research, not to mention the editing of this thesis.

I would also like to extend my gratitude to the members of the ATLAS group at McGill University whose help I could always count on. Special thanks to Dr. Andrée Robichaud-Véronneau whose help, patience and expertise in all things ATLAS related got me through my first few hundred lines of code.

The ATLAS experiment at CERN is a collaborative effort and all its members are to be thanked for its data analysis framework as well as the maintenance, construction and operation of the detector. Many thanks go to Nico Madysa from TU Dresden for all his help in maintaining, debugging and developing the AREUS code, Dr. Leonid Kurchaninov from TRIUMF for all his help with the modeling of the HEC's electronics and thermal noise, and finally Dr. Chris Anelli from UVic who supplied the minimum bias probability distribution functions discussed in Section 5.5.

Last but not least, I would like to thank my friends and family for their support.

# Abstract

The Large Hadron Collider (LHC) will be upgraded in 2024-26 to increase its beam intensity by a factor of up to 7 from its original design value. To cope with increased interaction rates and radiation exposure at this new High Luminosity LHC (HL-LHC), upgrades to multiple ATLAS detector subsystems are planned to take place alongside those to the LHC's accelerator chain. In this context, a re-design of the Hadronic End-Cap (HEC) calorimeter's electronic readout chain is required in order to maintain its energy reconstruction performance at the HL-LHC. The HEC readout electronics was implemented in a simulation framework capable of testing different analog filters and more complex digital signal processing algorithms. The expected degradation in energy resolution in the HEC at HL-LHC was estimated and optimization studies of different parameters of the HEC readout chain were carried out. Results have been used to make preliminary design decisions for the upgrade of the calorimeter readout electronics. Studies show that further improvements in the performance of the HEC energy reconstruction will have to come from new digital filtering algorithms that can better mitigate the effects of an increased interaction rate.

# Résumé

Le Grand Collisionneur de Hadrons (appelé en anglais "Large Hadron Collider" (LHC)) subira une mise à niveau importante en 2024-26 afin d'augmenter l'intensité de ses faisceaux de protons d'un facteur allant jusqu'à 7 par rapport à sa valeur de conception d'origine. Plusieurs mises à niveau des sous-systèmes du détecteur ATLAS sont prévues en parallèle à ceux de la chaîne d'accélération du LHC. Ceci sera nécéssaire afin de faire face à l'augmentation du taux d'interaction des protons et de l'exposition à la radiation qui auront lieu à ce nouveau LHC Haute Luminosité (HL-LHC). Dans ce contexte, une refonte de la chaîne de lecture électronique du calorimètre hadronique, ou "Hadronic End-Cap" (HEC), est nécessaire afin de maintenir sa performance de reconstruction énergétique au HL-LHC. L'implémentation de l'électronique de lecture du HEC dans un cadre de simulation capable de tester différents filtres analogiques et des algorithmes de traitement de signaux numériques plus complexes est réalisée. La dégradation attendue de la résolution énergétique du HEC au HL-LHC a été estimée et des études d'optimisation des différents paramètres de la chaîne de lecture du HEC ont été réalisées. Les résultats ont été utilisés pour prendre des décisions de conception préliminaires pour la mise à niveau de l'électronique de lecture du calorimètre. Les études démontrent que des améliorations supplémentaires de la performance de reconstruction énergétique du HEC devront provenir de nouveaux algorithmes de filtrage numérique qui pouront mieux atténuer les effets d'un taux d'interaction accru.

# Table of contents

# Chapter 1

# Introduction

The goal of this thesis is the simulation and optimization of the performance of the read-out electronics of the Hadronic End-Cap (HEC) calorimeter, a subsystem of the ATLAS detector (ATLAS is no longer an acronym, though it originally stood for "A Toroidal LHC ApparatuS"). The ATLAS experiment attempts to test and further our understanding of particle physics by analyzing proton-proton collisions at the Large Hadron Collider (LHC). The LHC is currently the world's largest and most powerful accelerator, colliding protons together at close to the speed of light. In 2024-26, the LHC will be upgraded to increase its beam intensity for a new era of data-taking, giving ATLAS sensitivity to rarer physics processes. At this new High Luminosity LHC (HL-LHC), the rate of proton-proton collisions will increase by almost an order of magnitude. This increase in collision rate will strain the current ATLAS detector readout while also increasing the radiation exposure to its detector subsystems beyond their design limits. Therefore, multiple upgrades to the ATLAS detector are planned to take place alongside those of the LHC. Among these upgrades will be the readout electronics of the HEC.

One of the design requirements for the new HEC electronic readout is that it provide the ability to achieve a detector performance comparable to that obtained with the current detector system, but under the much higher collision rate expected at the HL-LHC. To achieve this, both the analog and digital filtering algorithms of the HEC electronics readout are being re-designed. A fast and flexible simulation of the HEC readout electronics is therefore being developed to assess its performance and test new analog shaping circuits and more complex digital filtering algorithms that can help provide an adequate overall detector performance.

An overview of the Standard Model of particle physics and the need for a theory beyond the Standard Model is presented in Chapter 2. The experimental setup and upgrades of the LHC and ATLAS detector are presented in Chapter 3 with a particular focus on the HEC. The signal processing theory and techniques relevant to the simulation and results chapters are discussed in Chapter 4. The simulation of the HEC readout electronics is described in Chapter 5. The performance and optimization of various analog and digital filtering schemes of the HEC readout electronics is presented in Chapter 6. The results are summarized in Chapter 7 with an outlook on future research and development.

# Chapter 2

# The Standard Model of Particle Physics

The current theoretical framework used to describe all known elementary particles and the forces that govern their interactions, except gravity, is called the Standard Model (SM) of particle physics. This chapter provides a brief summary of the SM, just enough to understand the basic concepts, while also pointing to some of its crowning achievements in describing our observations of nature as well as some its shortcomings. A much more detailed description of the SM and of quantum field theory can be found in references [1–4].

## 2.1 Introduction

The SM is a relativistic and renormalizable quantum field theory in which point-like particles with no substructure are the excitations of quantum fields. These particles are defined by their mass and charge (which determines their coupling to a given force), and their spin (the quantum number associated to their angular momentum). These particles can be classified in two broad categories: fermions and boson. Fermions are the spin $^1/_2$ particles that make up matter and obey Fermi-Dirac statistics, while bosons are integer spin particles that obey Bose-Einstein statistics [2]. Bosons can be further divided into two categories, spin 1 gauge bosons that mediate the forces and a spin 0 Higgs boson. The existence of a Higgs boson is explained by the phenomena of electroweak symmetry breaking [5–10], which also explains the origin of all fermion masses (except neutrinos which are assumed in the SM to be massless). There are four gauge bosons: the massless photon and gluon that mediate the electromagnetic and strong force respectively, and the massive $W^{\pm}$ and $Z^0$ bosons that mediate the weak force. Of the fermions, there are six known flavors of quarks which participate in all three forces and six flavors of leptons that do not couple to the strong force. In addition, three of the

leptons flavors, called neutrinos, have no electric charge and thus also do not couple to the electromagnetic force. All these elementary particles and their properties are summarized in Figure 2.1. All charged particles are predicted and have been observed to have antiparticle counterparts, which have the same mass and spin but opposite charges.

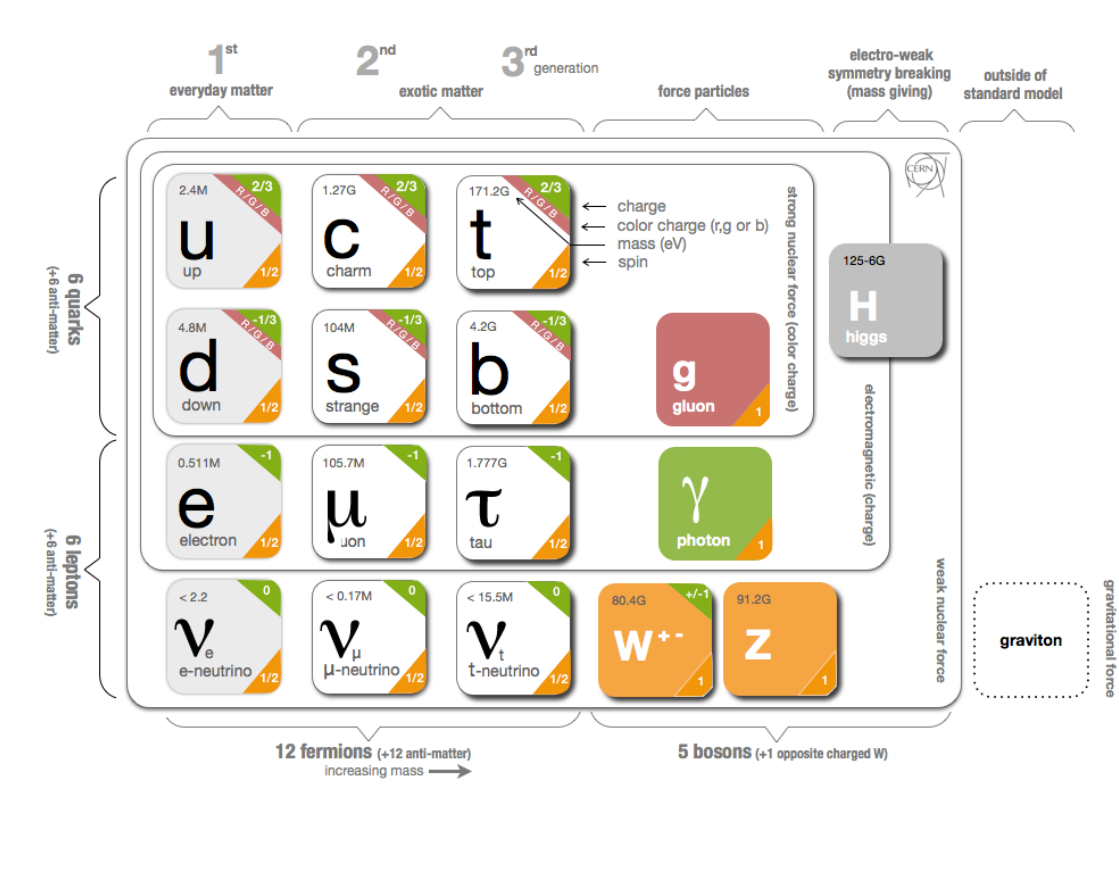


Fig. 2.1 Schematic diagram illustrating all the known types of elementary particles in nature [11]. Particles are grouped and arranged according to their properties.

The theory that describes the strong force is called Quantum Chromodynamics (QCD) (see [12] and references therein), owing to the fact that the charge carried by particles that interact via the strong force is called color. There are three different possible color charges referred to as red, green and blue, along with their three corresponding anti-color charges. Due to the non-Abelian nature of the group that describes strong interactions, gluons can self-interact [1]. This means that they carry the color charge of the interactions that they mediate. As a result, the strength of the force between colored particles increases with distance, as opposed to the electromagnetic and weak forces which decrease with distance. This leads to two very important consequences. The first is color confinement: colored

particles, i.e. quarks or gluons, cannot be found in isolation. Indeed, the energy stored in the gluon field between two colored particles increases as they are separated, leading to the spontaneous formation of quark-antiquark pairs from vacuum [1]. As such, quarks are only observed in colorless states, called color singlets. There are various ways of forming these color singlets. Colorless bound states of quarks are called hadrons. These are further classified into quark-antiquark bound states called mesons, and bound states of three quarks or three antiquarks called baryons. The masses of these bound states are not related in a straightforward way to the masses of the elementary particles that compose them because of their strong binding energies. When quarks or gluons are produced in a high energy environment they are observed as jets, which are streams of highly collimated particles, mainly hadronic in nature, originating from the initial colored particle. Another consequence of the non-Abelian nature of the strong force is asymptotic freedom. Due to the fact that the strong force becomes weaker at smaller distances, or equivalently at higher energies, quarks in a bound state can be considered as asymptotically free [1].

The predictions made by the SM and our knowledge of the properties and laws that govern the interactions of elementary particles are probed through the interaction of these particles with matter. The constituents of atomic matter are the most stable particles in the SM, the electron and the up and down quarks, as they are the lightest in their respective families. These particles make up all the atoms in the periodic table of elements. The atomic nucleus, composed of protons and neutrons, are in fact baryonic bound states of up ($u$) and down ($d$) quarks, $uud$ and $udd$ respectively. Neutrinos do not make up atomic matter as they only interact weakly with matter (they have no color or electric charge) and have an extremely small mass.

The current version of the SM was formulated in the 1970s to describe the cumulated knowledge of particle physics at the time. While the SM has many free parameters that have to be measured empirically, such as the masses of all the fermions, the Higgs mass and vacuum expectation value, and the gauge couplings of the three forces to name a few, it has made several important predictions that have since been confirmed by experiment. These include the discovery of the $\tau$ lepton in 1975 [13], the $W^{\pm}$ and $Z^0$ bosons in 1983 [14, 15], the top quark in 1995 [16] and the Higgs boson in 2012 [17, 18]. The predictions of the SM are still continuously being tested with no significant deviations observed as of yet. One of the testable predictions of the SM is the probability that a given interaction occurs, which

is expressed in terms the cross section[1] of a particular physics process. Figure 2.2 shows an overview of SM process cross section measurements with data collected by the ATLAS detector at the LHC. The ratios of the measurements to theory predictions are depicted as well, indicating that most measurements agree with calculations within one standard deviation.

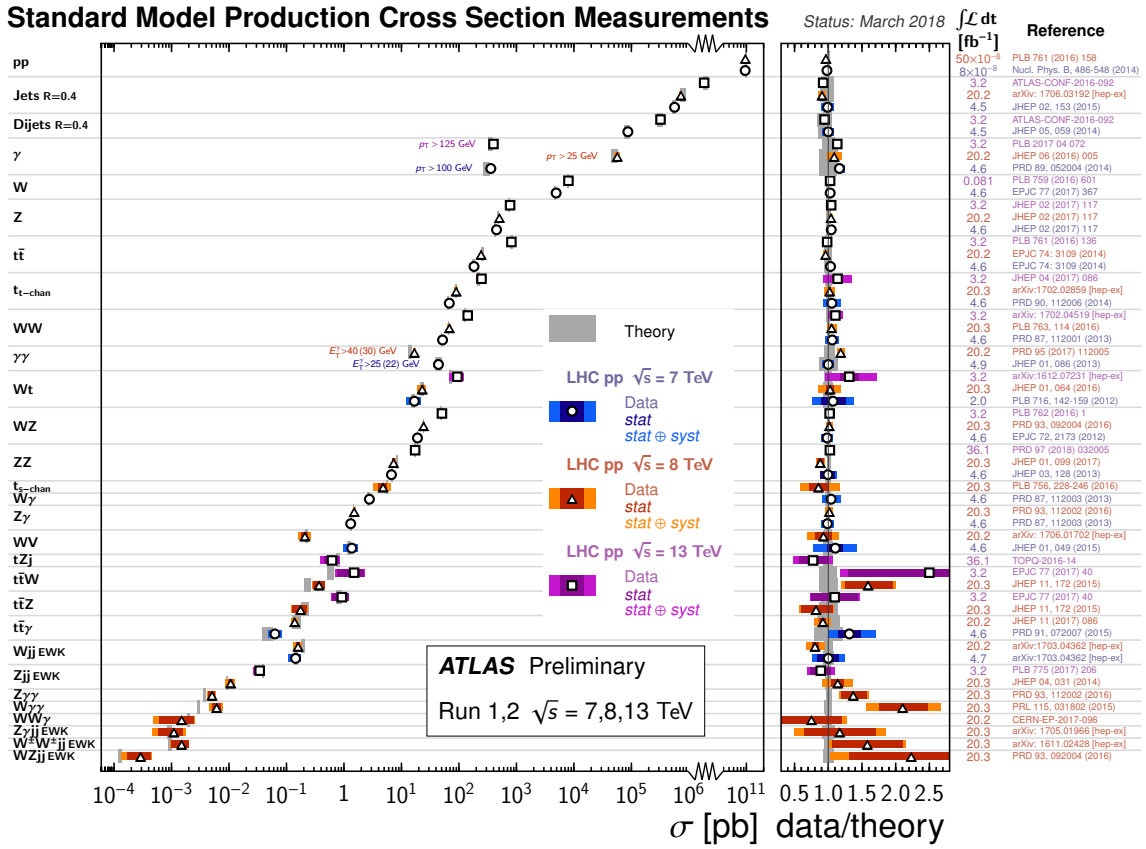


Fig. 2.2 Summary of total and fiducial production cross section measurements of several known physics processes measured by the ATLAS detector and their comparison with SM predictions [19].

## 2.2 Beyond the Standard Model

Though the SM has been a reliable model for describing elementary particles and their interactions, strong evidence suggests that it cannot be complete. For one, it does not include a description of gravity. It also has many free parameters that have to be fine tuned to fit

[1]The cross section is an area and is expressed in units of barns (symbol: b, equal to $10^{-28}\mathrm{m}^{-2}$).

observations. Many of our observations of nature also point to a theory beyond the SM (BSM). Here are a few selected examples:

- In the SM, neutrinos do not couple to the Higgs field and as such are predicted to have no mass. However, the oscillations between the three different types, or "flavors", of neutrinos has been observed [20], indicating that neutrinos are in fact massive. Indeed, these oscillations can be explained if neutrinos have mass eigenstates that are different from their flavor eigenstates. Mechanisms through which the neutrino can acquire mass are therefore required as extensions to the SM [21].

- There is now strong cosmological evidence that the energy content of the universe as well as its rate of expansion cannot be accounted for by the SM alone. Some theories point to a cold dark matter [22] and a repulsive dark energy [23] that would make up a significant portion of the energy content of our universe to account for these observations.

- Just as it was proven that the weak and electromagnetic forces are manifestations of the same gauge invariant theory that undergoes symmetry breaking, it is natural to think that a theory that unifies the electroweak and strong forces should exist. This is one of many other compelling arguments to think that a Grand Unified Theory (GUT) of the fundamental forces should encompass our SM of particle physics [24].

The ATLAS detector at the LHC attempts to probe our understanding of the SM and search of evidence of BSM physics. In order to provide the detectors on its ring an increased sensitivity to rare processes, the LHC will be upgraded to the HL-LHC. The ATLAS detector and its upgrade, planned to take place alongside that of the LHC, are detailed in the next chapter.

# Chapter 3

# Experimental Setup

In this chapter, an overview of the ATLAS experiment at the LHC is presented with a particular focus on the HEC calorimeter, a subsystem of the ATLAS Liquid Argon (LAr) Calorimeter. An overview of the upgrade schedules of the LHC and the ATLAS detector are also given, along with a description of the upgrade of the HEC readout electronics.

## 3.1 The Large Hadron Collider

The LHC [25] is a proton accelerator and collider located at CERN near Geneva, Switzerland. It is designed to accelerate and collide two counter-rotating particle beams traveling in two rings of 27 km in circumference located 40 to 170 m underground.

The LHC is the final acceleration stage of the CERN accelerator complex composed of several acceleration and injection stages (see Figure 3.1). Though the LHC is also designed to collide heavy ions such as lead, its main focus and that of the ATLAS detector is on the study of proton collisions. Before reaching the LHC, protons are first accelerated in the LINAC2 followed by the BOOSTER, the Proton Synchrotron (PS) and finally the Super Proton Synchrotron (SPS) where they reach an energy of 0.45 TeV. Two transfer tunnels are used to inject protons in bunches into the LHC which are then accelerated to 7 TeV, providing a center-of-mass energy of 14 TeV at the 4 interaction points (IPs). The LHC rings contain two separate beam pipes kept at ultrahigh vacuum. Here, the protons are guided by 1232 superconducting dipole magnets which bend the beams and 392 superconducting quadrupole magnets which focuses them. To achieve a beam energy of 7 TeV and keep the protons on their circular path, a dipole field of 8.33 T is required. Each beam pipe is also equipped with eight 400 MHz radio-frequency cavities which accelerate the protons and keep them

tightly bunched. These bunches contain up to $10^{11}$ protons which are made to collide 40 million times per second, or every 25 ns, giving the LHC its design instantaneous luminosity of $10^{34}$ cm$^{-2}$s$^{-1}$.

The instantaneous luminosity $\mathscr{L}$ is defined by the equation [26]:

$$\mathscr{L} = \frac{fN_1N_2}{4\pi\sigma_x\sigma_y}, \tag{3.1}$$

where $N_1$ and $N_2$ are the number of protons in the colliding bunches, $f = 40$ MHz is the frequency at which proton bunches are crossing, and $\sigma_x$ and $\sigma_y$ are the $x$ and $y$ components of the root mean square (RMS) of the spatial distribution of the particle bunches. The integrated luminosity is defined as:

$$L = \int \mathscr{L} \mathrm{d}t. \tag{3.2}$$

The number of interactions per bunch crossing (BC), $\mu$, is related to the instantaneous luminosity by:

$$\mu = \sigma_{tot} \cdot \Delta t_{BC} \cdot \mathscr{L}, \tag{3.3}$$

where $\Delta t_{BC} = 25$ ns is the time between bunch crossings and $\sigma_{tot}$ is the total[1] proton-proton cross section of interaction. The instantaneous luminosity delivered by the LHC changes in time as the protons interact and the number of protons in the bunches diminishes. After a certain amount of time, the proton beams are "dumped", or expelled from the LHC, and the process of injecting new protons into the LHC and accelerating them to 7 TeV is restarted. The period of proton collisions that takes place in between the acceleration and dumping of the proton beams is called a "fill". Over this period, $\mu$ is approximately Poisson distributed around its average $\langle\mu\rangle$.

The four main experiments that operate on the LHC ring at its four IPs are: ALICE, LHCb, ATLAS and CMS. ALICE [27] focuses on the analysis of lead-lead nuclei collisions to study the formation of quark-gluon plasmas. LHCb [28] is specialized in "b-physics" and aims at measuring charge-parity violation in the production and interactions of bottom quarks. ATLAS [29] and CMS [30] are both general-purpose detectors whose main objective was the discovery of the Higgs boson, which was accomplished in 2012 [17, 18]. The focus of these experiments is now on the measurement of the Higgs Boson's properties and the

[1] Elastic and inelastic.

study of BSM physics.

The first data-taking period, called Run 1, lasted from 2010 to 2012, starting with a center of mass energy of 7 TeV and ramping up to 8 TeV in 2012. The peak instantaneous luminosity achieved during Run 1 was approximately $8 \times 10^{33}$ cm$^{-2}$s$^{-1}$ [31]. Run 2 began in 2015 and is still ongoing, with the LHC delivering collisions at 13 TeV, not yet reaching its design goal of 14 TeV, while achieving a peak instantaneous luminosity, as measured by the ATLAS detector, of $21.4 \times 10^{33}$ cm$^{-2}$s$^{-1}$ [32], more than twice the LHC design value..

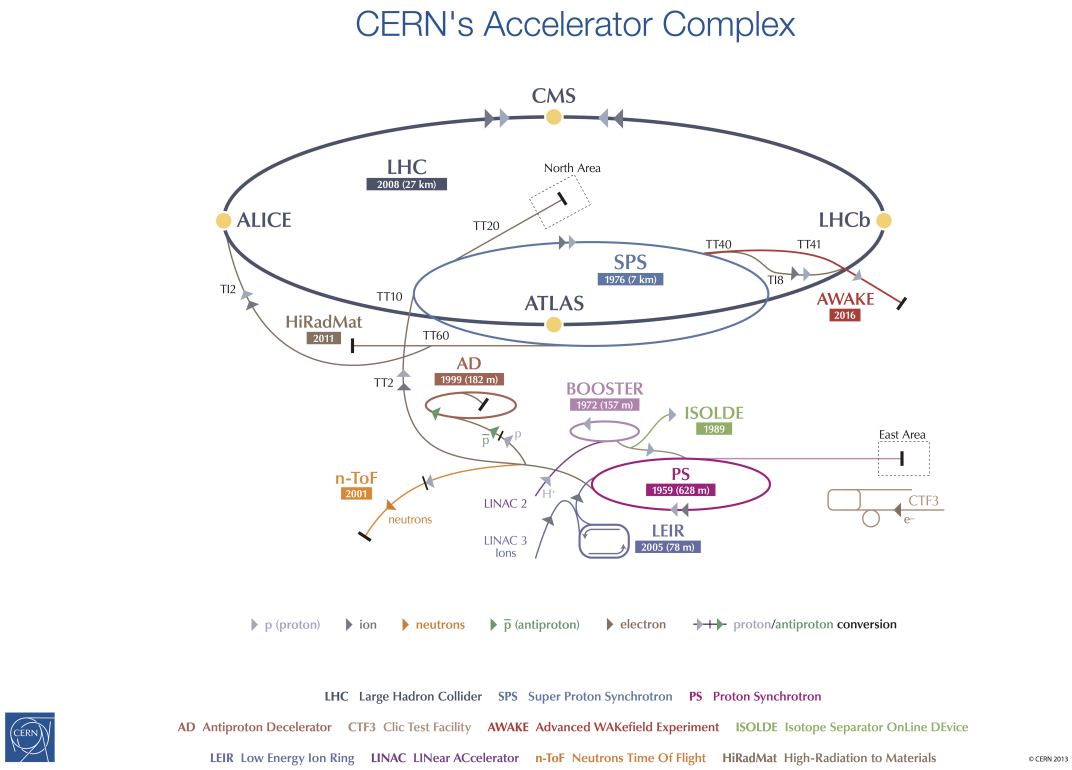


Fig. 3.1 Schematic diagram of the CERN accelerator complex [33].

## 3.2 The ATLAS detector

A schematic diagram of the ATLAS detector is shown in Figure 3.2. It has a cylindrical geometry around the beam pipe with the IP located at its center. It measures 44 m in length and 25 m in diameter and weighs almost 7000 tonnes. The ATLAS detector consists of multiple sub-detector layers arranged cylindrically around the beam pipe. Starting from

the IP and moving radially outwards, the ATLAS subsystems are the inner detector, the electromagnetic and hadronic calorimeters, and finally the muon spectrometer. The ATLAS detector also has a solenoid and three toroid magnet systems that bend the tracks of charged particles. An overview of its design is given in this section, with a particular focus on the HEC calorimeter in Section 3.2.3. More details about the ATLAS detector and its design can be found in reference [29].

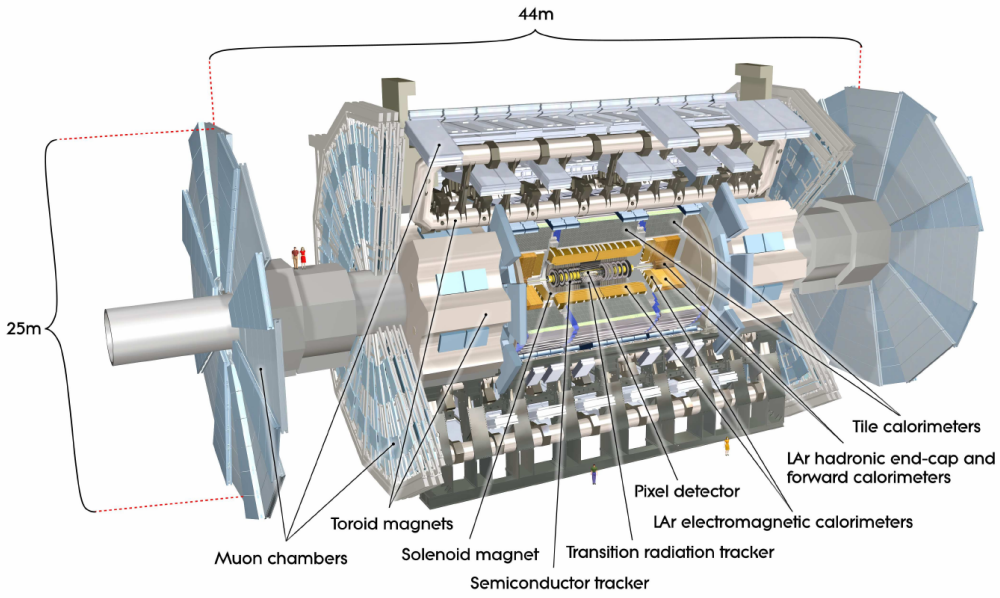


Fig. 3.2 Schematic diagram of the ATLAS detector and its sub-detectors [29].

### 3.2.1 Geometry and Conventions

The ATLAS coordinate system is defined with the IP at its origin. The $x$-axis points to the center of the LHC ring while the $y$-axis points perpendicularly upwards. The $z$-axis is formed by the cross-product of the $x$- and $y$-axis and is tangential to the beam pipe. This completes the Cartesian coordinate system.

The spherical coordinate system is more commonly used. It consists of the radial distance from the beam axis $R = \sqrt{x^2 + y^2}$ , the azimuthal angle $\phi$ which goes from $-\pi$ to $\pi$ and is measured from the $x$-axis in the $x-y$ plane, and the polar angle $\theta$ which ranges from 0 to $\pi$

and is measured from the $z$-axis. The polar angle is often replaced by the pseudorapidity $\eta$:

$$\eta = -\ln\left[\tan\left(\frac{\theta}{2}\right)\right] = \frac{1}{2}\ln\left(\frac{|\mathbf{p}| + p_z}{|\mathbf{p}| - p_z}\right), \tag{3.4}$$

where $p_z$ is the $z$ component of the 3-momentum vector $\mathbf{p}$. Pseudorapidity thus ranges from 0 in a direction perpendicular to the beam pipe to $\pm\infty$ in a direction along the beam pipe. Pseudorapidity is the approximation of rapidity in the limit where the momentum of a particle is much greater than its mass. This quantity is useful to describe the direction of outgoing particles produced in proton-proton collisions since a difference in rapidity $\Delta\eta$ is approximately invariant to a Lorentz boost in the $z$ direction [34].

Because the particles that interact at the IP are not the actual protons but their constituents (called "partons") which carry an unknown fraction of the proton's momentum, the center of mass energy of a collision in the lab frame is not known. However, since the total transverse energy of out-coming particles must be approximately zero, transverse quantities such as transverse momentum ($p_T = |\mathbf{p}| \cdot \sin(\theta)$) and transverse energy ($E_T = E \cdot \sin\theta$, where $E$ is the energy) are often used as they are invariant under Lorentz boosts along the $z$-axis. Missing $E_T$ refers to the transverse energy that was not detect by ATLAS and that would be required for the total $E_T$ to be zero.

### 3.2.2 Overview of the ATLAS Structure

As mentioned in the introduction to this section, the ATLAS detector is constructed in layers of different subsystems arranged cylindrically around the IP with a $\phi$ and $\pm z$ symmetry. An overview of each of the main detector sub-systems is presented in this subsection.

#### Inner Detector

The inner detector [35, 36] shown in Figure 3.3(a) is the sub-system closest to the IP. It covers the range in pseudorapidity of $|\eta| < 2.5$. Surrounding it is a solenoid magnet which is part of the magnet system shown in Figure 3.3(c) that provides a uniform 2 T magnetic field. This allows the inner detector to perform momentum measurements of charged particles in the transverse plane. The inner detector also provides measurements of the trajectories of charged particles, vertex reconstruction and electron identification capabilities.

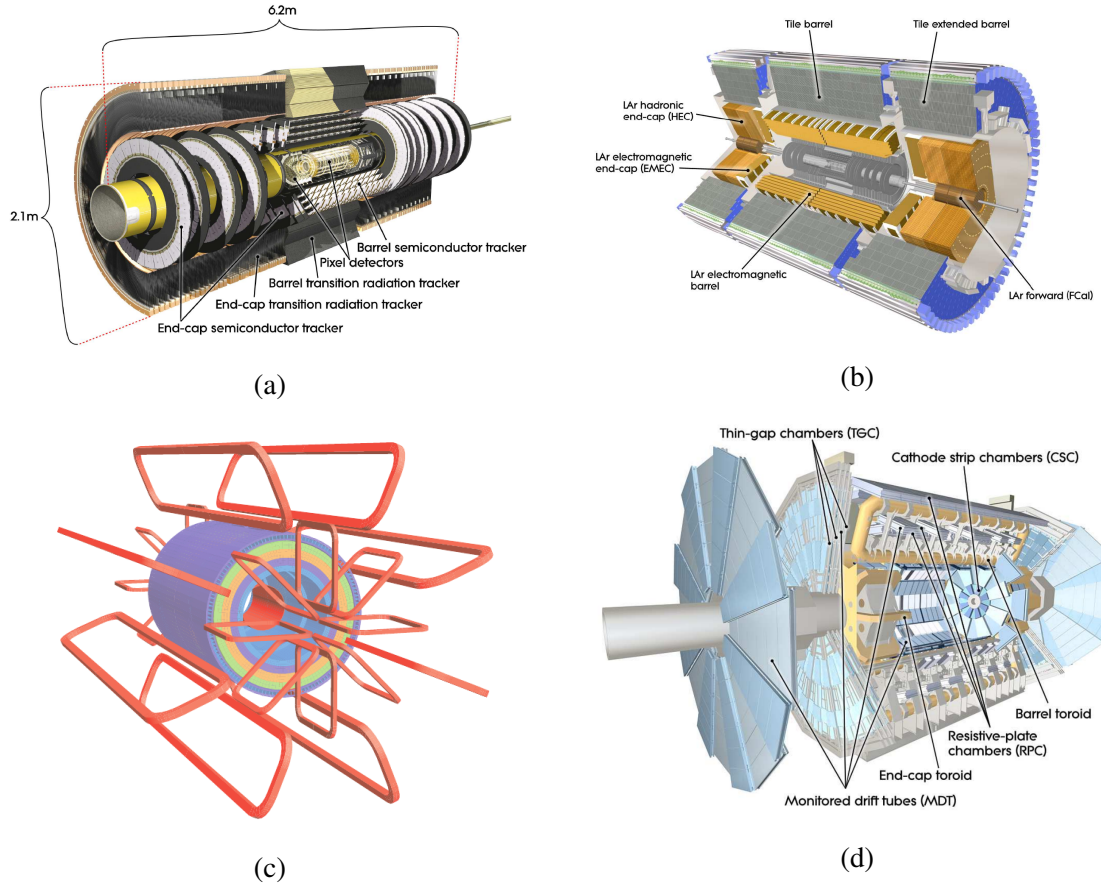


Fig. 3.3 Cutaway views of the different ATLAS sub-systems. Figure (a) shows the inner detector, (b) the calorimeter system, (c) the magnet system and (d) the muon spectrometer [29].

### Calorimeter System

A cutaway view of the calorimeter system, composed of the LAr [37] and Tile [38] calorimeters, is shown in Figure 3.3(b). The different calorimeter subsystems cover a total range of $|\eta| < 4.9$ using different detection techniques. The $\eta$ coverage of the electromagnetic calorimeter is matched to that of the inner detector and is finely granulated for precision measurements of photon and electron energies. The calorimeter must provide enough material so that the electromagnetic and hadronic showers induced by particles produced at the IP are contained and do not make it through to the muon spectrometer. The material, $|\eta|$ coverage and coarser granularity of the hadronic, forward and tile calorimeter subsystems are optimized to ensure good jet and missing $E_T$ resolution. The electromagnetic, hadronic and forward calorimeters are sampling calorimeters that use LAr as their active medium. They form the LAr calorimeter system. The tile calorimeter is also a sampling calorimeter but uses

scintillating tiles as its active medium.

### Muon Spectrometer

A cutaway view of the muon spectrometer [39] is shown in Figure 3.3(d). It uses the bending of charged particles in the magnetic field produced by the toroid magnets, shown in Figure 3.3(c), for momentum and charge measurements of muons. The muon spectrometer consists mainly of trajectory reconstruction chambers. It is the outermost sub-system of the ATLAS calorimeter, covering the region up to $|\eta| < 2.7$.

### Trigger and Data Acquisition System

The trigger system selects events with interesting physics signatures to reduce the rate of events which are recorded or "read-out". At a collision rate of 40 MHz, the bandwidth and memory required by the data acquisition system to record and store all events would be too large. The trigger system is composed of three successive levels: the hardware based Level-1 (L1) trigger [40], and the software based Level-2 (L2) trigger and event filter (EF) [41]. Each successive trigger level refines their criteria for accepting an event that passed the previous level. The L1 trigger reduces the event rate to 75 kHz at a fixed latency of 2.5 $\mu$s using limited information from the muon spectrometer and the calorimeter system. The data acquisition system receives and buffers the data that passes the L1 trigger at full detector granularity. This data is then sent to the L2 trigger and EF to further reduce the event rate to 200 Hz. Between Run 1 and Run 2, the trigger system was upgraded to attain an acceptance rate of 100 kHz in the L1 trigger. In addition, the L2 trigger and EF were consolidated into a single high level trigger (HLT) and upgraded to attain a final acceptance rate of up to 1 kHz [42].

An important set of trigger criteria in the context of this thesis is called the "minimum bias" trigger. The minimum bias trigger identifies events with a minimum set of criteria to ensure that this data has the least amount of bias. Given that a vast majority of events in the ATLAS detector come from the elastic collision of partons inside the protons, most events that pass this trigger come from elastic proton-proton collisions. In order to avoid saturating the detector readout bandwidth, only a small fraction of the events that pass this trigger are recorded.

### 3.2.3 The Hadronic End-Cap

The HEC is a sampling calorimeter with copper absorbers [37] and LAr as the active material. The HEC covers the range of $1.5 < |\eta| < 3.2$. It is located in the end-cap cryostat of the LAr calorimeter, as depicted in Figure 3.4, which keeps the argon in the detector liquid at approximately 87 K [43].

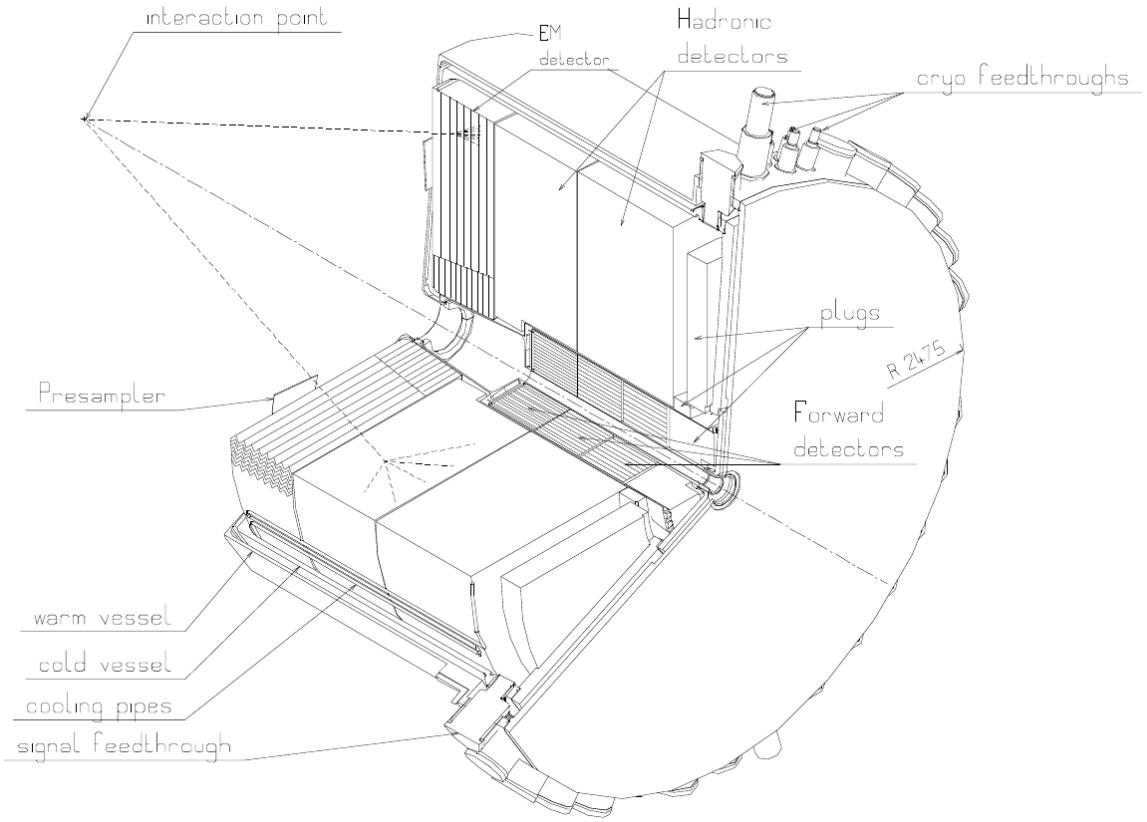


Fig. 3.4 View of one end-cap cryostat that houses the HEC, electromagnetic (EM) and forward calorimeters [37].

#### Working Principle

Before going into the details of its geometry and readout electronics, it is useful to understand the basic working principle of the HEC. Highly energetic charged and hadronic particles that interact with the copper plate absorbers induce particle showers. These particle showers ionize the active material between the plates and in the gaps. The gaps are instrumented with high voltage electrodes that the electrons will drift towards to be collected. Due to the

movement of charges in the gap, an electrical current is induced on a readout electrode with an amplitude and integral that is proportional to the amount of energy deposited in the gap. The amplitude and shape of the signal depends of the drift time of the electrons in the gap, which is on average 440 ns in the HEC [44]. The drift time in turn depends on the size of the LAr gap and the voltage on the electrodes. The effect of the much slower ions can be neglected. This can all be summarized in one compact formula for the amplitude of the current $I$ induced on the readout electrode:

$$I = \frac{Q_0}{\tau_{drift}} = N \cdot \frac{e}{\tau_{drift}} = \frac{E_{tot} \cdot f_{samp}}{W} \cdot \frac{e}{\tau_{drift}}, \tag{3.5}$$

where $Q_0$ is the total charge of the ionization electrons in the gap and $\tau_{drift}$ is the drift time of the electrons. The charge $Q_0$ can be expressed in terms of the number of free electrons $N$ and the electrical charge of the electron $e$. In turn, $N$ can be expressed in terms of the energy that the shower deposits in the absorber and in the active material $E_{tot}$, the sampling fraction $f_{samp}$ of the detector and the ionization energy of the LAr, $W = 23.6$ eV [45]. The sampling fraction is defined as the energy deposited in the LAr, $E_{vis}$ or visible energy, divided by $E_{tot}$:

$$f_{samp} = \frac{E_{vis}}{E_{tot}}. \tag{3.6}$$

In order to account for the recombination of the ions and electrons in the gap, a corrected value for $Q_0$ is used based on the Thomas-Imel model [46]:

$$Q_p = Q_0 \frac{\ln(1 + C/U)}{C/U}. \tag{3.7}$$

Here, $C = 0.80$ kV/cm is a constant while $U \approx 10$ kV/cm is the electric field in the gap. This amounts to a correction of about 3.8% to $Q_0$.

### Geometry

The geometry of the HEC is depicted in Figure 3.5. On the left, a slice of one "wedge" in the $R-\phi$ plane is depicted. A full "wheel" in the $R-\phi$ plane is made up of 32 of these wedges. On the right is depicted the top half of a slice in the $R-z$ plane. The HEC presents a $\phi$ symmetry around the beam pipe and a $\pm z$ symmetry because of the two almost identical detectors at each end of the ATLAS detector. The HEC is composed of two cylindrical wheels with two different sampling fractions, 5.5% in the front wheel (nearest to the IP) and

2.8% in the rear wheel where the thickness of the copper plates is doubled.

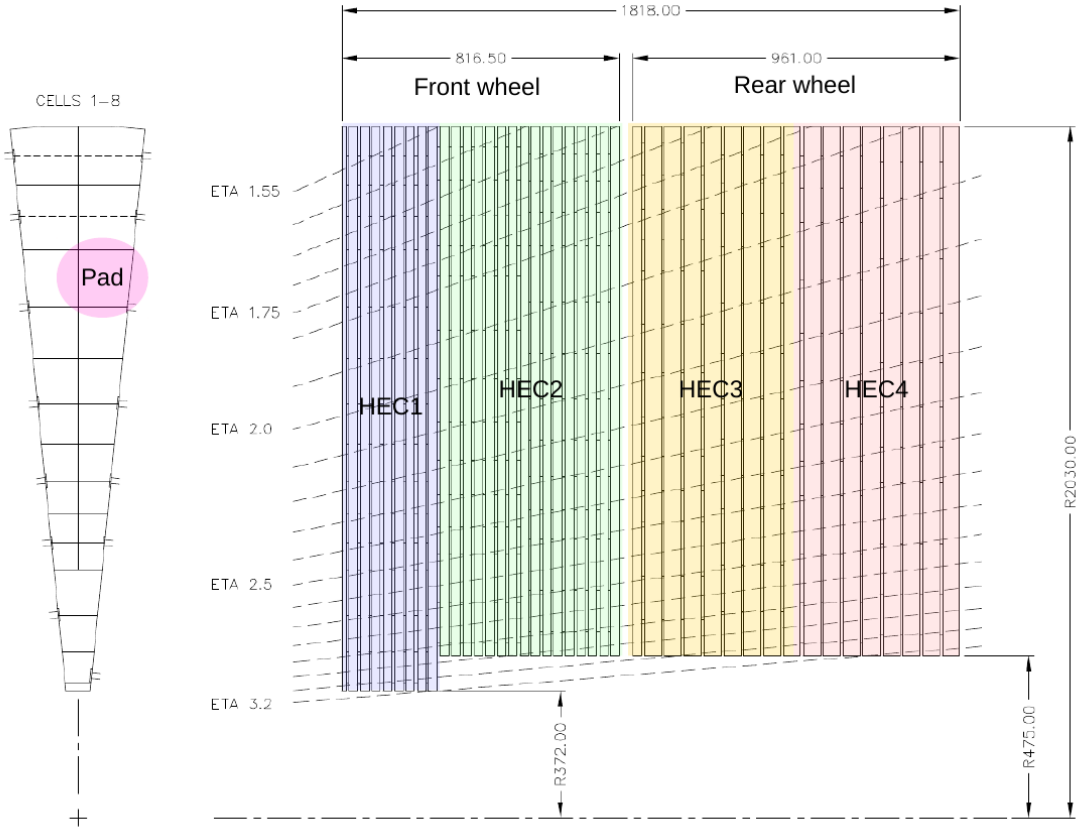


Fig. 3.5 Schematic view of the HEC [37]. The left side shows a slice in the $R-\phi$ plane, where 32 of these wedges make up a HEC wheel. The right shows the top half of a slice in the $R-z$ plane. ETA corresponds to the pseudorapidity ($\eta$) and the measurements are expressed in millimeters.

### Readout Structure

A readout cell, not to be confused with channel, is defined by the readout electrode in the LAr gap. A view of the electronics inside the gap can be seen in Figure 3.6. The gap consists of three parallel electrodes, the readout electrode being the central one with the other two serving as high voltage carriers that create the electric field in the gap. The copper plates on either side of the gap are grounded. The central electrodes are arranged in segmented pads in the $R-\phi$ plane as can be seen on the left side of Figure 3.5. From $1.5 < |\eta| < 2.5$, the pad structure has a granularity in $\eta \times \phi$ of $0.1 \times 0.1$, while from $2.5 < |\eta| < 3.2$ there is a

granularity of $0.2 \times 0.2$.

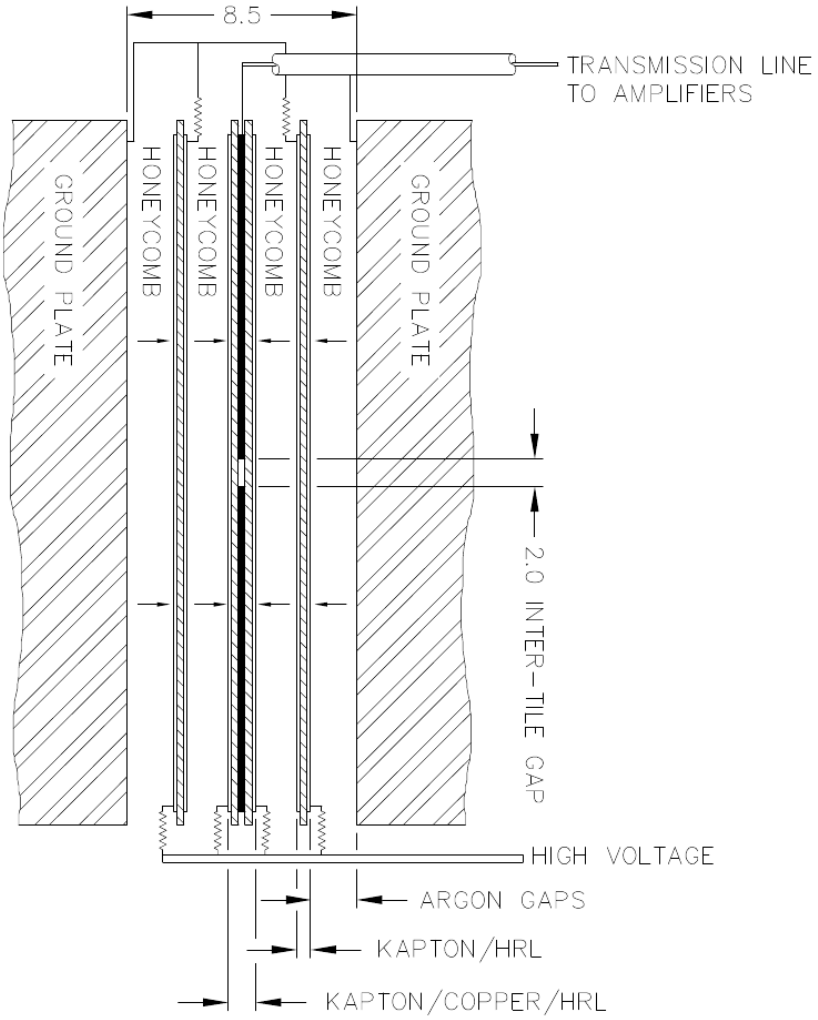


Fig. 3.6 Schematic diagram of the readout structure inside one of the LAr gaps in the $R-z$ plane [37].

The electric signal travels from the central electrodes in the gaps through the transmission lines to strip line connectors where the signals from two consecutive pads in the $z$ direction are passively summed.

The signals then travel to the preamplifying and summing boards (PSBs) on which 12 to 15 Gallium Arsenide (GaAs) application-specific integrated circuits (ASICs) [47] are mounted. The PSBs are located inside the cryostat in order to reduce thermal noise in the ASICs and are mounted on the outer radius of the HEC. In the ASIC, the signal from the strip line connectors are first individually preamplified.

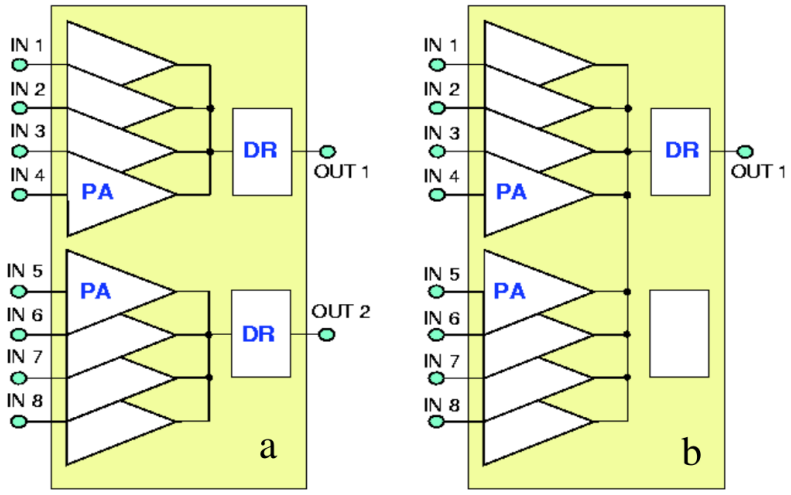


Fig. 3.7 Schematic diagram showing the two different GaAs ASIC preamplifier (PA) and driver (DR) summing schemes [48].

The outputs of the GaAs preamplifier ASICs correspond to the signals that form the HEC readout channels. There are two different summing schemes as can be seen in Figure 3.7. In both cases, the ASIC has 8 input signals which correspond to the signals from 16 consecutive cells. In the first scheme shown in Figure 3.7(a), 4 preamplifier outputs from 8 consecutive cells are summed, in which case the GaAs chip has two drivers which sum the signals forming two readout channels. In the second scheme shown in Figure 3.7(b), the GaAs chip has one driver which sums the signals from 8 preamplifier outputs or 16 consecutive cells forming a single readout channel. As can be seen in Figure 3.8, in the $z$ direction, the first 8 cells (4 GaAs preamp outputs) are summed to form a readout channel, the second channel is formed with the next 16 cells (8 GaAs preamp outputs) and the last two channels follow the same summing scheme as the first. The division of the channels in the $z$ direction can be seen in Figure 3.5, which shows which gaps are summed to form the HEC layers. Layers 1, 2, 3 and 4 correspond to the commonly used naming schemes HEC1, HEC2, HEC3 and HEC4 respectively. The cells are structured in such a way as to be approximately aligned in the $\eta$

direction as can be seen by the dashed lines of constant pseudo rapidity in Figure 3.5.

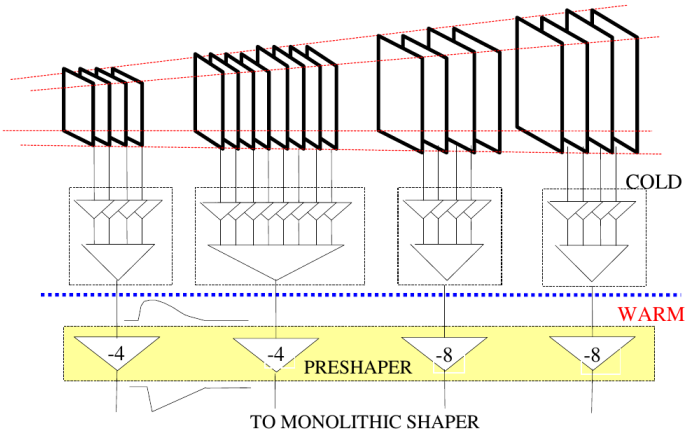


Fig. 3.8 Schematic diagram of the HEC summing and preshaping schemes [49].

The outputs from the PSBs are then sent through the feedthroughs of the cryostat (see Figure 3.4) to the front-end boards (FEBs) [51] located on the detector outside the cryostat. The FEB architecture common to the whole LAr calorimeter is depicted in Figure 3.9. The HEC is particular in that its signals are initially preamplified inside the cryostat, unlike signals from the EM and forward calorimeters, which are amplified by the "warm" preamplifiers installed on the FEB. The HEC GaAs preamplifiers have a different signal amplification and rise times than the warm preamplifiers. Thus, in order to match the linearity range of the shaper, a custom mezzanine called the preshaper is installed on the FEB instead of the warm preamplifier used to readout the electromagnetic and forward calorimeters signals. The function of the HEC preshaper is to apply additional amplification to the signal and invert its polarity with a negative gain (see Figure 3.8). The preshaper also compensates for the different sampling fractions in the front and rear wheels by amplifying signals from the rear wheel with a gain that is twice the gain in the front wheel. This ensures that the proportionality factor between the amplitude of the electric signal and the energy deposited in a channel is constant throughout the HEC. Finally, the HEC preshaper provides pole-zero cancellation (discussed in Chapter 5) to compensate for the widely varying capacitances of the LAr gaps.

After the preshaping stage, the signal is sent to the shaper (readout path) and to the layer summing boards (LSB) (trigger path). The LSB is the first stage in summing the HEC channels for the L1 trigger. From the LSB, the signal goes to the trigger driver boards (TDB)

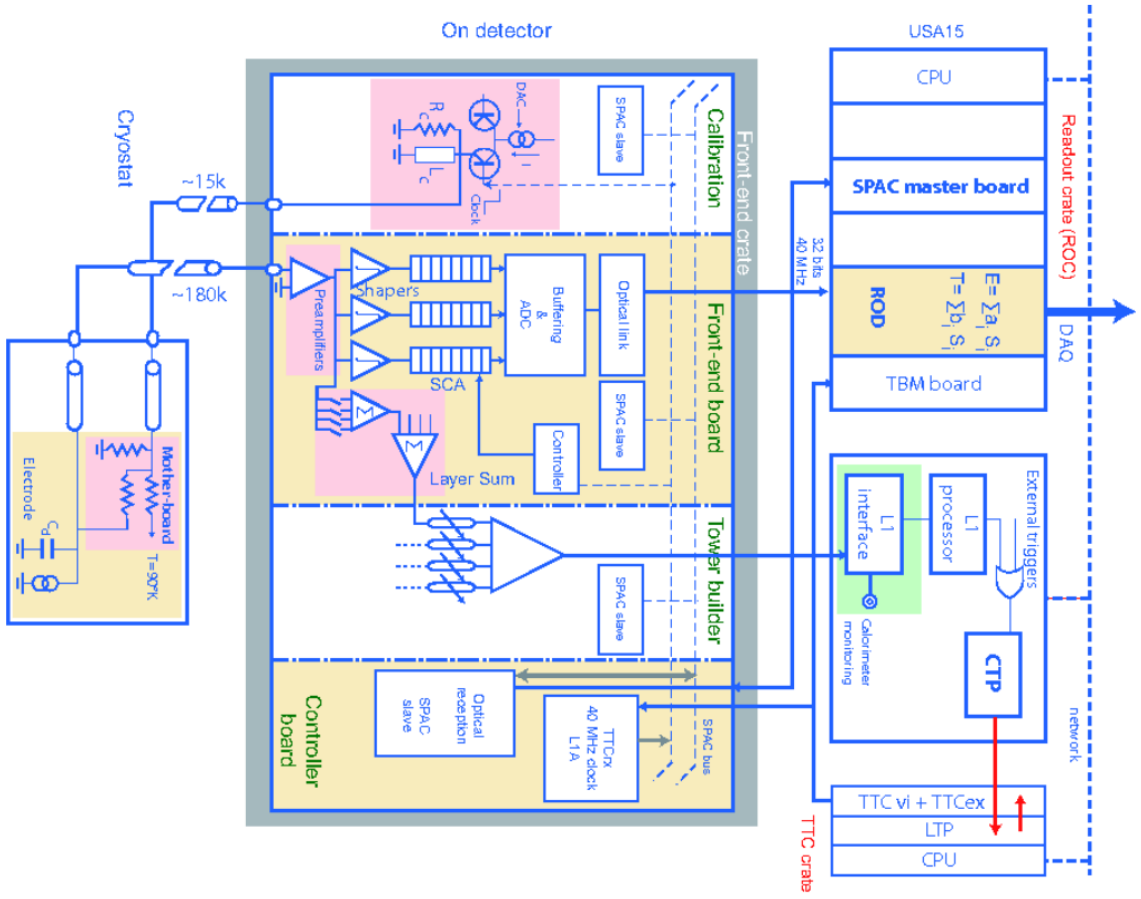


Fig. 3.9 Block diagram of the overall structure of the current LAr electronics. The electronics located inside the cryostat is shown in the left-most box. Not shown is the PSB unique to the HEC. The central box depicts the on-detector front-end electronics. In the case of the HEC FEBs, a preshaper mezzanine is installed in place of the preamplifier. The right-most box depicts the off-detector back-end electronics [50].

to finalize the summing of the first three segments of the HEC to form the so-called "trigger towers" sent to the L1 trigger. In the readout path, which is the focus of this thesis, the signals from the individual HEC channels are filtered in the shaper and further amplified at three different gains in parallel. These three different gain scales, low, medium and high, are used to extend the dynamic range of the ADC. The shaped signals at all three gain stages are then sampled at the LHC bunch crossing frequency of 40 MHz by the switched-capacitor arrays (SCAs). These store the analog signal samples for the duration of the L1 trigger latency. If an event is accepted by the L1 trigger, the optimal gain scale is selected and the first 5 samples of the signal in the SCA are digitized by a 12-bit analog to digital converter (ADC). With the

use of three gain scales, an effective dynamic range of 17-bits is achieved [51].

The digital signal from the FEB is then formatted, multiplexed, and sent through an optical cable at 1.6 Gbps to the readout driver (ROD) in the back-end electronics [50] as shown in Figure 3.9. The FEBs are mounted on the rim of the detector and thus are exposed to large doses of radiation, meaning stringent requirements have to be put on their radiation hardness. This is also why much of the more complex computation is done in the back-end, far from the detector, by central processing units (CPUs), digital signal processors (DSPs) and field-programmable gate arrays (FPGAs). It is in the DSPs in the ROD where the energy and timing information of energy deposits are extracted from the 5 digitized samples that are sent to the back-end. This is done with digital signal processing algorithms which will be detailed further in Chapter 5. The results are then sent to the data acquisition system.

#### The HEC Pulse Shape

The normalized ionization signal and resulting shaped and sampled pulses of the HEC are shown in Figure 3.10. The ionization of the LAr in the gap induces a triangular signal with a sharp rise time $\mathcal{O}(1\ ns)$ and a linear decay back to baseline over a period of ≈450 ns, corresponding to the drift time of the electrons in the gap. The ionization signal is filtered by the front-end electronics where it is shaped by the $CR-(RC)^2$ shaper circuit giving a bipolar pulse shape. This pulse shape is sampled at intervals of 25 ns, which is the interval between bunch crossings at the LHC.

#### Thermal Noise

Noise in the form of the thermal agitation of charge carriers (Johnson-Nyquist noise [52, 53]) in the HEC electronics distorts the pulse shape, aggravating the task of energy and timing reconstruction in the RODs. Thermal noise in the HEC can be modeled by a series voltage source and a parallel current source before the HEC preamplifiers (this is further detailed in Chapter 5) as the main source of thermal noise in the HEC electronics comes from the GaAs ASICs in the cryostat. Analog filtering with the $CR-(RC)^2$ shaper and the choice of the shaper time constants ($\tau_s = RC = CR$) which determines the width of the HEC pulse shape are crucial for minimizing the impact of thermal noise on the reconstruction of the original pulse amplitude and time. The "Fourier uncertainty theorem" [54], analogous to the

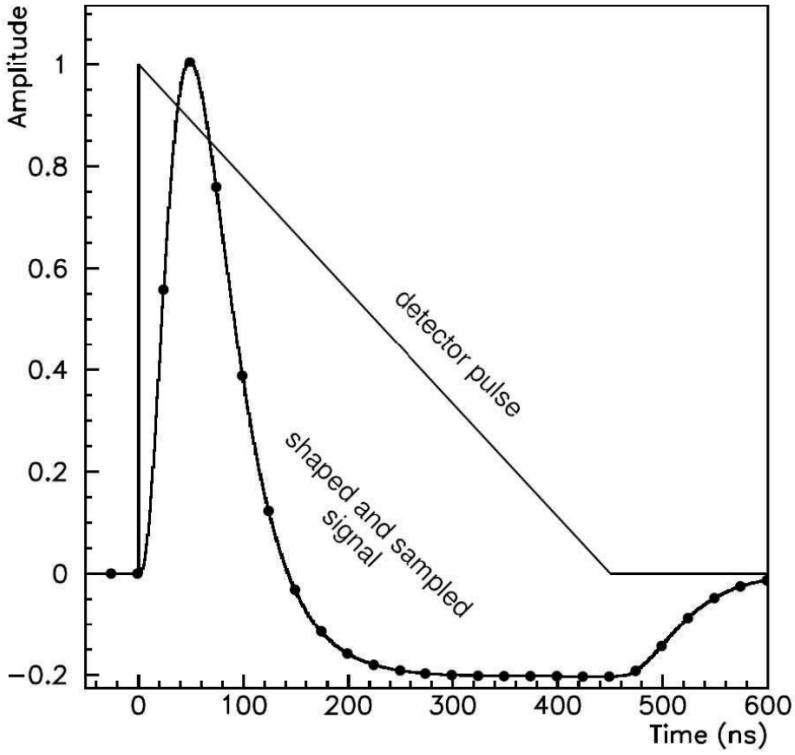


Fig. 3.10 Plot of the triangular ionization signal in the LAr calorimeter along with the shaped and sampled pulse shapes [37].

uncertainty principle in quantum physics, states that a broad pulse shape in the time domain has a correspondingly narrow frequency spectrum, and vice versa. Given that the thermal noise frequency spectrum extends to high frequencies, a broader signal pulse shape in the time domain achieved with longer shaper time constants helps reduce the effects of thermal noise. The effect of thermal noise on the digitized pulse shape can be seen in Figure 3.11(a).

### Pileup Noise

There are two types of pileup noise to be considered in the HEC readout chain. One is in-time pileup, where secondary particles from multiple proton-proton interactions in the same bunch crossing deposit energy in a HEC channel. If one of these energy deposits comes from a physically interesting event, or signal of interest, the energy deposits from the other events can be considered as noise. The impact of in-time pileup is to produce a larger amount of ionization in the detector, which is then reconstructed as corresponding to a higher amount of energy than the energy deposited only from the physics signal of interest. This is due to the fact that the energy deposited in a HEC channel is proportional to the amplitude of

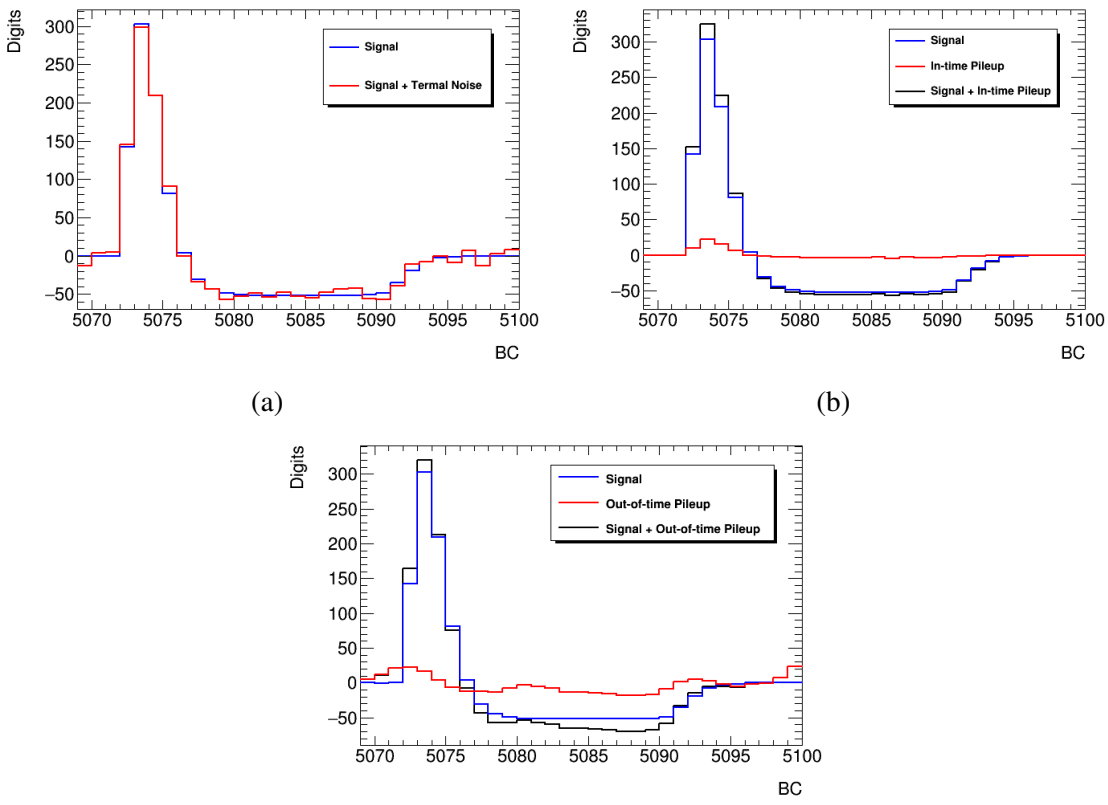


Fig. 3.11 Example of a digitized pulse shape in the HEC with and without (a) thermal noise, (b) in-time pileup and (c) out-of-time pileup. The x axis represent time expressed in units of bunch crossing number, and the y-axis represents the digitized value of the sampled analog pulse.

i

the electronic signal and that the full signal processing chain is linear. The effect of in-time pile-up on the HEC sampled pulse shape can be seen in Figure 3.11(b).

The other type of pileup noise is out-of-time pileup. Given that the HEC pulse shape returns to baseline after approximately 450 ns, it extends over several bunch crossings. If energy is deposited in a readout channel less than 450 ns before or 125 ns after a signal of interest, the two time-shifted pulse shapes will overlap in time. This will result in a distorted signal pulse shape as can be seen in Figure 3.11(c). In the context of this thesis, the use of the term pileup noise refers to the combination of in-time and out-of-time pileup. The impact of pile-up noise on the measurement of energy in a readout channel can be reduced using a narrow pulse shape, since a narrow pulse shape reduces the overlap between a signal of

interest and out-of-time pileup.

The time integral of a bipolar pulse shape, such as the one used in the HEC readout, is zero. This has the advantage of ensuring that the baseline of the calorimeter signal does not shift as a function of time with the presence of out-of-time pile-up.

The amount of pileup noise is highly dependent on the instantaneous luminosity of the LHC and in turn the average number of interactions per bunch crossing, $\langle\mu\rangle$. The optimization of the pulse shape width is thus highly dependent on $\langle\mu\rangle$. The width of the HEC pulse shape, described by its peaking time $\Delta\tau_p$, is determined by the choice of shaping circuit and time constants. While having a narrower pulse shape reduces pileup noise, it increases thermal noise. This is depicted in Figure 3.12 for two different instantaneous luminosities, $\mathscr{L} = 10^{34}$ cm$^{-2}$s$^{-1}$, which is the nominal instantaneous luminosity at the LHC, and a lower value of $\mathscr{L} = 10^{33}$ cm$^{-2}$s$^{-1}$. The amount of pileup noise increases with instantaneous luminosity and longer peaking times, while the amount of thermal noise increases with shorter peaking times.

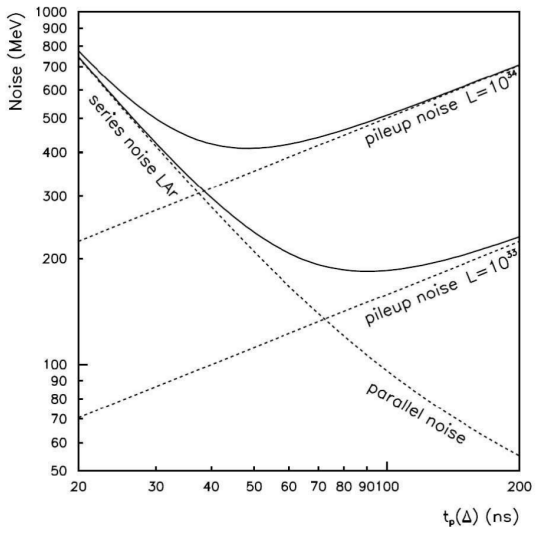


Fig. 3.12 Plot of the thermal noise (series and parallel components), pileup noise and total noise versus pulse shape peaking time $t_p(\Delta)$ in the LAr calorimeter for two different instantaneous luminosities, $\mathscr{L} = 10^{34}$ cm$^{-2}$s$^{-1}$ and $\mathscr{L} = 10^{33}$ cm$^{-2}$s$^{-1}$ [37].

Pileup noise in the HEC increases significantly at higher $\eta$ and in the forward layers. The large range of capacitances in the HEC cells leads to thermal noise that varies significantly throughout the detector as well. It is therefore impractical to optimize the shaping time of the

analog filtering, which is implemented in hardware, on a channel by channel basis and for a given instantaneous luminosity. Therefore, digital filtering of the signal is done in the ROD for further mitigation of different sources of noise. Digital filters, as described in Chapter 5, can easily be calibrated to the pileup and thermal noise conditions of each channel in order to minimize their impact on the final reconstructed energy.

#### Energy Resolution

The energy resolution of a sampling calorimeter can be parametrized by the following equation [37]:

$$\frac{\sigma_E}{E} = \frac{a}{\sqrt{E}} \oplus \frac{b}{E} \oplus c, \tag{3.8}$$

where $E$ is the energy measured, $\sigma_E$ is the RMS of the error on an energy measurement, the sampling term $a$ depends on the construction of the calorimeter, the noise term $b$ depends on the total noise in its readout chain and $c$ is a constant term that relies on the precise knowledge of its geometry and electronic pulse shape. The focus of this thesis is on the noise term $b$, which includes thermal noise in the electronics, pileup noise and digitization noise introduced when converting the analog samples of the pulse shape to digital values.

## 3.3 Upgrade Plans of the LHC and the ATLAS Detector

### 3.3.1 The High Luminosity LHC

The LHC was designed to collide protons at a center of mass energy of 14 TeV and to deliver a total integrated luminosity of 300 fb$^{-1}$ to each of its two general purpose detectors, ATLAS and CMS. The run schedule of the LHC is depicted in Figure 3.13. To date it has reached 13 TeV and delivered around 100 fb$^{-1}$ of data. Along with the discovery of the Higgs boson, the data collected at the LHC since 2010 has lead to some of the most accurate measurements of SM parameters and stringent limits on BSM parameters. However, the statistical gain of running the LHC without any significant increase in instantaneous luminosity after 2020 will be marginal, requiring 10 years to halve the statistical error on measurements. In order to extend its discovery potential and maintain the statistical gain of running over a longer period of time, the LHC will be upgraded during the 2024-2026 Long Shutdown 3 (LS3). This upgrade will result in an instantaneous luminosity approximately 5 to 7 times larger than its original design value, making it possible to record a total of 3000 to 4000 fb$^{-1}$ of collision data over the following 10 to 12 years [55].

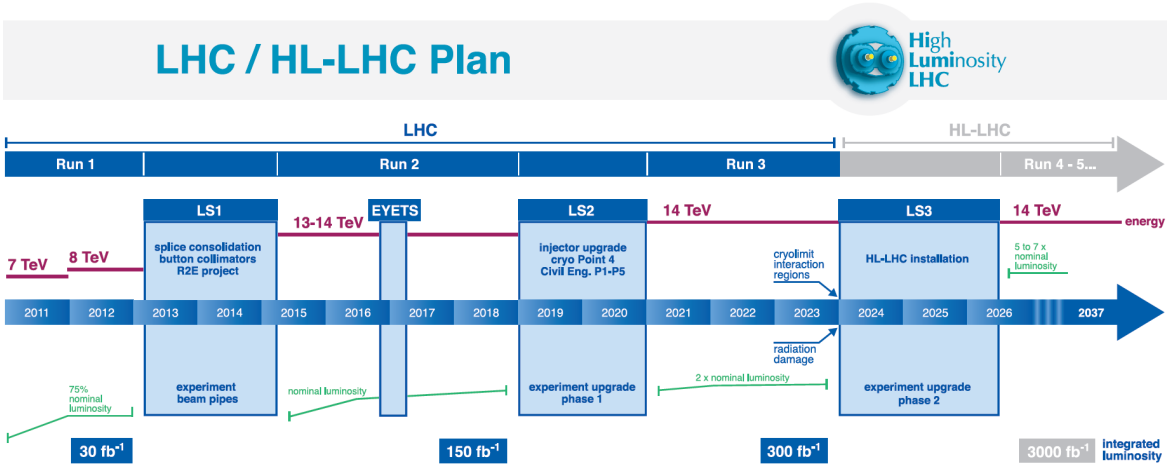


Fig. 3.13 Upgrade schedule of the LHC [56]. Shown are the center-of-mass collision energies in red, the instantaneous luminosity in green, the integrated luminosity in $\text{fb}^{-1}$, the Long Shutdown periods LS1, LS2 and LS3, and the Extended Year-End Technical Stop (EYETS).

### 3.3.2 The upgrade schedule of the ATLAS detector

The upgrades to the LHC will give ATLAS a greater sensitivity to measurements that tackle the most relevant questions in particle physics. These include the existence of supersymmetry, the nature of dark matter and the existence of extra dimensions as well as the properties of the newly discovered Higgs boson. Access to 3000 $\text{fb}^{-1}$ of collision data would allow an improvement on the precision of the production cross section times branching ratio for most Higgs boson decay modes of a factor of two or three. It would also allow for the measurement of rarer processes, such as the Higgs decay to two muons and evidence of Higgs self-coupling (with CMS and ATLAS results combined). With conservative estimates, the mass reach of searches for new particles will increase by approximately 50% [57].

In order to achieve adequate physics performance at a higher instantaneous luminosity and cope with the effects of long term radiation exposure due to the increased integrated luminosity, the ATLAS detector has multiple upgrades planned to take place along side those of the LHC. These upgrades take place during the Long Shutdown periods LS1, LS2 and LS3.

#### Phase-II Upgrades

The so-called Phase-II upgrades of the ATLAS detector will take place during LS3. A significant upgrade to the trigger and data acquisition system is planned. The L1 trigger will be split into two levels, an L0 level, which will retain the same topological algorithms

introduced during Phase-I [58], and a new L1 trigger which will have a greater latency budget and have access to the full granularity of information from the calorimeter system. This will require a complete overhaul of the calorimeter front- and back-end electronics. More information can be found in reference [59].

### 3.3.3 Upgrade Plans for the HEC

As discussed in the previous subsection, substantial upgrades to the electronics of the LAr calorimeter are planned for the Phase-II upgrade of the ATLAS detector. In this subsection, the planned upgrades to the HEC electronics are detailed and motivated.

#### Phase-II Upgrades

The HEC and its on-detector electronics were designed to sustain up to 10 years of operation at the LHC, or the equivalent of 700 to 1000 $fb^{-1}$ of integrated luminosity [60]. However, the HL-LHC is expected to deliver 3000 to 4000 $fb^{-1}$ over the 10 to 12 years following LS3. This means that the on-detector electronics will be exposed to radiation doses far beyond their design specifications. Radiation tests done on the cold electronics (PSBs) inside the cryostat show that they should remain operational at HL-LHC for an integrated luminosity of 4000 $fb^{-1}$ [61]. The linearity range of the preamplifiers has a maximum current of 250 $\mu$A [62]. A study was done in the context of this thesis to show that the higher proton-proton interaction rate at the HL-LHC should not significantly affect the the linearity of the HEC signal in the preamplifiers (see Appendix A).

New readout electronics will be designed based on a free-running architecture where analog readout is continuously sampled and digitized in the front-end. The information will then be sent to a digital back-end system at 40 MHz where the data will be buffered awaiting a trigger accept signal. Figure 3.14 shows a schematic diagram of the proposed implementation of this free-running readout architecture. New components that are being designed for the phase-II upgrade are shown inside a blue frame boxes. The new FEBs (i.e. FEB2) will replace the existing front-end boards mounted on-detector and will therefore be radiation hard. The digital back-end electronics, the LAr Signal Processor (LASP), will be located off-detector.

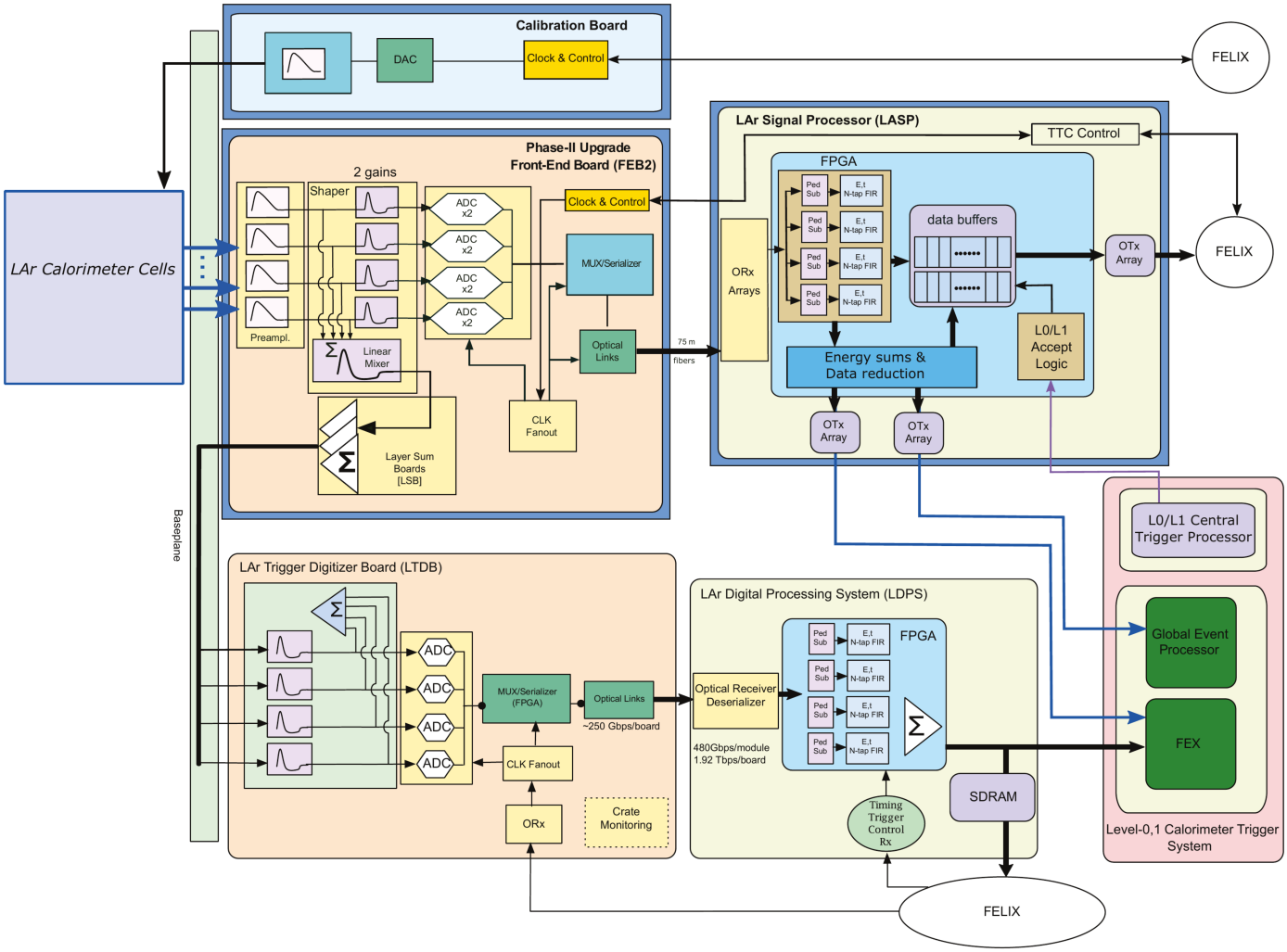


Fig. 3.14 Block diagram of the upgraded Phase-II LAr electronics [63]. Systems installed during LS3 are shown in blue wide frame boxes. The LTDB and DPS are components of the Phase-1 upgrade [64].

The average number of interactions per bunch crossings $\langle\mu\rangle$ at the HL-LHC is expected to reach 140 to 200 [59]. For comparison, Figure 3.15 shows the distribution of $\langle\mu\rangle$ measured during previous data taking years at the LHC, ranging from $\langle\mu\rangle = 9.1$ to $\langle\mu\rangle = 37.8$. Therefore, during HL-LHC running, the increase in pileup noise in the HEC electronic readout chain will be significant. It is thus imperative that the energy reconstruction performance of the HEC's signal processing chain at the HL-LHC be evaluated.

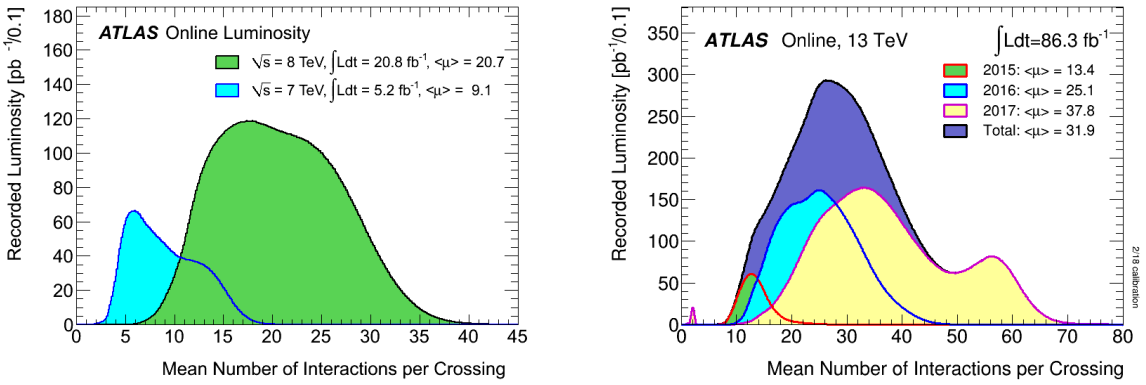


(a) (b)

Fig. 3.15 Average number of interactions per bunch crossing in previous data taking years during (a) Run 1 [31] and (b) Run 2 [32] at the ATLAS detector.

The topic of this dissertation is the optimization of the HEC readout parameters for HL-LHC running. The impact of several different readout parameters are explored. At the HL-LHC, the use of a bipolar pulse shape is expected to still be optimal due to its zero integral which keeps the baseline shift in the readout at zero. However, the number of integration stages in the $CR-(RC)^2$ shaper and their time constants need to be optimized for the pileup environment of the HL-LHC. Sampling the signal at 80 MHz, or twice the current sampling rate, would allow more information to be extracted from the pulse shape and is expected to improve the performance of digital filtering algorithms. Though extra bandwidth would be required to send more samples to the back-end electronics, in case of a significant improvement in performance this choice might be justified. The use of different digital filtering algorithms capable of mitigating the increased effects of out-of-time pileup at the HL-LHC must be tested along with the current digital filter already in use.

# Chapter 4

# Signal Processing

In this chapter, the basics of analog and digital signal processing are introduced. These concepts will be important in the simulation and interpretation of results presented in Chapters 5 and 6 respectively. A comprehensive summary of these subjects can be found in references [65–67].

The work presented in this thesis focuses on the electric signals coming from the HEC channels, such as voltage or current, as a function of time. As such, continuous-time signals will be referred to as analog signals in this chapter. In the HEC, the ionization signal goes through some analog filtering in order to cut out undesirable frequencies coming from sources of noise, such as thermal noise in the electronic circuits and pileup noise. The signal is then sampled in the time domain by an ADC at a given sampling rate, giving a discrete-time signal. Ideally, the signal is sampled in equally spaced time intervals. The clock jitter of the ADC introduces some uncertainty on the time at which the signal was sampled, though this effect shall be neglected in what follows. The quantization of the amplitude of this discrete time signal according to the ADC's number of bits and least significant bit (lsb) is treated separately. This will introduce some quantization noise depending on the way in which the ADC approximates the amplitude of the signal, which is by rounding in the HEC's ADC. The ADC's effective number of bits (ENOB) accounts for the thermal noise introduced by the ADC itself. Once a discrete-time signal is quantized, it becomes a digital signal and can be digitally filtered. Often, the digital signal processing of the signal is treated in the discrete-time domain as it greatly simplifies the calculations. The quantization of the signal can be treated separately. The digital filtering of the signal can be implemented in hardware in a number of different ways, such as through the use of DSPs in the HEC's signal

processing chain. The internal and output precisions of the signal in the hardware in which the filter is implemented shall be neglected in what follows.

## 4.1 Analog Signals and Filters

An analog filter $\mathscr{F}$ in its broadest sense is simply a system that takes an analog signal $x_a(t)$ as input, manipulates it in some way, and outputs an analog signal $y_a(t)$:

$$x_a(t) \xrightarrow{\mathscr{F}} y_a(t). \tag{4.1}$$

Analog signals can also be expressed in the frequency domain with its Fourier transform. The Fourier transform decomposes the signal into the frequencies that make it up:

$$X_a(\omega) = \int_{-\infty}^{\infty} x_a(t) e^{-i\omega t} dt. \tag{4.2}$$

Here, $X_a(\omega)$ denotes the Fourier transform of $x_a(t)$ and $\omega$ denotes the angular frequency, which is related to frequency by $\omega = 2\pi f$. The original signal as a function of time $x_a(t)$ can be recovered from its Fourier transform $X_a(\omega)$ by taking its inverse Fourier transform:

$$x_a(t) = \int_{-\infty}^{\infty} X_a(\omega) e^{i\omega t} d\omega. \tag{4.3}$$

In most cases, and in fact for the rest of this thesis, only Linear and Time Invariant (LTI) filters will be considered, as their mathematical properties make them significantly easier to manipulate. Any circuit composed of linear components, such as resistors, capacitors and inductors, forms an LTI system.

A linear system will have an output that is linearly related to the input. If input $x_{a1}(t)$ to a linear filter $\mathscr{F}$ has output $y_{a1}(t)$, input $x_{a2}(t)$ has output $y_{a2}(t)$, and $a_1$ and $a_2$ are constants, the system obeys the following relation:

$$a_1 x_{a1}(t) + a_2 x_{a2}(t) \xrightarrow{\mathscr{F}} a_1 y_{a1}(t) + a_2 y_{a2}(t). \tag{4.4}$$

A time invariant filter that outputs $y_a(t)$ for input $x_a(t)$ will output $y_a(t+\Delta t)$ if its input $x_a(t+\Delta t)$ is shifted in time by $\Delta t$.

An LTI system has the property that it can be described by a single function called its impulse response, denoted $h_a(t)$. As the name implies, $h_a(t)$ is the output of the system for an input impulse $\delta(t)$, were $\delta(t)$ is the Dirac delta function. The output $y_a(t)$ of an LTI system in response to any input $x_a(t)$ can be computed by the convolution of its impulse response with the input:

$$y_a(t) = (x_a * h_a)(t) = \int_{-\infty}^{\infty} x_a(t)h_a(t-\tau)d\tau. \tag{4.5}$$

In the frequency domain, this operation is greatly simplified due to the convolution theorem [67], which states that a convolution in time-domain of two signals corresponds to the pointwise product of their Fourier transforms:

$$Y_a(\omega) = H_a(\omega)X_a(\omega). \tag{4.6}$$

Analog LTI systems are typically described by linear constant-coefficient differential equations with zero initial conditions ($y(0) = 0$ and $t \geq 0$) relating input to output, in which case the Laplace transform is used to study the system's properties. Instead of in the frequency domain, the Laplace transform represents a signal in the s-plane, where $s = \sigma + i\omega$, $\sigma$ is a real number and $\omega$ is the angular frequency. The Laplace transform of $x_a(t)$ is defined as:

$$X_a(s) = \int_{-\infty}^{\infty} x_a(t)e^{-st}dt \tag{4.7}$$

and, similarly to the Fourier transform, $x_a(t)$ can be recovered from $X_a(s)$ via the inverse Laplace transform. Its formal definition will not be discussed here as it can usually be computed through the use of the partial fraction expansion method, which will be discussed later in this section, and the use of tables with common time domain functions and their Laplace transform. If a signal's Fourier transform exists, it can be found from its Laplace transform by the relation:

$$X_a(\omega) = X_a(s = i\omega). \tag{4.8}$$

It has an analogous version of the convolution theorem, allowing for the description of the input/output relations of LTI systems in the s-plane with the pointwise product of the Laplace transforms of the input and impulse response of the system:

$$Y_a(s) = H_a(s)X_a(s). \tag{4.9}$$

Common examples of analog filters are high-pass RC and low-pass CR circuits. For a CR circuit, as depicted in Figure 4.1(a), the following input/output relation for voltage are found based on Kirchhoff's circuit laws [68]:

$$v_{in}(t) = RC\frac{dv_{out}(t)}{dt} + v_{out}(t). \tag{4.10}$$

Taking the Laplace transform and noting that $\mathscr{L}\{\frac{dv_{out}}{dt}\} = sV_{out}(s) - v_{in}(t=0)$, where $\mathscr{L}$ is

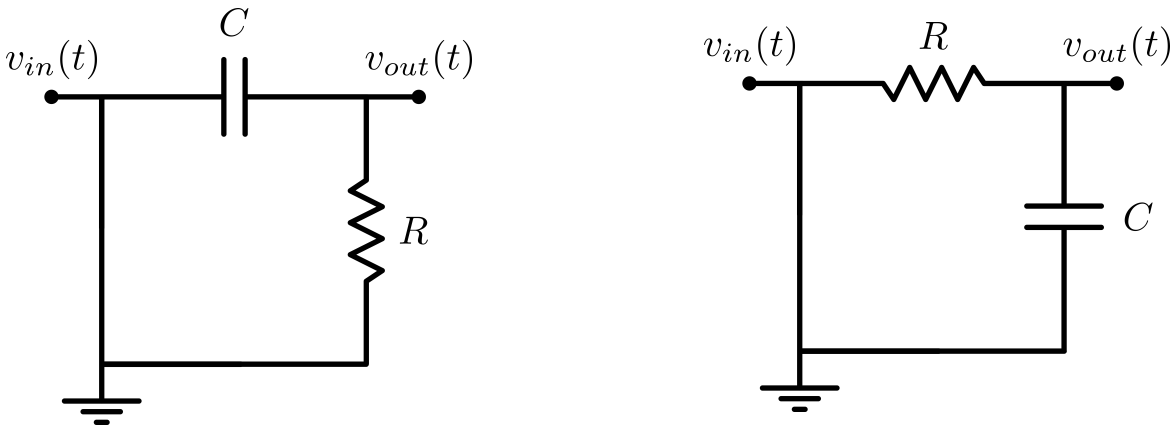


Fig. 4.1 Circuit diagrams of a (a) CR and (b) RC circuit.

the Laplace transform operator, the transfer function of the circuit in the s-plane is simply:

$$H(s) = \frac{V_{out}(s)}{V_{in}(s)} = \frac{1}{1 + RC \cdot s}, \tag{4.11}$$

where it is assumed that $v_{in}(0) = 0$. Similarly, the transfer function of the RC circuit as depicted in Figure 4.1(b) is given by:

$$H(s) = \frac{V_{out}(s)}{V_{in}(s)} = \frac{RC \cdot s}{1 + RC \cdot s}. \tag{4.12}$$

Figure 4.2 shows the Bode plots for these two circuits, indicating their magnitude response as a function of frequency. In both cases, the frequency $f = \frac{1}{2\pi RC}$ corresponds to the "cut-off" frequency where the circuit attenuates the input by -3 dB. The "time constant" of the circuits is $\tau = RC$. It corresponds to the time it takes to charge the capacitor through the resistor from 0 to $(1 - e^{-1})V_0$ with an applied DC voltage $V_0$, or discharge from $V_0$ to $e^{-1}V_0$ from an initial voltage across the capacitor $V_0$.

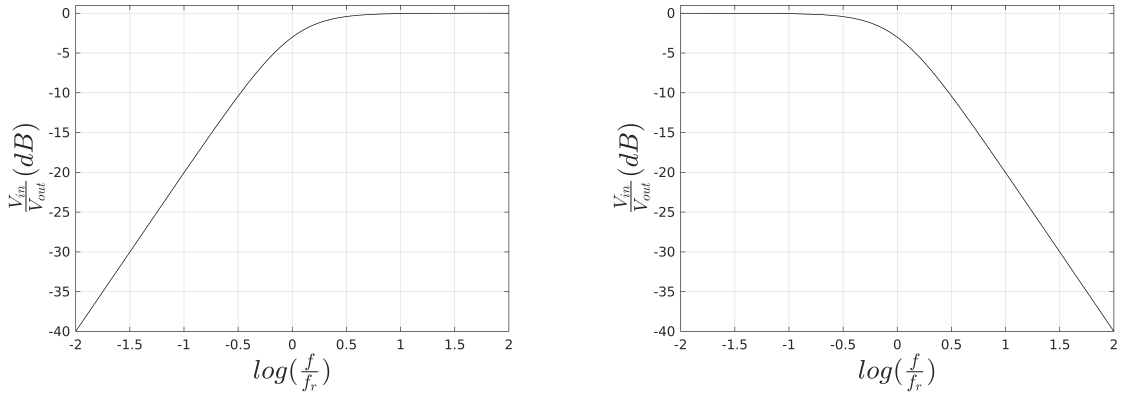


(a) (b)

Fig. 4.2 Bode plots of a (a) CR and (b) RC circuit.

An LTI system that is described by linear constant-coefficient differential equations can be written as a rational function in terms of poles and zeros in the s-plane in the form:

$$H(s) = C \cdot \frac{\prod_{k=1}^{M}(1+\tau z_k \cdot s)}{\prod_{l=1}^{N}(1+\tau p_l \cdot s)}, \tag{4.13}$$

where the $N$ poles appear at $s = -\frac{1}{\tau p_l}$ and the $M$ zeros appear at $s = -\frac{1}{\tau z_k}$. Here, $\tau p_l$ are the time constants that lead to poles, $\tau z_k$ are the time constants that lead to zeros and $C$ is some unitless constant. If a system's transfer function can be written in the form of equation 4.13, the method of partial fraction expansion can be used to recover its time domain response. If $M < N$, i.e. the number of poles is greater than the number of zeros, the transfer function from equation 4.13 can be written in this form:

$$H(s) = \sum_{k=1}^{N} \frac{A_k}{1+\tau p_k \cdot s}, \tag{4.14}$$

where the coefficients $A_k$ can be found analytically. In order to do so, the right side of equation 4.14 is first set to a common denominator. Then, the numerators of the right hand sides of equations 4.13 and 4.14 are expressed as a power series of $s$. Lastly, these two numerators are equated, with each polynomial coefficient, i.e. the coefficients multiplying every power of $s$, being equal. The result is a set of $N$ equations, the unknowns being the $N$ coefficients $A_k$.

Once the function is expressed in the form of equation 4.14, finding the inverse Laplace transform is simply done by using the relation:

$$\mathscr{L}\left\{\frac{1}{1+\tau p_k \cdot s}\right\} = \frac{1}{\tau p_k} e^{-\frac{t}{\tau p_k}}. \tag{4.15}$$

Note that this method of recovering the time domain response of a filter does not work if one of the poles is repeated. This can be avoided by changing the value of any repeated pole by an arbitrarily small value since, in practice (or in a non ideal system), the time constants of a physical system are not identical.

## 4.2 Discrete-Time Signals

Discrete-time signals are represented mathematically by a sequence of equally-spaced numbers or "samples". The amplitude of discrete-time signals is continuous, i.e. it can take on any value, as opposed to a digital signal which most often refers to an analog signal that has been sampled by an ADC.

The $n^{\text{th}}$ number in a sequence $x$ is denoted $x[n]$, where $n \in \mathbb{Z}$ is an integer. A discrete-time system or filter $\mathscr{T}$ is defined mathematically as a transformation that maps an input sequence with values $x[n]$ to an output sequence with values $y[n]$:

$$x[n] \xrightarrow{\mathscr{T}} y[n]. \tag{4.16}$$

As with analog signals, a discrete-time sequence can be represented in the frequency domain through the use of a Fourier transform. The discrete-time Fourier transform (DTFT) of a discrete-time signal corresponds to its frequency domain representation. The DTFT $X(\omega)$ is related to its discrete-time signal $x[n]$ by:

$$X(\omega) = \frac{1}{2\pi} \sum_{n=-\infty}^{\infty} x[n] e^{-i\omega n}. \tag{4.17}$$

The time domain signal can be recovered with the inverse DTFT (IDTFT):

$$x[n] = \int_{-\pi}^{\pi} X(\omega) e^{i\omega n}. \tag{4.18}$$

Again, only the class of discrete-time systems which are LTI will be considered. These systems obey the superposition principle:

$$a_1 x_1[n] + a_2 x_2[n] \xrightarrow{\mathscr{T}} a_1 y_1[n] + b_2 y_2[n], \tag{4.19}$$

if $y_1[n]$ and $y_2[n]$ are the responses of a system $\mathscr{T}$ to inputs $x_1[n]$ and $x_2[n]$ respectively and $a_1$ and $a_2$ are arbitrary constants. A time-invariant system, who's response to an input $x[n]$ is $y[n]$, will output $y[n-n_0]$ with input $x[n-n_0]$ for any time shift $n_0$.

As for analog systems, discrete-time LTI systems are completely characterized by their impulse responses, the response of the system to an impulse $\delta[n]$, where $\delta[n]$ is the delta Kronecker. The output $y[n]$ of this system can be computed by the discrete-time convolution of an input x[n] with its impulse response:

$$y[n] = (x * h)[n] = \sum_{m=-\infty}^{\infty} x[m]h[n-m]. \tag{4.20}$$

In the frequency domain, the convolution becomes a pointwise product:

$$Y(\omega) = H(\omega)X(\omega) \tag{4.21}$$

analogously to the convolution theorem for analog systems [65].

Discrete-time LTI systems can be further classified into two important categories: infinite impulse response (IIR) and finite impulse response (FIR) systems.

Typically, discrete-time filters are realized through the implementation of linear constant-coefficient difference equations of the form:

$$\sum_{k=0}^{M-1} a_k y[n-k] = \sum_{k=0}^{N-1} b_k x[n-k]. \tag{4.22}$$

Rearranging the terms gives:

$$y[n] = \sum_{k=0}^{N-1} b_k x[n-k] - \frac{1}{a_0} \sum_{k=1}^{M-1} a_k y[n-k]. \tag{4.23}$$

This is the general form of an IIR filter. It depends on previous outputs of the filter and thus has to store the $M$ previous filter outputs in addition to the $N$ samples stored from the input. The impulse response of the filter, as the name implies, is infinite and does not go to zero, though can asymptotically. This can make its implementation tricky as this feedback loop can lead to instability in the sense that a bounded input:

$$|x[n]| \leq B_x < \infty \quad \text{for all } n \tag{4.24}$$

does not necessarily lead to a bounded output:

$$|y[n]| \leq B_y < \infty \quad \text{for all } n. \tag{4.25}$$

Here, $B_x$ and $B_y$ are positive finite values. When referring to the stability of a filter, it is in the bounded-input, bounded-output sense.

A FIR filter has the simpler form:

$$y[n] = \sum_{k=0}^{N-1} b_k x[n-k]. \tag{4.26}$$

It continuously applies a set of $N$ coefficients $b_k$ to the input and can thus be considered as a continuous weighted average of the $N$ previous samples of the input. FIR filters are intrinsically stable and have a memory of duration $N$. The filter is entirely determined by its set of coefficients which define its transfer function. The distinction between different FIR filters lies in the filter depth (i.e. the length of its transfer function) and the way their coefficients are calculated.

## 4.3 Sampling of Analog Signals

Discrete-time signals are most often a representation of a sampled analog signal. A discrete-time signal $x[n]$ is then obtained by uniformly sampling an analog signal $x(t)$ according to the relation:

$$x[n] = x_a(nT_s - t_0), \tag{4.27}$$

where $T_s$ is the sampling period, or the time between samples. The sampling frequency is denoted $f_s = \frac{1}{T_s}$. A time offset $t_0$ can be introduced while sampling an analog signal. When sampling with an ADC, this is referred to as the phase shift of the ADC, $\phi_{ADC}$, which is

expressed in seconds. The operation of sampling an analog signal is not usually invertible. However, in the case of a band-limited analog signal $x_a(t)$ with:

$$X_a(\omega) = 0 \qquad \text{for } |\omega| \geq 2\pi \cdot f_N, \tag{4.28}$$

the Nyquist-Shannon sampling theorem [69, 70] states that $x(t)$ is uniquely determined by its samples $x[n] = x_a(nT_s - t_0)$ if:

$$f_s = \frac{1}{T_s} \geq 2 \cdot f_N. \tag{4.29}$$

The frequency $f_N$ is referred to as the "Nyquist frequency" and $2f_N$ as the "Nyquist rate". Thus, if a signal's frequency is band-limited and is sampled at the Nyquist rate, which is twice the Nyquist frequency of the signal, the original analog signal can be recovered from the resulting discrete-time signal.

When a band-limited signal is sampled under the Nyquist rate, aliasing of the signal occurs. This is mathematically described in frequency domain by the relationship between the sampled signal $X(\omega)$ and the analog signal $X_a(\omega)$:

$$X(\omega) = \frac{1}{T_s} \sum_{k=-\infty}^{\infty} X_a(\omega - 2\pi k). \tag{4.30}$$

The frequency spectrum of the sampled sequence is an infinite sum of shifted copies, called aliases, of the frequency spectrum of the analog signal. The copies are shifted by integer values $k$ of the sampling frequency. An example of aliasing occurring when sampling below the Nyquist rate of an analog signal is shown in Figure 4.3. If $f_s \leq 2f_N$, the shifted copies of the original signal frequency spectrum will overlap and distort the frequency spectrum of the sampled sequence.

## 4.4 Random Signals

Before introducing the quantization of a discrete-time signal, the basic properties of both analog and discrete-time random signals are described. These concepts also apply to the analysis of thermal and pileup noise in the HEC.

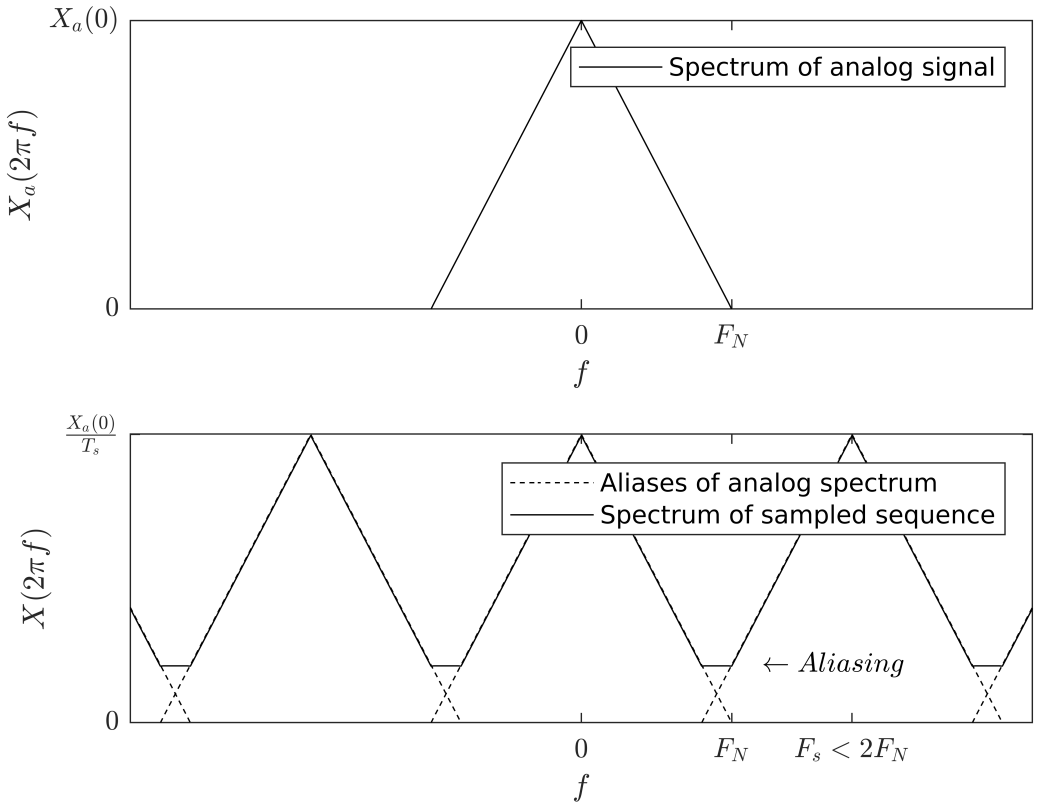


Fig. 4.3 Example of aliasing occurring when the sampling rate $F_s$ of a band-limited analog signal is below the Nyquist rate $2F_N$.

### 4.4.1 Analog Signals

Let $\mathbf{x}_a(t)$ be an analog random process, specifically a random variable measured at time $t$. These random variables are characterized by a set of probability distribution functions (PDFs) that may also be a function of time:

$$P(\mathbf{x}_a(t),t) = \text{Probability}[\mathbf{x}_a(t) \leq x_a(t)], \tag{4.31}$$

where $x_a(t)$ denotes a particular value of $\mathbf{x}_a(t)$. The mean or expectation value of the process $\mathbf{x}_a(t)$, denoted $\eta_{\mathbf{x}_a}(t)$, is:

$$E\{\mathbf{x}_a(t)\} = \eta_{\mathbf{x}_a}(t). \tag{4.32}$$

The autocorrelation function of this process, denoted by $R_{\mathbf{x}_a}(t_1,t_2)$, is the expectation value of the product $\mathbf{x}_a(t_1)\mathbf{x}_a^*(t_2)$:

$$E\{\mathbf{x}_a(t_1)\mathbf{x}_a^*(t_2)\} = R_{\mathbf{x}_a}(t_1,t_2), \tag{4.33}$$

where the symbol $^*$ denotes the complex conjugate. A stochastic process is in a wide-sense stationary, hereby referred to simply as stationary, if the random variable's mean does not depend on time and if its autocorrelation function depends only on the time difference $\tau = t_1 - t_2$. The random processes that contribute to the noise in the HEC signal chain, such as thermal, quantization and pileup noise, are or can be approximated as stationary. As a consequence, for a stationary process:

$$E\{\mathbf{x}_a(t)\} = \eta_{\mathbf{x}_a}(t) = \eta_{\mathbf{x}_a},$$

$$R_{\mathbf{x}_a}(t_1,t_2) = E\{\mathbf{x}_a(t+\tau)\mathbf{x}_a^*(t)\} = R_{\mathbf{x}_a}(\tau). \tag{4.34}$$

The mean square of a stationary process is thus also constant:

$$E\{|\mathbf{x}_a(t)|^2\} = R_{\mathbf{x}_a}(0) = \sigma^2_{\mathbf{x}_a}. \tag{4.35}$$

The power spectral density (PSD) of a stationary process is the Fourier transform of its autocorrelation function:

$$S_{\mathbf{x}_a}(\omega) = \int_{-\infty}^{\infty} R_{\mathbf{x}_a}(\tau)e^{-i\omega\tau}\mathrm{d}\tau. \tag{4.36}$$

In the case where a random process is considered as noise, the PSD gives the noise power as a function of frequency.

The output of an LTI system with a stationary random process $\mathbf{x}_a(t)$ as input is itself a stationary random process:

$$\mathbf{y}_a(t) = \int_{-\infty}^{\infty} \mathbf{x}_a(t-\tau)h(\tau)\mathrm{d}\tau. \tag{4.37}$$

The mean of the output is thus also constant:

$$\eta_{\mathbf{y}_a}(t) = \int_{-\infty}^{\infty} E\{\mathbf{x}_a(t-\tau)\}h(\tau)\mathrm{d}\tau = \eta_{\mathbf{x}_a}\int_{-\infty}^{\infty} h(\tau)\mathrm{d}\tau = \eta_{\mathbf{x}_a}. \tag{4.38}$$

The mean value of a stationary noise process filtered by a system with an impulse response that integrates to zero in the time domain is thus zero, as is the case of pileup noise filtered

by the HEC electronics. The autocorrelation of the output is related to $R_{\mathbf{x}_a}$ by:

$$R_{\mathbf{y}_a}(\tau) = R_{\mathbf{x}_a}(\tau) * h^*(-\tau)h(\tau). \tag{4.39}$$

The PSD of the output can thus be expressed as:

$$S_{\mathbf{y}_a}(\omega) = S_{\mathbf{x}_a}(\omega)|H(\omega)|^2. \tag{4.40}$$

### 4.4.2 Discrete-time Random Signals

Random discrete-time signals behave in an analogous way to random analog signals. Let $\mathbf{x}[n]$ be a discrete-time process, specifically a random variable measured at index $n$. As stationary processes have been discussed in the previous section, only random processes that are stationary in nature will be discussed. Many of the results from the previous section still apply.

The mean or expectation value of the process $\mathbf{x}[n]$, denoted $\eta_{\mathbf{x}}[n]$, is constant:

$$E\{\mathbf{x}[n]\} = \eta_{\mathbf{x}}[n] = \eta_{\mathbf{x}}. \tag{4.41}$$

The autocorrelation of this process, denoted $R_{\mathbf{x}}[n_1, n_2]$, only depends on the sample distance $m = n_1 - n_2$, and is the expectation values of the product $\mathbf{x}[n_1]\mathbf{x}^*[n_2]$:

$$E\{\mathbf{x}[n_1]\mathbf{x}^*[n_2]\} = R_{\mathbf{x}}[n_1, n_2] = R_{\mathbf{x}}[m]. \tag{4.42}$$

The mean square of this process is:

$$E\{|\mathbf{x}[n]|^2\} = R_{\mathbf{x}}[0] = \sigma_{\mathbf{x}}^2, \tag{4.43}$$

which is constant in time. The PSD of this process is the DTFT of its autocorrelation function:

$$S_{\mathbf{x}}(\omega) = \sum_{k=-\infty}^{\infty} R_{\mathbf{x}}[m]e^{-i\omega m}. \tag{4.44}$$

The output $\mathbf{y}[n]$ of an LTI discrete-time system with a discrete-time random stationary process $\mathbf{x}[n]$ as input is itself a stationary random process. Its mean $\eta_{\mathbf{y}}$ and mean square $\sigma_{\mathbf{y}}^2$ are thus also constant, with its autocorrelation function being related to $R_{\mathbf{x}}[m]$ by:

$$R_{\mathbf{y}}[m] = R_{\mathbf{x}}[m] * h^*[-m] * h[m]. \tag{4.45}$$

The PSD of the output can thus be expressed as:

$$S_{\mathbf{y}}(\omega) = S_{\mathbf{x}}(\omega)|H(\omega)|^2. \tag{4.46}$$

The stationary discrete-time random processes that will be studied are in a wide-sense ergodic, meaning that the mean and autocorrelation of the process can be computed from the time averages of a single sample sequence $x[n]$:

$$E\{\mathbf{x}[n]\} = \langle x[n] \rangle = \lim_{L\to\infty} \frac{1}{2L} \sum_{n=-L}^{L} x[n], \tag{4.47}$$

$$E\{\mathbf{x}[n+m]\mathbf{x}^*[n]\} = \langle x[n+m]x^*[n] \rangle = \lim_{L\to\infty} \frac{1}{2L} \sum_{n=-L}^{L} x[n+m]x^*[n]. \tag{4.48}$$

This is true for stationary processes with a finite mean and an autocorrelation sequence that is finite in length [66], such as the thermal and pileup noise in the HEC (see Chapter 5).

## 4.5 Quantization of Continuous Amplitude Signals

ADCs convert analog signals to digital sequences of binary numbers with finite precision according to the number of bits $b$ with which it represents them. The quantization of a discrete-time signal $x[n]$ can be mathematically described by a non-linear system $Q$ which rounds an input value to the nearest quantization value and limits it to the dynamic range $d = x_{max} - x_{min}$ of the ADC. This is shown in the following relation, where $x_d \in [x_{min}, x_{max}]$ is the digitized sample:

$$x_d[n] = Q\{x[n]\} = Q\{x_a(nT)\}. \tag{4.49}$$

In the case of a rounding ADC with equally spaced quantization values, the lsb which determines the step size $\Delta$ between successive quantization levels is:

$$\Delta = \frac{d}{2^b}. \tag{4.50}$$

The operation of quantizing a discrete-time signal introduces an error called the "quantization error" $e[n]$ [67]:

$$e[n] = x_d[n] - x[n] = Q\{x[n]\} - x[n]. \tag{4.51}$$

In our case, if $x_{min} - \frac{\Delta}{2} < x[n] \leq x_{max} + \frac{\Delta}{2}$, i.e. the discrete-time signal's amplitude lies within the dynamic range of the ADC, then $-\frac{\Delta}{2} \leq e[n] < \frac{\Delta}{2}$. If $x[n]$ is outside this range, the ADC is

saturated and the absolute error can be larger than $\frac{\Delta}{2}$.

The quantization system can be thought of as the operation of adding noise to an input signal. Here, the error can be represented by the uniformly distributed PDF:

$$p(e) = \begin{cases} \frac{1}{\Delta} & \text{if } -\frac{\Delta}{2} \leq e[n] < \frac{\Delta}{2} \\ 0 & \text{if } -\frac{\Delta}{2} > e[n] \geq \frac{\Delta}{2} \end{cases}. \tag{4.52}$$

This gives an error with mean $\eta_e = 0$ and mean square $\sigma_e^2 = \frac{\Delta^2}{12}$. In the case where the ADC is not ideal, it introduces some thermal noise when quantizing a signal. The amount of thermal noise coming from the ADC is quantified by the ENOB parameter $b_{eff}$. With this, the mean square of the total noise introduced in the procedure of quantizing a signal with a realistic ADC, $\sigma_{tot}^2$, becomes:

$$\sigma_{tot}^2 = \frac{d^2}{12 \cdot 2^{2b_{eff}}}. \tag{4.53}$$

The mean square of the thermal noise introduced by the ADC is therefore:

$$\sigma_{ENOB}^2 = \left(2^{2(b-b_{eff})} - 1\right) \frac{\Delta^2}{12}. \tag{4.54}$$

The digitized sequence after the quantization procedure of a realistic ADC can be mathematically described as:

$$x_d[n] = Q\{x[n]\} + \mathcal{N}_n(0, \sigma_{ENOB}), \tag{4.55}$$

where $\mathcal{N}_n(\eta, \sigma)$ represents a random number drawn from a normal distribution with mean $\eta$ and standard deviation $\sigma$.

# Chapter 5

# ATLAS Readout Electronics Upgrade Simulation

In this chapter, the ATLAS Readout Electronics Upgrade Simulation (AREUS) [71] software framework used to test and optimize the performance of the HEC readout electronics at HL-LHC is described. The implementation in this framework of the HEC geometry, readout electronics, thermal noise and pileup noise is described along with the energy reconstruction algorithms used to extract energy from the sampled pulse shape. Finally, Section 5.6.3 details the measurement of a digital filter's energy resolution. Details of the software implementation of AREUS can be found in [72, 73, 71].

## 5.1 Introduction

AREUS was developed and validated to provide a highly flexible and precise simulation of the LAr calorimeter system's trigger electronics. Its flexibility allowed for the implementation of the HEC electronic readout chain currently in use, while providing the means to test new and more complex filtering algorithms for the Phase-II upgrade. In addition, the ability to integrate ATLAS simulated collision data within the software framework makes it possible to simulate the readout electronics response to both the physics signals and pileup noise expected at HL-LHC.

AREUS is designed in a modular way. Each module is strictly independent and is responsible for the simulation of one part of the calorimeter's electronics chain, from the ionization of the LAr in the calorimeter cells to the digital filtering algorithms responsible

for energy reconstruction. Two different modules are responsible for reading data in the form of energy deposits in sequential bunch crossings and providing them to subsequent modules for processing. One module uses official ATLAS simulated data as input for a simulation of the entire LAr calorimeter; the other module can instead be fed a sequence of energies deposited in a single channel. The latter is ideal for studying the performance of filters in detail without the need to simulate the full calorimeter. The main modules of interest in this section are those that had to be adapted to the response of the HEC readout electronics. These are the modules responsible for simulating the channel mapping as well as the analog processing and thermal noise in the front-end electronics. Finally, a digital filtering module simulates the energy reconstruction algorithms. Modules for the monitoring and analysis of the different stages are also provided.

## 5.2 HEC Implementation

The mapping of the HEC readout channels and their properties is crucial for the accurate simulation of the HEC's expected pulse shape and thermal noise. Since the HEC has a $\phi$ and $\pm z$ symmetry, its 5632 readout channels can be accurately described by the parameters of the of 51 channels shown in Figure 5.1. The channel numbering goes up to 56 in a non-sequential way as some of the layers do not cover the full range of $1.5 < |\eta| < 3.2$, meaning some channel numbers are skipped. The most important properties of the HEC channels are their respective capacitances, the drift time of the electrons in the channel's LAr gaps and the lengths of the cables that carry the electrical signal from the LAr gaps to the PSBs. The capacitance determines the rise time of the signal in the preamplifiers and affects the amount of thermal noise in the electronics. The drift time of the electrons defines the shape of the ionization signal. The cable lengths affect the signal shape due to reflections inside the transmission line.

The values of these parameters and the analytical models for the HEC's pulse shape and thermal noise presented in the next two sections were obtained from reference [44]. These parameters were validated with data from the HEC's test beam setup [74] prior to its installation in ATLAS.

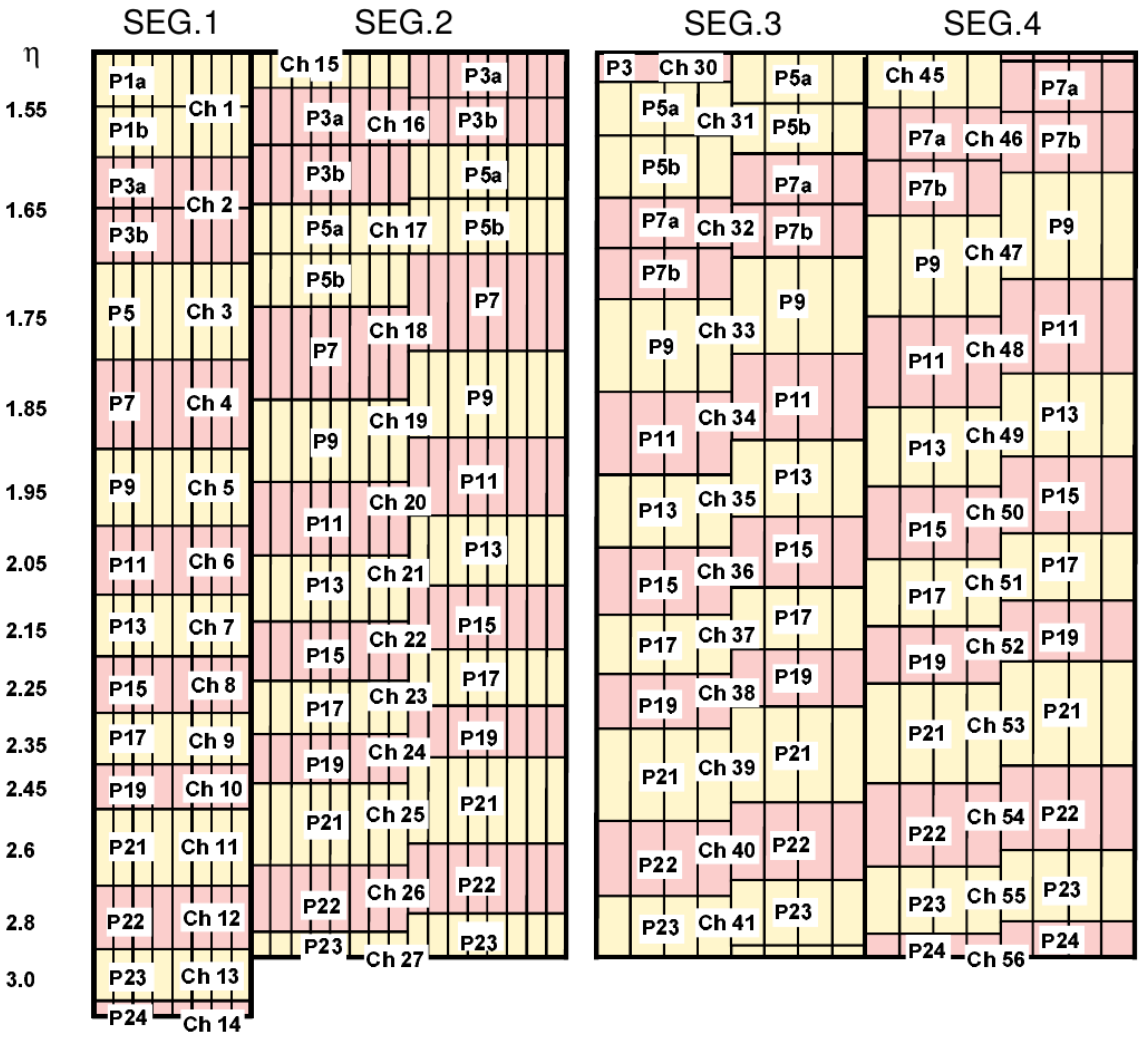


Fig. 5.1 Schematic diagram of the HEC in the $R-z$ plane and numbering of the readout channels [44].

## 5.3 Analog Shaping

First in the readout chain is the ionization signal in the HEC's LAr gap. The triangular ionization pulse can be described by:

$$I(t) = I_0 \left(1 - \frac{t}{\tau_{drift}}\right) \quad \text{for} \quad 0 < t < \tau_{drift}, \tag{5.1}$$

where $I_0$ is the initial ionization current from Equation 3.5 and $\tau_{drift}$ is the drift time of the electrons in the gap.

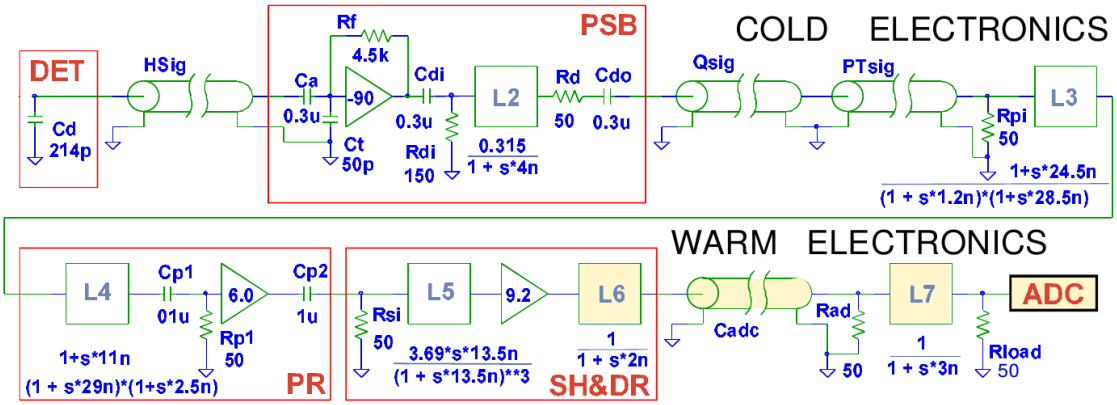


Fig. 5.2 Schematic diagram of the HEC readout electronics currently in use [44]. The objects highlighted in yellow are specific to the HEC's test beam setup and are replace by a single pole in the ATLAS detector (see Equation 5.9).

A schematic diagram of the HEC electronics chain is shown in Figure 5.2, with the top half showing the cold electronics inside the cryostat and the bottom half showing the electronics installed on the FEBs. The values of the different parameters of the HEC's analog readout chain referred to in Figure 5.2 are summarized in Table 5.1. A HEC readout channel is modeled as an ideal source of current with capacitance $C_d$. Each of the 51 different types of HEC channels have a different detector capacitance. The ionization signal first goes through the signal cables *HSig*, as shown in Figure 5.2, to the PSB, which is described by its transfer function:

$$H_{PSB}(s) = \frac{R_p}{(1+s\cdot\tau_a)(1+s\cdot\tau_d)} \quad \text{where} \quad \tau_a = R_a(C_d+C_a). \tag{5.2}$$

The transfer function describing the decoupling capacitors $C_{di}$ and $C_{do}$ which differentiate the signal is:

$$H_{Cap}(s) = \frac{s^2\cdot\tau_{d1}\tau_{d2}}{(1+s\cdot\tau_{d1})(1+s\cdot\tau_{d2})}, \tag{5.3}$$

where

$$\tau_{d1} = 150\Omega\cdot C_{di} \quad \text{and} \quad \tau_{d2} = 50\Omega\cdot C_{do}. \tag{5.4}$$

The distortion in the cables following the PSB is modeled as:

$$H_{Cab}(s) = \frac{a_s\cdot(1+\tau_{zs})}{(1+s\cdot\tau_{os})(1+s\cdot\tau_{ps})}. \tag{5.5}$$

| Transfer function | Parameter | Value |
|---|---|---|
| $H_{PSB}(s)$ | $\tau_d$ | 4 ns |
| | $R_p$ | 750 Ω |
| | $R_a$ | 50 Ω |
| | $C_a$ | 50 pF |
| | $C_d$ | Channel specific |
| $H_{Cap}(s)$ | $C_{di}$ | 0.3 pF |
| | $C_{do}$ | 0.3 pF |
| $H_{Cab}(s)$ | $a_s$ | 0.963 |
| | $\tau_{zs}$ | 24.7 ns |
| | $\tau_{os}$ | 1.3 ns |
| | $\tau_{ps}$ | 28.9 ns |
| $H_{PR}(s)$ | $G_p(front)$ | 5.5 |
| | $G_p(rear)$ | 11 |
| | $C_p$ | 1 $\mu$F |
| | $\tau_i$ | 14.0 ns |
| | $\tau_o$ | 1.0 ns |
| $H_{SH}(s)$ | $G_s$ | 10.0 |
| $H_{DR}(s)$ | $\tau_{df}$ | 1.0 ns |

Table 5.1 Values of the HEC electronic readout chain parameters.

The HEC signal then travels outside the cryostat through the feedthroughs to the FEBs. There, the signal first goes through the preshaper (PR in Figure 5.2), which has the following transfer function:

$$H_{PR}(s) = \frac{s \cdot \tau_{d3} \cdot G_p(1+s\cdot\tau_{pz})}{(1+s\cdot\tau_i)(1+s\cdot\tau_o)(1+s\cdot\tau_{d3})} \quad \text{, where} \quad \tau_{d3} = 50\Omega \cdot C_p. \tag{5.6}$$

Here, $G_p$ is the preshaper's gain, which is twice as high in the two rear layers of the HEC to compensate for the smaller sampling fraction. The zero with time constant $\tau_{pz}$ is

$$\tau_{pz} = 50\Omega \cdot (C_d + C_a), \tag{5.7}$$

thereby canceling the pole in the PSB with time constant $\tau_a$ (see Equation 5.2). The preshaper thus corrects for the preamplifier rise time through pole-zero cancellation, making the HEC pulse shape, after the preshaping stage, independent of the channel's capacitance.

The shaper currently in use (SH in Figure 5.2) is a $CR-(RC)^2$ circuit with transfer function (see Section 4.1):

$$H_{SH} = 3.69 \cdot G_s \cdot \frac{s \cdot \tau_s}{(1+s \cdot \tau_s)^3}, \tag{5.8}$$

where $3.69 \cdot G_s$ is the shaper's gain and $\tau_s = RC = CR$ are the shaper's time constants. The shaper in the current readout electronics uses $\tau_s = 13$ ns.

The line driver that carries the shaped signal to the ADC is described by 1 pole:

$$H_{DR}(s) = \frac{1}{(1+s \cdot \tau_{df})}. \tag{5.9}$$

The complete transfer function of the current analog electronics is thus:

$$H(s) = H_{PSB}(s) \cdot H_{Cap}(s) \cdot H_{Cab}(s) \cdot H_{PR}(s) \cdot H_{SH}(s) \cdot H_{DR}(s). \tag{5.10}$$

To derive an analytical expression for the HEC's pulse shape, the method of partial fraction expansion is used (see Section 4.1). As the readout chain's transfer function has 13 pole, the partial fraction expansion method requires solving a $13 \times 13$ matrix. Mathematica [75] is used for solving this problem. After obtaining the transfer function in the time domain, convolving it with the ionization signal (see Equation 5.1) is done using the relations:

$$\left(\delta(t) - \frac{1}{\tau_{drift}}\right) * e^{-\frac{t}{\tau}} = \begin{cases} \left(1 + \frac{1}{\tau_{drift}}\right) \cdot e^{-\frac{t}{\tau}} - \frac{\tau}{\tau_{drift}} & \text{for } t < \tau_{drift} \\ \left(1 + (1 - e^{\frac{\tau_{drift}}{\tau}}) \frac{\tau}{\tau_{drift}}\right) \cdot e^{-\frac{t}{\tau}} & \text{for } t > \tau_{drift}. \end{cases} \tag{5.11}$$

This is done for each pole with time constant $\tau$ in the HEC's transfer function.

The shaper and its shaping time need to be re-optimized for the pileup conditions at the HL-LHC. Changing the time constants or adding/removing integration stages (*RC* filters) can be done without changing the bipolar nature of the HEC's pulse shape. A monopolar pulse shape could reduce power consumption in the front-end and increase the dynamic

range of the ADCs as it would not need to sample the pulse's undershoot which accounts for approximately $^1/_4{}^{\text{th}}$ of the dynamic range. However, the fact that the bipolar pulse shape integrates to zero is important to maintain a zero pedestal shift in the readout.

Figure 5.3 shows the pulse shape obtained normalized to an amplitude of 1 for different parameters of the shaper. In Figure 5.3(a), the HEC pulse shape for three different shaper time constants is shown. Reducing the shaper's time constants leads to a narrower pulse shape. In Figure 5.3(b), the HEC pulse shape for three different shaper circuits is shown. The shapers are formed by adding/removing an integration stage to the current $CR-(RC)^2$ shaper. Similarly to reducing the shaper's time constants, removing integration stages leads to a narrower pulse shape. In the next section, the thermal noise and the effect of the different shaper configurations on its PSD are described.

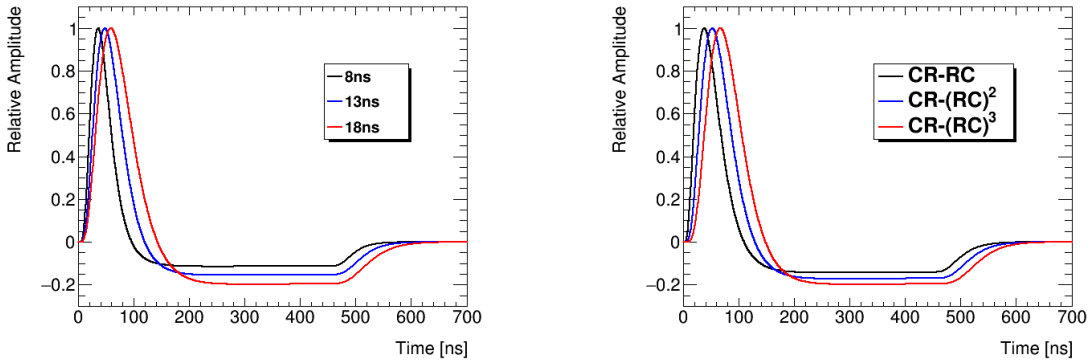


(a) (b)

Fig. 5.3 Normalized pulse shapes for (a) different shaper time constants with a $CR-(RC)^2$ shaper and (b) different shaper circuits with time constants of $RC = CR = 13$ ns in the HEC channel located in layer HEC1 at $\eta = 2.35$.

## 5.4 Thermal Noise

The digital energy reconstruction algorithms rely heavily on an accurate knowledge of the noise's autocorrelation function, and thus its PSD (see Section 5.6). An accurate model of the HEC's thermal noise PSD is thus crucial to the simulation and optimization of the HEC's readout chain.

A schematic diagram of the sources of thermal noise (or Johnson-Nyquist noise [52, 53]) coming from the HEC preamplifiers is shown in Figure 5.4. It consists of two independent

noise sources at the preamplifier input, a series voltage noise ($e_s$) and a parallel current noise ($i_p$). Their PSDs are described by [44]:

$$\frac{\mathrm{d}}{\mathrm{d}f}\overline{i_p^2}(\omega) = \frac{4kT}{R_{pn}}(1+\frac{\omega_s}{\omega}) \tag{5.12}$$

and

$$\frac{\mathrm{d}}{\mathrm{d}f}\overline{e_s^2}(\omega) = \frac{4kT}{R_{sn}}, \tag{5.13}$$

where $R_{sn} = 400\ \Omega$ and $R_{pn} = 45\ \Omega$ are the equivalent series and parallel noise resistances, respectively. The parameter $\omega_s = 0.6$ Mrad/s is the corner frequency of the GaAs preamplifier chips which accounts for its flicker noise contribution, often called pink noise or $\frac{1}{f}$ noise. Finally, $k$ is Boltzmann's constant and $T = 87$ K is the temperature inside the cryostat.

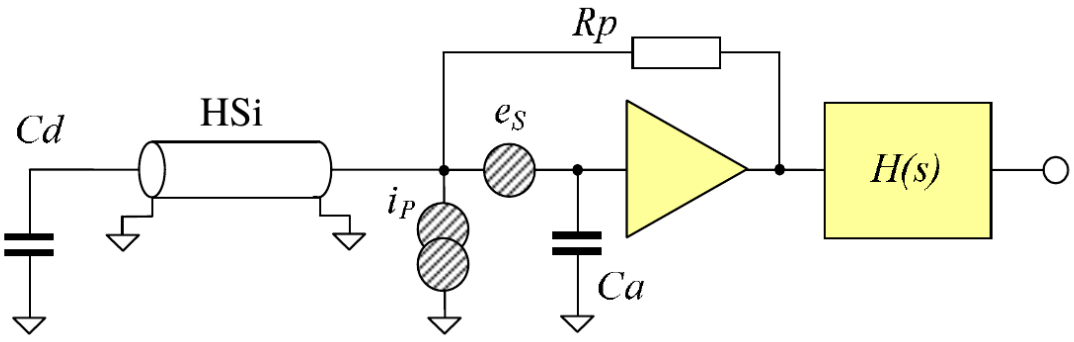


Fig. 5.4 Schematic diagram of the sources of thermal noise in the HEC's electronic readout chain [44]. The symbol $H(s)$ is the HEC's transfer function (see Equation 5.10) without the factor $R_p$ and pole with time constant $\tau_a$ from $H(s)_{PSB}$ (see Equation 5.2).

Reflections of the signal in *HSig* are described by an ideal transmission line loaded by the capacitance $C_d$ of the HEC channel. The impedance of the transmission line is:

$$Z_{HSig}(\omega) = \rho \cdot \frac{1+\kappa(\omega)\cdot e^{-2i\omega T_c}}{1+\kappa(\omega)\cdot e^{-2i\omega T_c}}, \tag{5.14}$$

where the voltage reflection factor is:

$$\kappa(\omega) = \frac{1-i\omega\rho C_d}{1-i\omega\rho C_d}. \tag{5.15}$$

Here, $\rho = 50\ \Omega$ is the characteristic impedance of the transmission line and:

$$T_c = Length \cdot Delay = L_{H_{Sig}} \cdot 5.68\ \text{ns/m} \tag{5.16}$$

is the propagation time of the signal in the transmission line. Each of the 51 different types of HEC channels have different signal cable lengths $L_{H_{Sig}}$.

Using Ohm's law and Equations 5.12, 5.13 and 5.14, the PSD of the total noise current at the preamplifier input is obtained:

$$\frac{\mathrm{d}}{\mathrm{d}f}\overline{i^2}(\omega) = \left|\frac{1+i\omega(C_a+C_d)R_a}{1+i\omega(C_a+C_{HSig}(\omega))R_a}\right|^2 \times \left(\frac{4kT}{R_{pn}}\left(1+\frac{\omega_s}{\omega}\right)+\frac{4kT}{R_{sn}}\cdot\omega^2\left|C_a+C_{HSig}(\omega)\right|^2\right). \tag{5.17}$$

Here, $C_{HSig}(\omega)$ is the capacitance of the transmission line:

$$C_{HSig}(\omega) = \frac{1}{i\omega Z_{HSig}(\omega)}. \tag{5.18}$$

The PSD of the thermal noise in the HEC electronics readout chain is thus given by:

$$S(\omega) = \frac{\mathrm{d}}{\mathrm{d}f}\overline{i^2}(\omega)\cdot\left|H(s=i\omega)\right|^2. \tag{5.19}$$

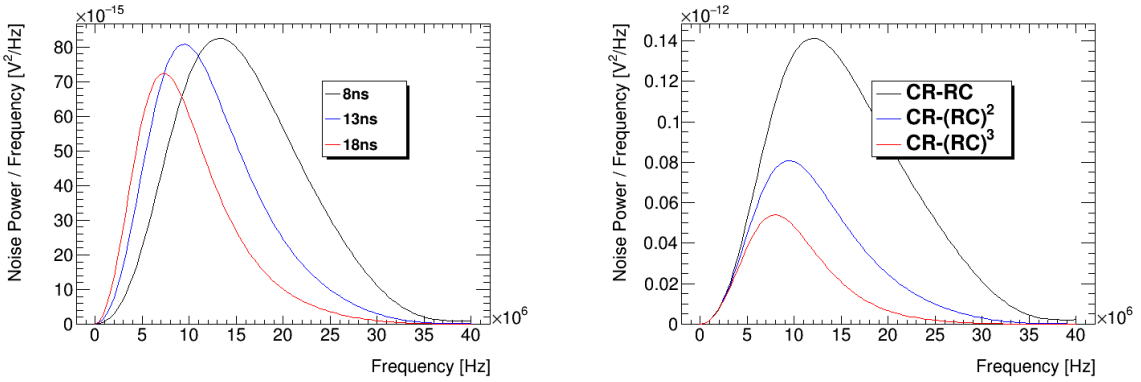


(a) (b)

Fig. 5.5 Thermal noise PSD for (a) different shaper time constants with a $CR-(RC)^2$ shaper and (b) different shaper circuits with time constants $CR = RC = 13$ ns in the HEC channel located in layer HEC1 at $\eta = 2.35$.

The PSD of the thermal noise in the HEC analog readout electronics is plotted in Figure 5.5 for the different configurations of the HEC's shaper discussed in the previous section. By increasing the shaper's time constants or adding an integration stage, higher frequencies of noise are attenuated. The autocorrelation functions of the noise for the different shaper configurations are shown in Figure 5.6. Adding an integration stage significantly decreases the mean square of the thermal noise (first sample of the autocorrelation function) when compared to increasing its shaping time. Conversely, while removing an integration stage to reduce the width of the pulse shape (see Figure 5.3) may be desirable for readout channels where pileup noise is dominant, it also greatly increases the mean square of the noise when compared to the impact of reducing the shaping time constants.

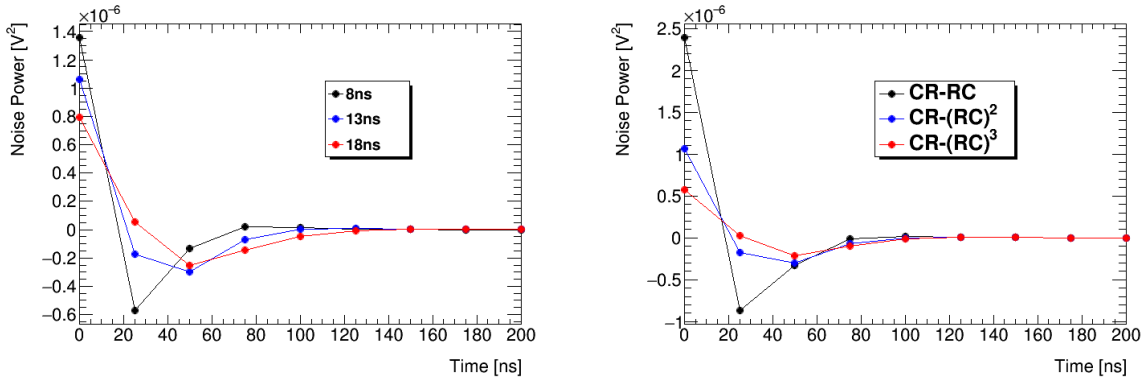


(a) (b)

Fig. 5.6 Thermal noise autocorrelation function for (a) different shaper time constants with a $CR-(RC)^2$ shaper and (b) different shaper circuits with time constants $CR = RC = 13$ ns in the HEC channel located in layer HEC1 at $\eta = 2.35$.

## 5.5 Pileup Noise

The modeling of proton-proton collisions at the ATLAS IP, the electronic and hadronic showers that they produce when interacting with the detector as well as the detector's response requires the use of complex simulation packages. Official ATLAS simulated data is used to determine the probability distribution functions (PDFs) of the expected pileup noise in the HEC at HL-LHC.

For the work presented in this thesis, minimum bias events generated with Pythia8 [76] are used in order to simulate the pile-up conditions expected at the HL-LHC. Minimum bias events in the context of this thesis are simply events that would be accepted by the

minimum bias trigger, which mainly consists of elastic proton-proton interactions. The final state particles of these interactions and their decay products are then run through a detailed simulation of the ATLAS detector in GEANT4 [77, 78], which simulates the interaction of the collision products with the material in the detector as well as the detector's response. The output consists of the energies deposited in the LAr gaps of the HEC, which are then converted to current by AREUS.

The simulation used for the pileup noise in this thesis is based on the expected ATLAS geometry and pileup conditions at the HL-LHC after the Phase-II upgrade. The proton-proton collisions are thus simulated at a center of mass energy of 14 TeV and an average number of interactions per bunch crossing $\langle\mu\rangle = 200$. This corresponds to an instantaneous luminosity of $\mathscr{L} = 7.5 \cdot 10^{34}\text{cm}^{-2}\text{s}^{-1}$, the "worst case" scenario in terms of the level of pileup noise the electronics need to be able to cope with.

From this dataset, the PDFs for the energy of a single minimum bias event is calculated for each HEC channel. These PDFs are based on the model described in reference [79]. The PDFs as a function of energy are described by the formula:

$$P_{tot}(E) = q \cdot \delta(E) + (1-q) \cdot P_E(E), \tag{5.20}$$

where q is the probability that a minimum bias event will deposit no energy in a readout channel and $P_E$ is the energy distribution. The energy distribution of a minimum bias event in a HEC channel is shown in Figure 5.7(a). Energy deposits in sequential bunch crossings are approximated to be uncorrelated (the minimum bias event PDFs do not change as a function of time). However, as the energy from a minimum bias event ionizes the LAr in a HEC cell, it is shaped and sampled in the HEC's readout chain. This gives pileup noise a complex frequency dependence. Its autocorrelation function $R_{pu}[n]$ in terms of the total energy deposited in a HEC channel by pileup is given by:

$$R_{pu}[n] = \sigma_E^2 \cdot \frac{R_{sps}[n]}{R_{sps}[0]}, \tag{5.21}$$

where $\sigma_E^2$ is the mean square of the total energy deposited by pileup (which depends on in a HEC channel $\langle\mu\rangle$) and $R_{sps}[n]$ is the autocorrelation function of the HEC's sampled pulse shape. The pileup noise autocorrelation function for the different shaper configurations described in Section 5.3 is shown in Figure 5.8. Reducing the shaping time constants to 8 ns

reduces the mean square of the pileup noise (first sample of the autocorrelation function). Removing an integration stage also reduces the mean square, though to a lesser extent. Pileup noise remains autocorrelated over a much longer period of time when compared to the autocorrelation function of thermal noise (see Figure 5.6).

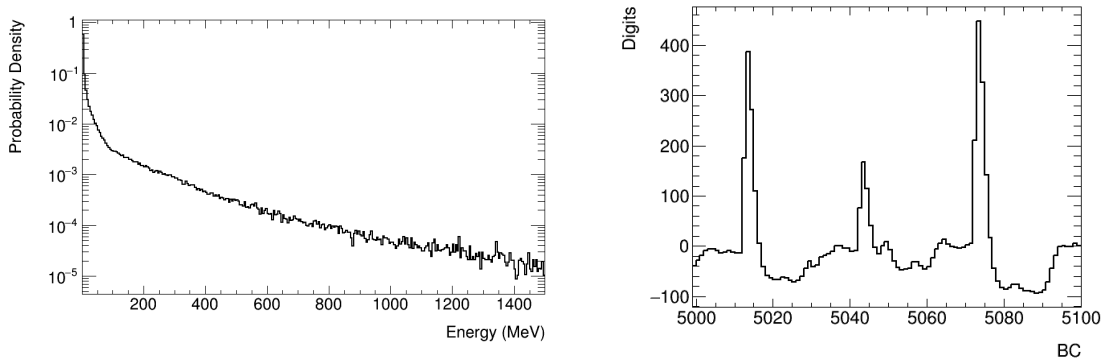


(a) (b)

Fig. 5.7 Figure (a) shows the energy distribution of a single minimum bias event in the HEC1 at $\eta = 2.35$ with $q = 0.805$. Figure (b) shows a sequence of digitized samples as function of time (expressed in units of number of bunch crossings). This sequence of digitized samples was simulated assuming three large energy deposits at intervals of 30 bunch crossings on top of a pileup contribution obtained assuming $\langle\mu\rangle = 200$.

The minimum bias PDFs are not expected to change as a function of the instantaneous luminosity of the LHC. As such, they can be used to generate sequences of energy deposits in a HEC channel at different pileup conditions, given that the number of interactions per bunch crossing is entirely determined by how many times the PDF is sampled. In AREUS, at every bunch crossing, the number of minimum bias interactions that occur is either determined by a random number Poisson distributed around $\langle\mu\rangle$ or fixed to $\mu$. Then, a number uniformly distributed from 0 to 1 is generated. If it is bigger than $q$, the probability that a single minimum bias event will deposit exactly no energy in the channel, the energy distribution is sampled. This is done $\mu$ times to obtain the total energy deposited by minimum bias events in the channel at that bunch crossing.

In addition to this pileup noise, signals with energies uniformly distributed between 0 and 50 GeV are artificially added in order to study the energy resolution of different digital filters. This is done at intervals of 30 bunch crossings to avoid overlap between signals. A sequence of energy deposits generated with $\langle\mu\rangle = 200$ is shown in Figure 5.7(b). Sequences

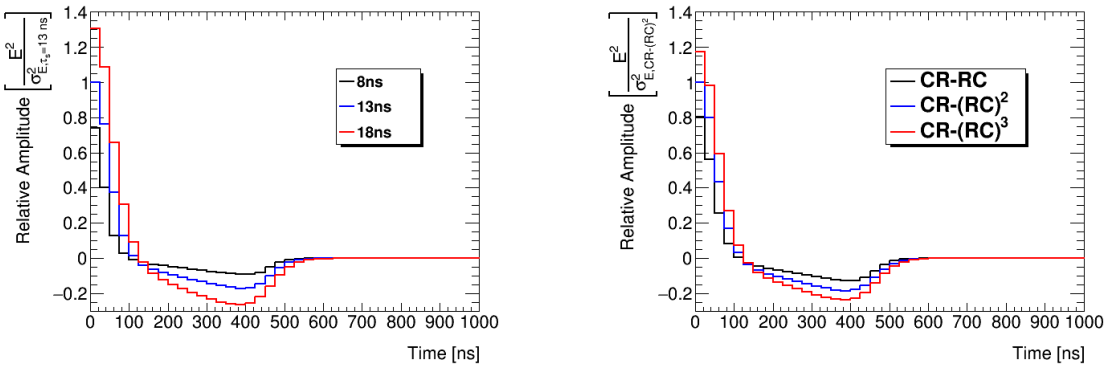


(a) (b)

Fig. 5.8 Pileup autocorrelation function for (a) different shaper time constants with a $CR-(RC)^2$ shaper and (b) different shaper circuits with time constants $CR = RC = 13$ ns in the HEC channel located in layer HEC1 at $\eta = 2.35$. Autocorrelation functions are normalized to the mean square of the pileup noise in the current HEC shaper ($CR-(RC)^2$ with $\tau_s = RC = 13$ ns).

of 1 million bunch crossings are generated for select channels that span the range of thermal and pileup noise conditions in the HEC. No signals are artificially added in the first 3000 bunch crossings which are reserved for the calibration of the digital filters on only thermal and pileup noise, which is discussed in the next section.

## 5.6 Sampling, Digitization and Filtering

In AREUS, the sequence of energy deposits in a channel is converted to current, shaped and then sampled at 40 MHz. Thermal noise is then added to every individual sample in order to save on computing time. An example of thermal noise in the simulation of a HEC channel is given in Figure 5.9(a). In order to accurately describe this process, aliasing was added to the AREUS simulation. As you can see from Figure 5.5, the thermal noise in the HEC is not band-limited to 20 MHz, so sampling it at 40 MHz introduces significant aliasing of its PSD. In addition to improving the performance of the energy reconstruction algorithms, sampling at 80 MHz would thus significantly reduce aliasing of the thermal noise.

The process of digitizing the signal is done by rounding the samples of the pulse shape to the nearest ADC digit. In the HEC, the current ADC has 12 bits with an lsb of 112 MeV (or 1 mV). The thermal noise in the ADC is modeled by the ENOB parameter, which is 11.3 on the current FEBs, according to the description in Section 4.5. An example of the quantization

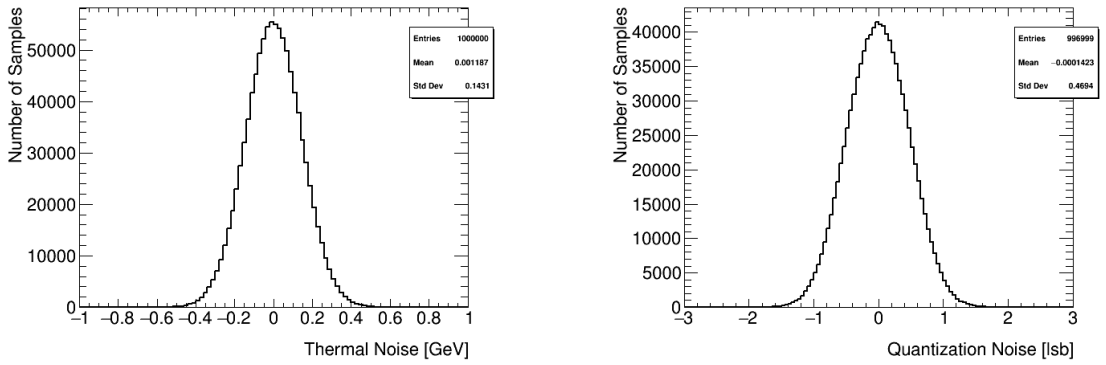


(a) (b)

Fig. 5.9 Example of (a) thermal noise and (a) quantization noise that is simulated for every sample of a sequence of digitized samples simulated in the HEC 1 at $\eta = 2.35$.

noise (rounding error + thermal noise of the ADC) in the simulation of a HEC channel is shown in Figure 5.9(b). From Equation 4.53, the standard deviation of the noise should be 52.5 MeV or equivalently 0.469 lsb. In the context of this thesis, electronic noise refers to the thermal noise in the analog electronics and the quantization noise in the ADC.

At this point in the simulation chain, digital filters are used to reconstruct the energy deposited in a bunch crossing by a physically interesting event. A description of the two filters tested for the Phase-II upgrade of the HEC is given in the next two subsections. AREUS uses the first 3000 bunch crossings (in the case of this study) in a sequence of ADC samples to calculate the filter coefficients. These are then applied to the rest of the sequence to test the energy resolution of the filter.

### 5.6.1 Optimal Filter

The optimal filter (OF) [80] is the energy reconstruction algorithm currently implemented in the LAr calorimeter back-end electronics. It is a FIR filter designed to minimize the mean square of the total noise (pileup and electronic noise). The OF does this by optimizing the shaping time of its output on a channel by channel basis. This can be seen in Figure 5.10. When the OF is calibrated on a sequence with no pileup noise, its output has a broader peak than the input pulse shape (see Figure 5.10(a)). Conversely, when the OF is calibrated on a sequence with high pileup, its output has a narrower peak than its input (see Figure 5.10(b)).

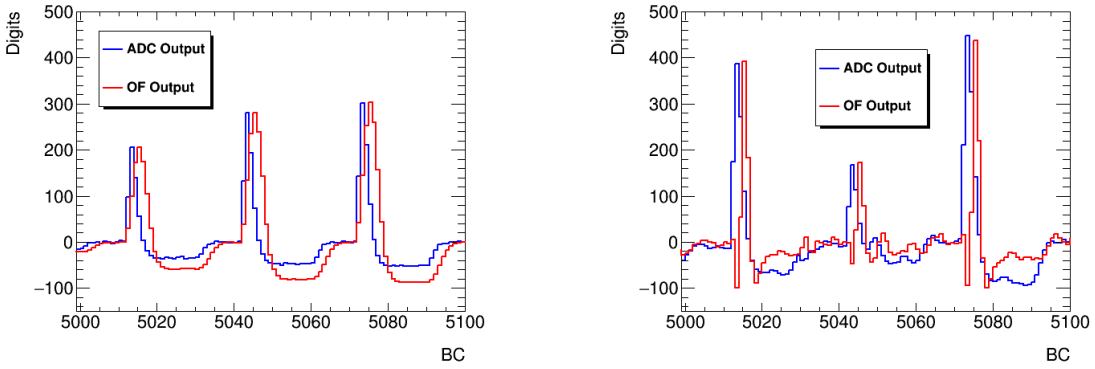


(a) (b)

Fig. 5.10 Example outputs of the ADC and OF for three consecutive significant energy deposits with pileup conditions (a) $\mu = 0$ and (b) $\langle\mu\rangle = 200$ in the HEC 1 at $\eta = 2.35$. Sequences are shown as a function of time (in units of bunch crossings).

### Filter Coefficients

A sampled pulse shape in the HEC $x[n]$ can be described as:

$$x[i] = Ag(iT_s + \phi_{ADC} - t_0), \tag{5.22}$$

where $g(t)$ is the normalized analog pulse shape sampled at intervals of $T_s = 25$ ns, $\phi_{ADC}$ is the ADC phase, $A$ is the amplitude of the pulse shape and $t_0$ is the timing of the ionization signal with respect to $i = 0$. The optimal filter attempts to extract the amplitude $A$ of the pulse shape which is proportional to the energy deposited in the channel. In doing so, the pulse shape $g(t)$ and ADC phase $\phi_{ADC}$ must be known precisely. In other words, the samples $g[i]$ of the normalized and sampled pulse shape must be known. A signal $s[i]$ deposited at a time $t_0$ after sample $i = 0$ in a sequence with pileup and electronic noise $n[i]$ is described to first order by:

$$s[i] \approx Ag[i] - At_0 g'[i] + n[i]. \tag{5.23}$$

Here, $g'[i]$ is the time derivative of $g[n]$. This is a valid approximation in the limit where the time between a bunch crossing and an energy deposit in a HEC channel $t_0$ is small. The output of the optimal filter is described by [80]:

$$u[i] = \sum_{i=0}^{N-1} a_i s[i], \tag{5.24}$$

where $u[i]$ is the filter output, $a_i$ the filter coefficients (or transfer function, $h[i] = a_i$) and $N$ the filter depth (number of coefficients). The coefficients are calculated in such a way that, on average, the OF outputs the amplitude of the signal:

$$\langle u[i] \rangle = A = \sum_{i=0}^{N} a_i \left( Ag[i] - At_0 g'[i] + \langle n[i] \rangle \right). \tag{5.25}$$

Given the bipolar pulse shape of the HEC, $\langle n[i] \rangle = 0$, giving constraints on the filter coefficients:

$$\sum_{i=0}^{N} a_i g[i] = 1 \quad \text{and} \quad \sum_{i=0}^{N} a_i g'[i] = 0. \tag{5.26}$$

The mean square of $u$ is given by:

$$\langle |u[i]|^2 \rangle = \sum_{i=0}^{N} \sum_{j=0}^{N} a_i a_j \langle n[i] n[j] \rangle = \sum_{i=0}^{N} \sum_{j=0}^{N} a_i a_j R_n[i,j], \tag{5.27}$$

where $R_n[i,j]$ is the autocorrelation matrix of the noise $n[i]$. To calculate the OF coefficients, the mean square of $u[i]$ is minimized using Lagrange multipliers. The function to be minimized, according to the constraints in Equation 5.26, is:

$$I_u = \sum_{i=0}^{N} \sum_{j=0}^{N} R_n[i,j] a_i a_j - \lambda \left( \sum_{i=0}^{N} a_i g[i] - 1 \right) - \kappa \sum_{i=0}^{N} a_i g'[i], \tag{5.28}$$

where $\lambda$ and $\kappa$ are the Lagrange multipliers. Setting $\frac{\partial}{\partial a_i} I_u = 0$ gives the following set of linear equations:

$$a_i = \lambda \sum_{j=0}^{N} R_n^{-1}[i-j] g[i] + \kappa \sum_{j=0}^{N} R_n^{-1}[i-j] g'[j], \tag{5.29}$$

where $R_n[i,j]$ is expressed as $R_n[i-j]$ since the electronic and pileup noise in the HEC are both stationary random processes. Combining Equations 5.26 and 5.29 gives $N+2$ independent equations from which the Lagrange multipliers and the OF coefficients that minimize the mean square of the total noise are calculated.

In order to calibrate the filter and calculate its coefficients, AREUS must determine $g[i]$ and $R_n[i]$. The ADC phase and analytical pulse shape are a priori known, which takes care of $g[i]$. The autocorrelation matrix of the noise is calculated on the first samples in a sequence of ADC samples where no signal is artificially injected, as described in the previous section, using time averages as described in Section 4.4.2.

### 5.6.2 Wiener Filter

The Weiner filter (WF) [81] is an alternative to the OF. It has previously been studied in the context of its possible use in the LAr calorimeter trigger readout, along with its extension, the Weiner filter with forward correction (WFFC) (see references [72, 73]). The Weiner filter attempts to reconstruct the sequence of energies deposited in a channel $E[n]$ without distinguishing between signal or pileup. It's ideal output to a normalized and sampled pulse shape $g[n]$ is thus $\delta[n-d_{WF}]$, where $d_{WF}$ is the delay on the output of the WF. However, the WF is a FIR filter, which can be thought of as a moving weighted average of its input. This means that if the input pulse shape integrates to zero, so does the filter's output; i.e., the WF cannot output an ideal delta Kronecker. It was determined that a variant of the WF for which the ideal response to the normalized and sampled pulse shape, $g[n]$, is a delta Kronecker followed by a sample at half value, $\delta[n-d_{WF}]+\frac{1}{2}\delta[n-1-d_{WF}]$, performed best in the HEC simulation at HL-LHC. This is called the WF with half-value post-peak. Its output in response to a sequence of ADC samples can be seen in Figure 5.11(a).

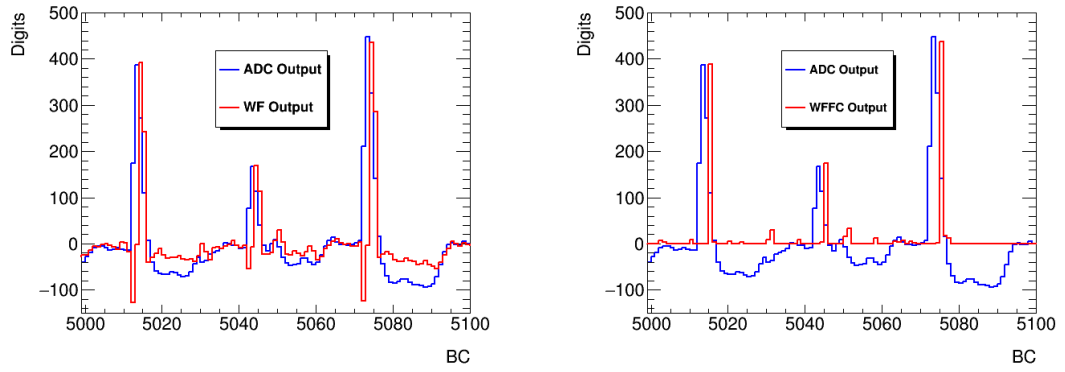


(a) (b)

Fig. 5.11 Example outputs of the ADC, (a) WF and (b) WFFC for three consecutive significant energy deposits with pileup condition $\langle\mu\rangle = 200$ in the HEC 1 at $\eta = 2.35$. Sequences are shown as a function of time (in units of bunch crossings).

#### Filter Coefficients

The WF coefficients $a_i$ are calculated in such a way that [81]:

$$\hat{E}[n] = \sum_{i=0}^{N-1} a_i x[n-i]. \tag{5.30}$$

Here, $x[n]$ is the input sequence to the filter, the output of the ADC on the FEB, and $\hat{E}[n]$ is an estimation of the desired sequence $E[n]$. The error on the output energy of the WF is calculated with respect to the actual energy deposited at sample $n$, $E[n]$:

$$e[n] = E[n] - \hat{E}[n] = E[n] - \sum_{i=0}^{N-1} a_i x[n-i]. \tag{5.31}$$

The mean square of this error is given by:

$$\begin{aligned}
\langle e^2[n] \rangle &= \langle (E[n] - \hat{E}[n])^2 \rangle \\
&= \langle (E[n] - \sum_{m=0}^{N-1} a_m x[n-m])^2 \rangle \\
&= \langle E^2[n] \rangle - 2 \sum_{m=0}^{N-1} a_m \langle E[n] x[n-m] \rangle + \sum_{m=0}^{N-1} \sum_{l=0}^{N-1} a_m a_l \langle x[n-m] x[n-l] \rangle \\
&= R_{EE}(0) - 2 \sum_{m=0}^{N-1} a_m R_{Ex}[m] + \sum_{m=0}^{N-1} \sum_{l=0}^{N-1} a_m a_l R_{xx}[l-m].
\end{aligned} \tag{5.32}$$

Here, $R_{EE}[n]$ is the autocorrelation function of the desired signal $E[n]$, $R_{Ex}[m]$ is the correlation function between the input samples $x[n]$ and the desired output $E[n]$, and $R_{xx}[n]$ is the autocorrelation function of the input samples $x[n]$. The WF attempts to minimizing the mean square of the error, giving:

$$\frac{\partial}{\partial a_m} \langle e^2[n] \rangle = 0 = \sum_{l=0}^{N-1} a_l R_{xx}[l-m] - R_{Ex}[m]. \tag{5.33}$$

The filter coefficients are thus derived from equation:

$$\sum_{l=0}^{N-1} a_l R_{xx}[l-m] = R_{Ex}[m]. \tag{5.34}$$

To calculate the coefficients, one must thus have knowledge of the autocorrelation function of the input samples and the correlation function between the input samples and desired output. Therefore, the WF requires calibration on signal as well as noise. This would require knowledge of the frequency and amplitude of energy deposits from physically interesting events. The dependency of the energy reconstruction algorithm on these predictions is undesired. Therefore, an approximation is done by neglecting electronic and pileup noise,

giving [72]:

$$R_{xx}(n) = \frac{1}{N}\sum_{n=0}^{N-1} g[n]g[n+m] \tag{5.35}$$

and

$$R_{Ex}[n] = \frac{1}{N}\sum_{n=0}^{N-1} \delta[n-d_{WF}]g[n+m] = g[m+d_{WF}]. \tag{5.36}$$

In this approximation, the WF coefficients does not depend on electronic or pileup noise but only on the normalized and sampled pulse shape of the HEC electronics. While this makes the WF incapable of minimizing noise on a channel by channel basis like the OF, its well defined output independent of noise conditions makes it easy to correct with an IIR extension.

### Forward Correction

The WFFC adds an energy identification algorithm and a forward correcting filter (see Figure 5.12). The energy identification algorithm only outputs a value if it detects a signal and if it does, the initial estimation of the energy from the WF is used to calculate a correction to its output. In so doing, the WFFC outputs only a single sample that approximates the energy deposition of a signal. The filter thus attempts to eliminate out-of-time pileup, making it less sensitive to signal in consecutive bunch crossings (see Figure 5.11(b)). It is therefore expected that this filter will perform best in channels where pileup noise dominates, as its extremely narrow output makes it very sensitive to thermal noise.

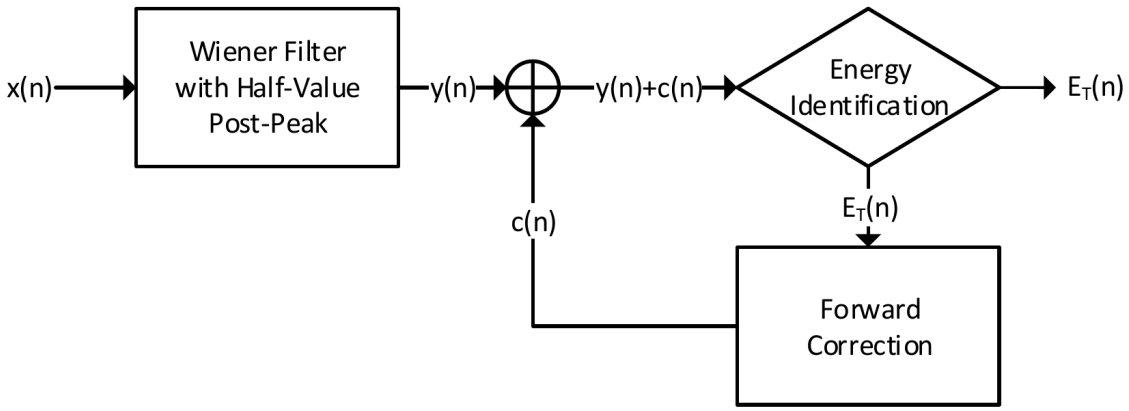


Fig. 5.12 Schematic diagram of the WFFC [72].

The feedback from the forward correction makes the WFFC an IIR filter. The stability of the filter in response to irregular (saturated or otherwise distorted) pulse shapes was previously studied. A set of criteria was developed to determine when the stability of the WFFC is compromised (see reference [72] and references therein), though this has yet to be tested on the HEC's readout chain. If an irregular output is detected, the forward correction filter is reset to prevent it from affecting following outputs.

### 5.6.3 Methodology for Calculating the Total Noise

From the filter analysis module in AREUS, correlation plots between the energy of a signal and the energy reconstructed by the filtering algorithms ($E_{s,in}$ and $E_{s,out}$ respectively) are used to determine the total noise at the output of the filter. Examples for the OF and the WFFC are shown in Figures 5.13(a) and 5.14(a) respectively.

An example of the result of projecting $E_{s,in}$ in different ranges onto the $y$-axis is shown in Figures 5.13(b) and 5.14(b). This gives the standard deviation of $E_{s,out} - E_{s,in}$ for a given signal energy range. The results of doing this for different pileup conditions and energy ranges are shown in Figures 5.13(c) and 5.14(c). The root mean square (RMS) of the noise is approximately constant as a function of signal energy, though it significantly worsens as pileup increases.

The energy reconstruction performance of the HEC electronic readout chain is evaluated by plotting the total noise ($\sigma(E_{s,out} - E_{s,in})$) versus $\langle\mu\rangle$. The total noise is that for the full signal energy range that is simulated ($0 < E_{s,in} \leq 50$ GeV). This gives a measure of the noise term $b$ of the energy resolution of the HEC (see Equation 3.8).

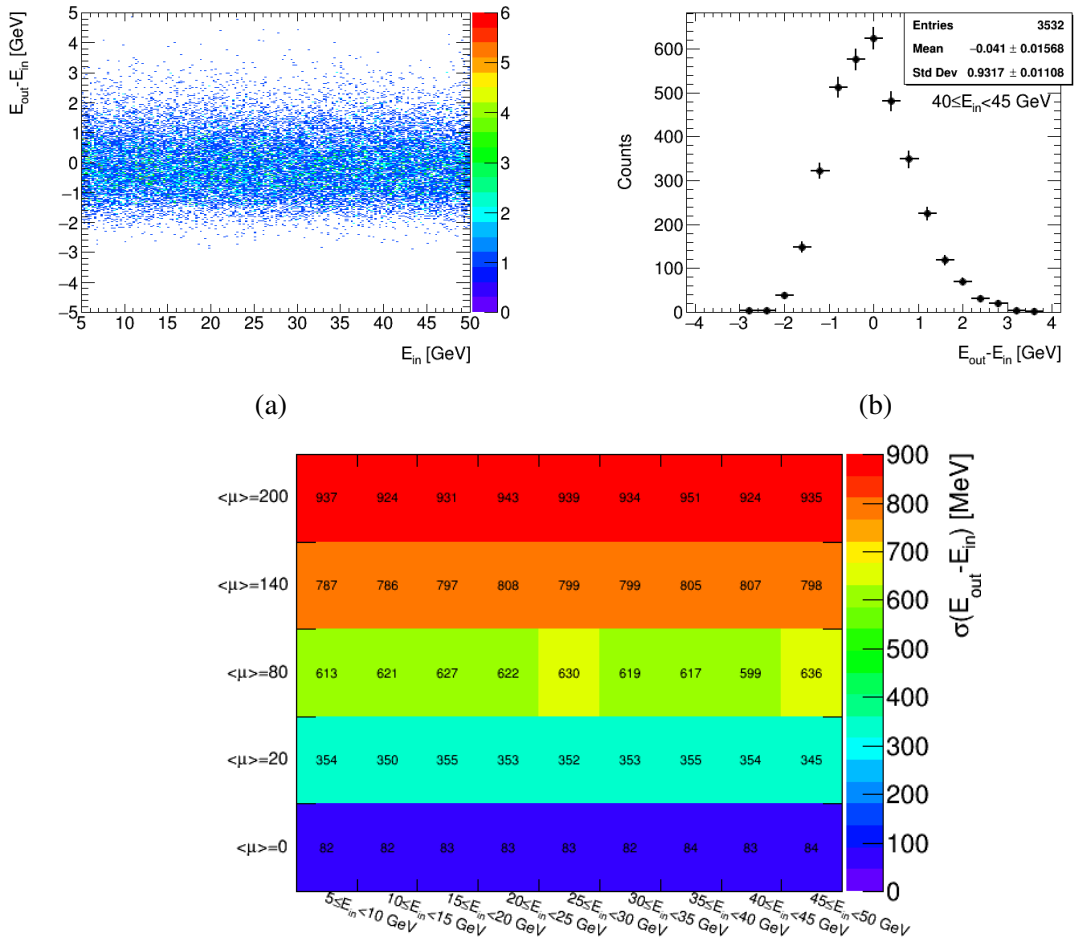


Fig. 5.13 Plots of the total noise at the output of the OF for the HEC channel located at $\eta = 2.35$ in layer HEC1. Figure (a) shows the correlation between $E_{out} - E_{in}$ and $E_{in}$ and (b) the projection of $40 \leq E_{in} < 45$ GeV onto $E_{out} - E_{in}$. Both are for $\langle\mu\rangle = 200$. Figure (c) shows the RMS of the noise as a function of pileup and input energy.

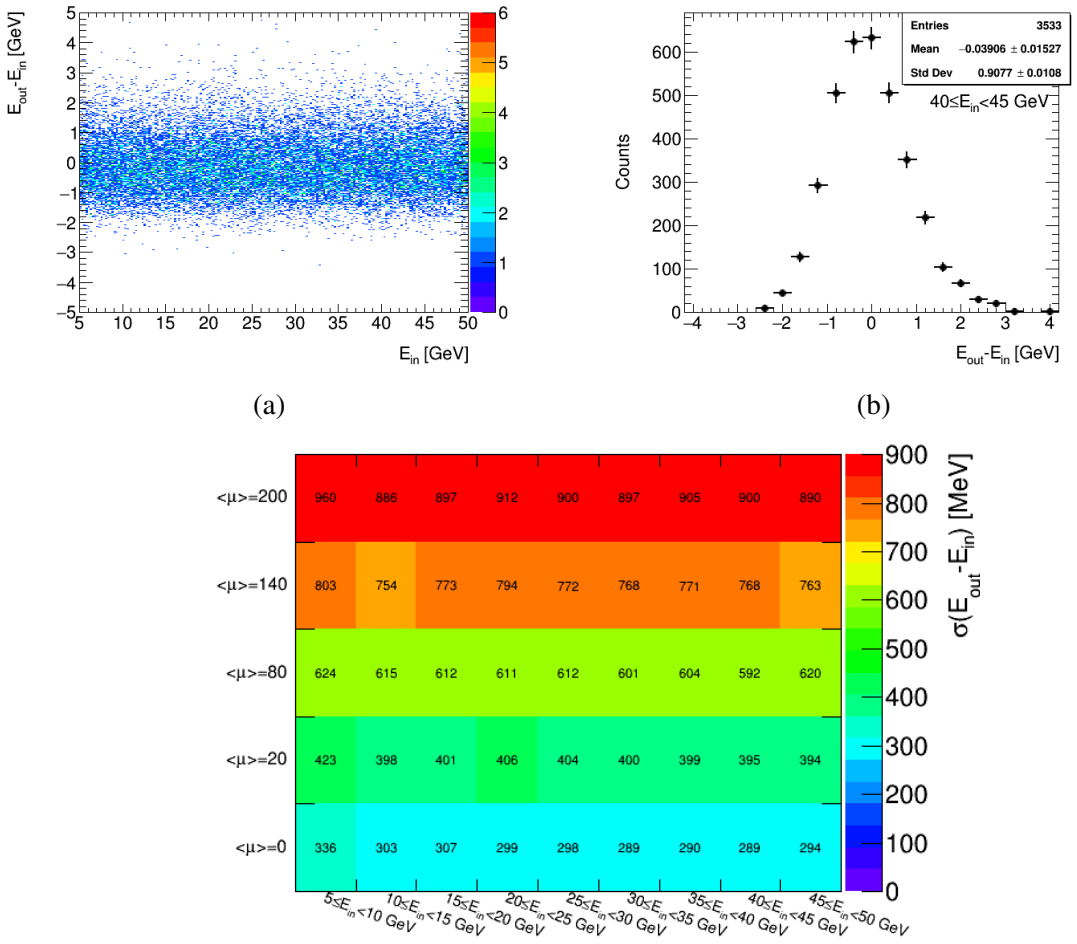


(a) (b)

(c)

Fig. 5.14 Plots of the total noise at the output of the WFFC for the HEC channel located at $\eta = 2.35$ in layer HEC1. Figure (a) shows the correlation between $E_{out} - E_{in}$ and $E_{in}$ and (b) the projection of $40 \leq E_{in} < 45$ GeV onto $E_{out} - E_{in}$. Both are for $\langle \mu \rangle = 200$. Figure (c) shows the RMS of the noise as a function of pileup and input energy.

# Chapter 6

# Performance and optimization of the HEC readout electronics at the HL-LHC

In this chapter, the AREUS simulation is used to test and optimize the performance of the HEC at HL-LHC. The main results obtained in this section were published in the ATLAS Liquid Argon Calorimeter Phase-II Upgrade Technical Design Report [63]. First, the current configuration of the HEC's readout chain is tested under different pileup conditions. Using the tools developed in the previous section, the different shapers and filtering algorithms will be tested along with the possibility of increasing the sampling rate of the ADC from 40 to 80 MHz.

## 6.1 Overview

In this subsection, the performance of the HEC is simulated without any changes to its electronics readout chain. This includes the current $CR-(RC)^2$ shaper with shaper constants $\tau_s = CR = RC = 13$ ns, a 12-bit ADC with an ENOB of 11.3, a sampling rate of 40 MHz and the OF with a filter depth of 5 samples. All results are shown for the medium gain signal path.

The response of the entire HEC calorimeter is simulated using ATLAS simulated di-jet events [1]. These simulated events also have a transverse momentum cut on the jets of $p_T > 2000$ GeV. Results for the simulation of the entire HEC calorimeter with $\langle\mu\rangle = 200$ are shown in Figure 6.1. Generally, the total noise increases from the front to the back layers,

[1] Final states of the proton-proton interactions resulting in at least two energetic jets of particles.

and also increases as a function of $\eta$, as expected.

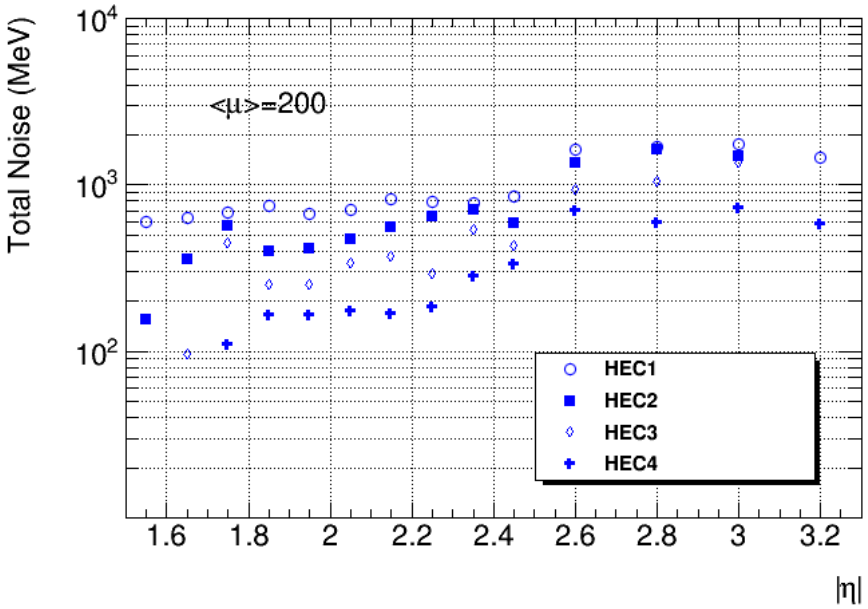


Fig. 6.1 Total noise in the HEC expected at the HL-LHC at an instantaneous luminosity of $\mathscr{L} = 7.5 \cdot 10^{34}$ cm$^{-2}$s$^{-1}$ with the current electronic readout.

This can be seen more clearly in Figure 6.2, where the total noise in a few representative channels in the HEC is shown for different pileup scenarios. Bins along the x-axis corresponds to simulations of the HEC readout under different pileup conditions, from no pileup ($\mu$=0) up to $\mu$=200. The total noise for each value of pileup considered is calculated using the reconstructed energy from an Optimal Filter who's coefficients (OFCs) were optimized for that specific pileup condition. Error bars on the total noise are included but appear smaller than the markers. The readout channels at pseudorapidities of 1.75, 2.35 and 2.8 in HEC layers 1, 2, 3 and 4 span the range of pileup versus electronic noise conditions in the HEC. At $\mu = 0$, only electronic noise is present. There is an approximate factor of two difference between the electronic noise in the front and back wheels due to the sampling fractions being twice as large in the front wheel. The readout channel in the HEC1 at $\eta = 2.8$ sees the most increase in total noise, by a factor of approximately 21 from $\mu = 0$ to $\mu = 200$, while the channel in the HEC4 at $\eta = 1.75$ sees virtually no change.

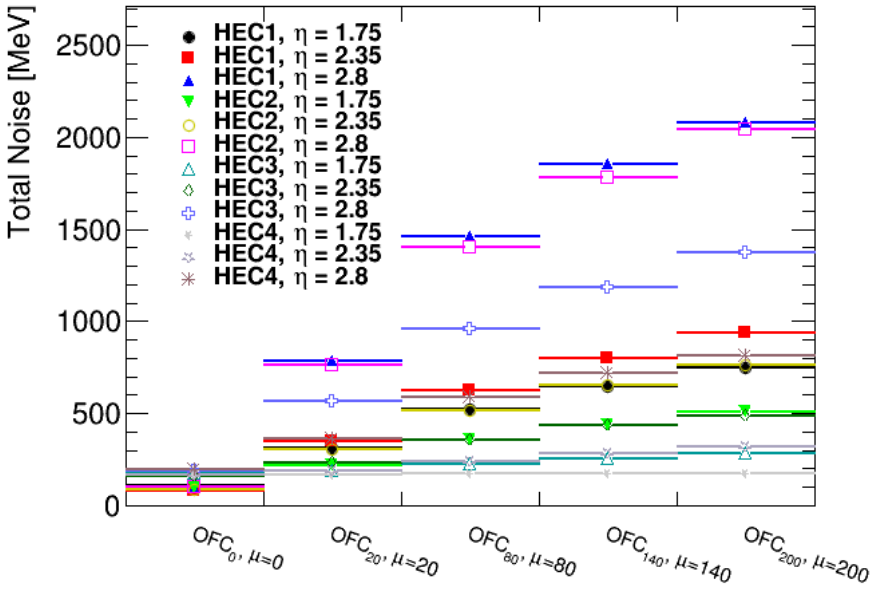


Fig. 6.2 Total noise as a function of pileup in 12 representative HEC readout channels.

## 6.2 Analog Shaping

The performance of the different configurations of the shaper discussed in Section 5.3 is presented here. The results for different shaper time constants are shown Figure 6.3. Figure 6.3(a) shows that in channels with high pileup, reducing the shaper's time constants from 13 to 8 ns can reduce the total noise by up to 5.5%; however, in readout channels where the electronics noise dominates (HEC3 and HEC4 at eta=1.75), a decrease in shaping time is shown to increase the total noise by up to 1.2% (see Figure 6.3(b)). This is expected as a shorter shaping time reduces pileup noise but increases the contribution of thermal noise to the total noise. In channels where thermal noise dominates, increasing the shaping time constants to 18 ns has no significant impact on the total noise when compared to a shaping time of 13 ns.

The results for different shapers are shown Figure 6.4. While removing an integration stage produces a narrower pulse shape (see Figure 5.3(b)), it only marginally improves total noise in channels where high pileup is expected (see Figure 6.4(a) at $\mu = 200$). This is due to the fact that removing an integration stage not only increases the bandwidth of the thermal noise's PSD, but also its RMS (see Figures 5.5 and 5.6). Conversely, Figure 6.4(b) shows that adding an integration stage leads to a reduction of the total noise by up to 28% in readout channels where the contribution from thermal noise is dominant.

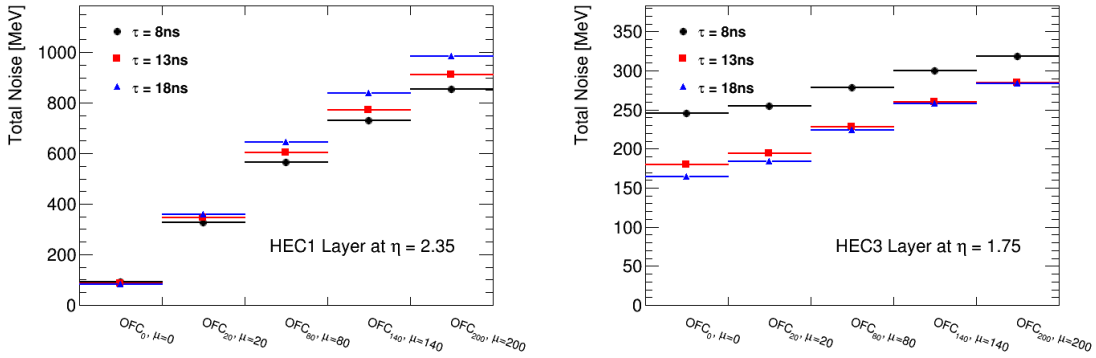


(a) (b)

Fig. 6.3 Comparison of the total noise as a function of pileup for different shaping time constants in a channel (a) dominated by pileup noise and (b) dominated by thermal noise at high pileup.

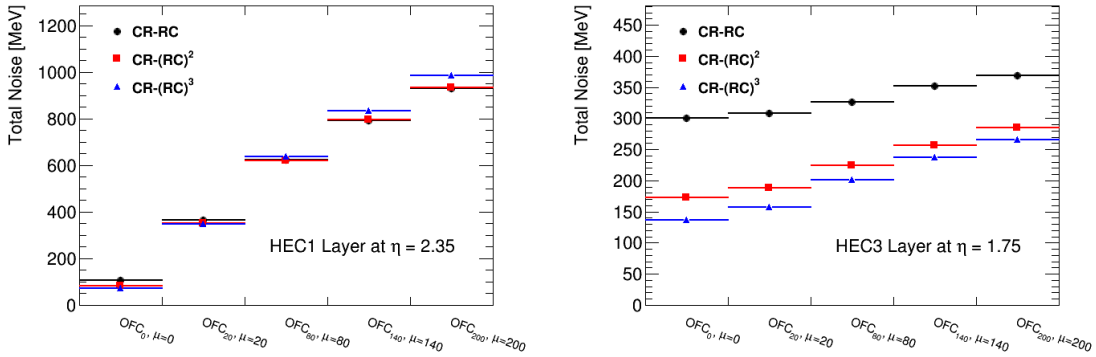


(a) (b)

Fig. 6.4 Comparison of the total noise as a function of pileup for different shaper circuits in a channel (a) dominated by pileup noise and (b) dominated by thermal noise at high pileup.

Reducing total noise in channels where thermal noise dominates is not as crucial to maintaining the current performance of the HEC at the expected instantaneous luminosity at the HL-LHC. The increase in luminosity has less effect on the total noise in these channels than those in the front layers and at higher $\eta$. The current plan for the Phase-II upgrade is to keep using the $CR-(RC)^2$ shaper with programmable shaping time to account for the large range of pileup versus thermal noise conditions not only in the HEC, but in the LAr calorimeter [63].

## 6.3 Sampling Rate

A higher sampling rate provides additional information about the pulse shape and the autocorrelation functions of the noise to the OF. It is thus expected to improve its performance when highly correlated noise, such as out-of-time pileup, is present. It also reduces aliasing of the thermal noise. To cover the entire width of the HEC's pulse shape, a filter depth of 10 samples is required instead of 5. A comparison of the total noise expected when sampling at 40 and 80 MHz is shown in Figure 6.5(a). An improvement of approximately 11% can be seen at $\mu = 200$ when increasing the sampling rate to 80 MHz. The benefits of increasing the sampling rate become more important at higher pileup.

Because of the aliasing of the thermal noise's PSD at a sampling rate of 40 MHz, high frequencies are added to the noise distribution at lower frequencies (see Figures 4.3 and 5.5). This further complicates the task of reducing the high frequency contribution of thermal noise by digital filters such as the OF. However, the PSD of the HEC's thermal noise is approximately band-limited to 40 MHz (see Figure 5.5), meaning that only negligible aliasing of the thermal noise is seen at a sampling rate of 80 MHz. Optimizing the shaping time of the HEC before the sampling is done is thus not as crucial. This is shown in Figure 6.5 when comparing the red points from (a) and (b), where (b) shows the result of doubling the sampling rate and reducing the shaping time to 8 ns in the same readout channel. While it was shown that reducing the shaping time to 8 ns decreased the total noise by 5.5% in this channel at a sampling rate of 40 MHz (see Section 6.2), a decrease of approximately 3% is seen here. In other words, the benefits of doubling the sampling rate and reducing the shaping time do not add linearly.

For the design of the new LAr electronics readout, it was decided that the relatively small improvement in total noise achieved with a higher sampling rate of 80 MHz did not justify the cost associated with a doubling of the bandwidth that would be necessary to implement this scenario.

## 6.4 Optimal Filter

In this section, the performance of the OF is tested. Figure 6.6(a) shows the performance of the OF when increasing its filter depth from 5 to 13 samples. It is expected that providing additional information on the pulse shape and autocorrelation functions of the noise will help

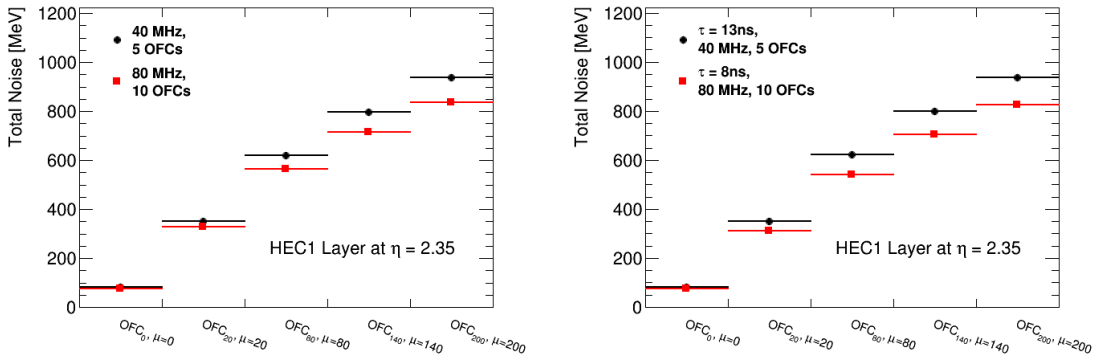


(a) (b)

Fig. 6.5 Comparison of total noise as function of pileup for (a) two different sampling rates using a shaping time of 13 ns and (b) two different sampling rates and shaper time constants.

the OF reduce the effects of out-of-time pileup. Indeed, increasing the filter depth from 5 to 9 provides increasing benefits as pileup increases, up to an improvement of 5% at $\mu = 200$, while increasing the filter depth from 9 to 13 provides no significant benefits in all cases.

The OF coefficients (OFCs) and its transfer function are highly dependent on the pulse shape and noise autocorrelation function. As such, as mentioned in the previous chapter, its coefficients are calculated based on the electronic and pileup noise conditions of each specific channel. However, the number of interactions per bunch crossing over the course of an LHC (or HL-LHC) fill is approximately Poisson distributed around $\langle\mu\rangle$ while the transfer function of the OF remains constant. The performance of the OF must thus be tested at high pileup with "fixed" coefficients to see if any significant degradation of its performance should be expected over the course of an HL-LHC fill. Figure 6.6(b) compares the performance of the OF as a function of $\mu$ in the case where its coefficients are fixed to those calculated on a sequence with $\mu = 140$ to the performance of the OF with coefficients specifically optimized for the pileup condition of each sequence. No significant increases in the total noise is observed when using the OF with fixed coefficients on sequences with $\mu = 80$ and $\mu = 200$ compared to the OF with "tuned" coefficients. For $\mu$ Poisson distributed around $\langle\mu\rangle = 140$, the probability that an interaction will have less than $\mu = 80$ or more than $\mu = 200$ is negligible.

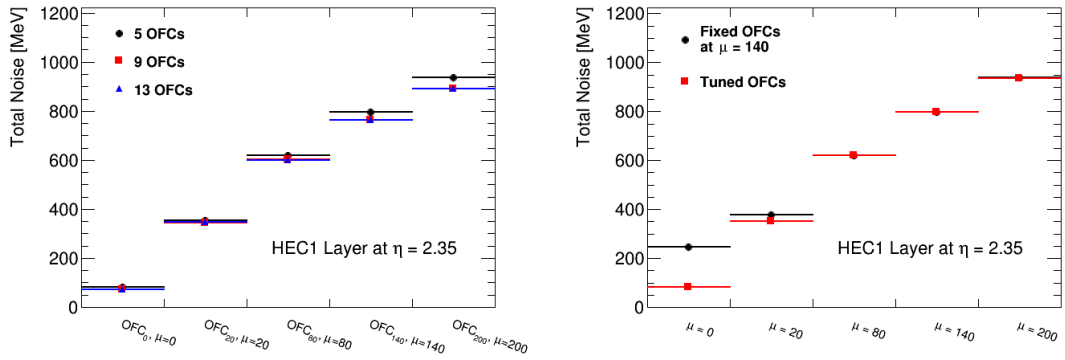


(a) (b)

Fig. 6.6 Comparison of total noise as a function of pileup for (a) various OF filter depths and (b) fixed versus tuned OFCs.

## 6.5 Weiner Filter with Forward Correction

The WFFC is designed to suppress out-of-time pileup by only outputting a sample when a signal is detected by its energy identification algorithm. If a signal is detected, it takes advantage of the well defined pulse shape of the WF by applying a forward correction which is fed back to the input and corrects for the negative undershoot of the pulse shape. As such, the WFFC is expected to performs best in channels dominated by pileup, as its narrow output makes it extremely sensitive to thermal noise. Figure 6.7(a) shows a comparison of the performance of the WFFC and the OF in a channel dominated by pileup at high $\mu$. At $\mu = 200$, the WFFC is shown to outperform the OF by 5%. Figure 6.7(b) shows the same comparison in a channel in the same layer but at slightly lower pseudorapidity where less pileup noise is expected. In this case, the WFFC achieves a comparable performance to the OF. Again, in the same layer but at even lower $\eta$, Figure 6.7(c) shows that the WFFC output has almost 17% more total noise than the OF.

The overall performance of the WFFC does not make it a viable option to be used for the energy reconstruction in the HEC calorimeter readout. However, it provides a proof of concept and valuable insights for the further development of potentially better performing digital filtering algorithms.

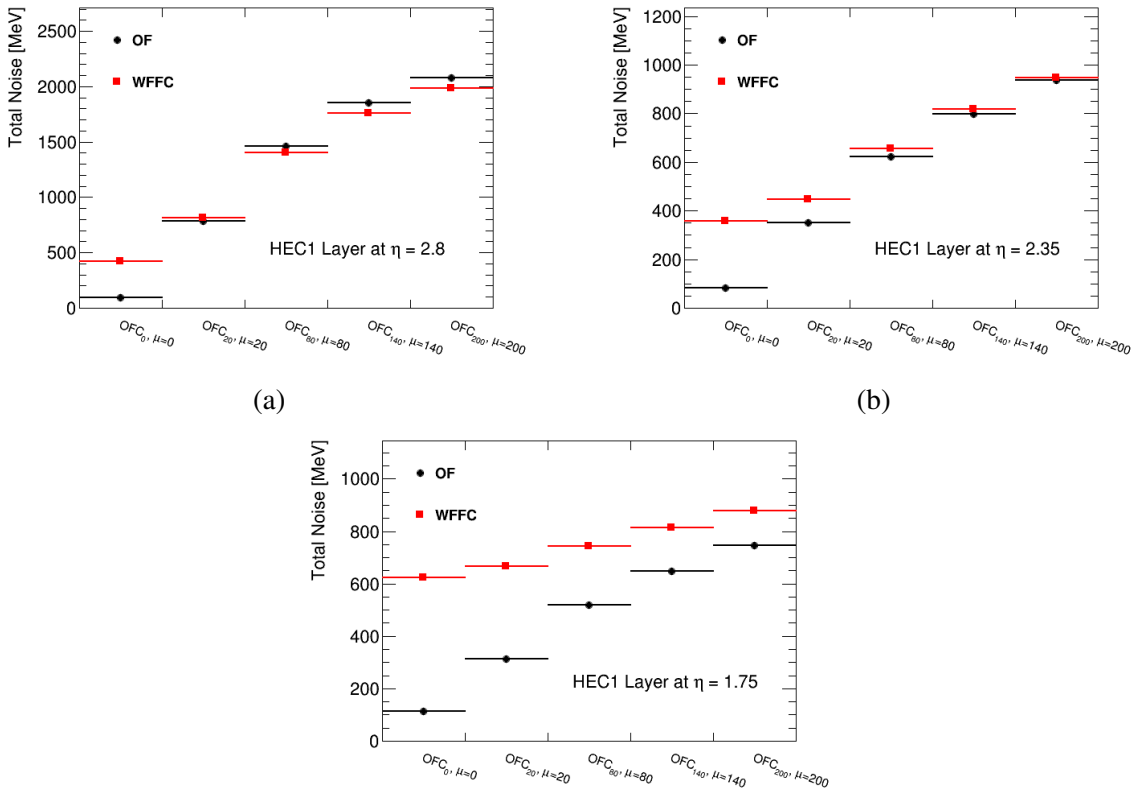


(a) (b)

(c)

Fig. 6.7 Comparison of total noise as a function of pileup for the OF and WFFC in different readout channels in the HEC1 layer at (a) $\eta = 2.8$, (b) $\eta = 2.35$, and (c) $\eta = 1.75$.

# Chapter 7

# Summary

The performance of the HEC readout electronics at the HL-LHC was simulated. In the analog electronics, a reduction of the total noise of up to 5.5% can be achieved in some readout channels where pileup noise dominates by reducing the shaper's time constants to 8 ns. Removing an integration stage in the shaper was shown to provide no significant benefits in channels where pileup noise dominates. The LAr calorimeter electronics readout at HL-LHC is therefore being designed using a $CR-(RC)^2$ shaper with programmable time constants. Doubling the sampling rate of the ADC provides an overall reduction in total noise of up to 11%, while shortening the shaping time in this scenario provides an additional reduction of up to 3% in readout channels with larger pileup noise contributions. While increasing the sampling rate improves the overall energy reconstruction performance of the HEC, it doubles the bandwidth needed to send the samples to the back-end electronics, increasing the total cost as well as technical complexity of the project. It is therefore expected that a sampling rate of 40 MHz will be kept for the phase-II upgrade of the LAr calorimeter electronics. On the digital filtering side, increasing the filter depth of the OF from 5 to 9 reduces total noise by up to 5%, while increasing it from 9 to 13 provides only marginal benefits. In addition, it was shown that the performance of the OF should be stable over the course of an HL-LHC fill. The WFFC was tested in the HEC's readout chain, showing a 5% reduction of the total noise when compared to the OF in channels where pileup noise dominates; however, it performs significantly worse in other channels.

Simulation studies presented in this thesis indicate that the energy reconstruction in the HEC at HL-LHC will worsen compared to the performance currently achieved at lower level of pileup. While the development and validation of the simulation is still ongoing, it is clear that any additional reduction of the total noise in the HEC readout electronics will

come from the digital filtering algorithms that can better suppress out-of-time pileup. The development of filters other than the ones discussed, such as the extended OF (described in references [82–84]), is already underway. The simulation of the HEC readout chain in AREUS provides a fast and flexible tool to develop and test the performance of these filters at the HL-LHC.

# Appendix A

# Maximum current expected in HEC preamplifiers at HL-LHC

As mentioned in Section 3.3.3, the maximum current at which the HEC cold preamplifiers are expected to behave linearly is 250 $\mu$A. However, information of the energy deposited at the cell level in the HEC is not readily available due to the summing of signals in the strip line connectors and the GaAs ASICs (see Section 3.2.3). In the GaAs ASIC drivers, four preamplified signals from layers HEC1, 3 and 4 or eight preamplified signals from layer HEC2 are summed to form a readout channel. If it is assumed that the ionization from an energy deposit in a channel is evenly distributed in the cells that make up a channel, a linearity range of 250 $\mu$A in the preamplifiers corresponds to a linearity range of 1 mA in the drivers of the HEC1, 3 and 4, and 2 mA in the drivers of the HEC2. This short study attempts to estimate the amount of nonlinear signals expected in the HEC at the HL-LHC by estimating the fraction of energy deposit that lead to ionization currents above 1 mA in a channel.

Official ATLAS simulated data consisting of di-jet events was chosen for this study as jets in the range of $1.5 < |\eta| < 3.2$ deposit most of their energy in the HEC. In addition, the di-jet production cross section is the second largest contributor to the total proton-proton interaction cross section (see Figure 2.2). While the single jet production cross section is higher, the transverse energy of jets coming from di-jet events is expected to be larger in the pseudorapidity range of the HEC as shown in Figure A.1. The di-jet simulation uses Pythia8 [76] as the event generator and Geant4 [77, 78] for the detector simulation. A cut of $p_T < 1400$ GeV is applied on the transverse momentum of the interacting partons and $p_T < 2000$ GeV on the jets. The dataset contains $\approx 400,000$ events giving $\approx 292$ fb$^{-1}$ of data,

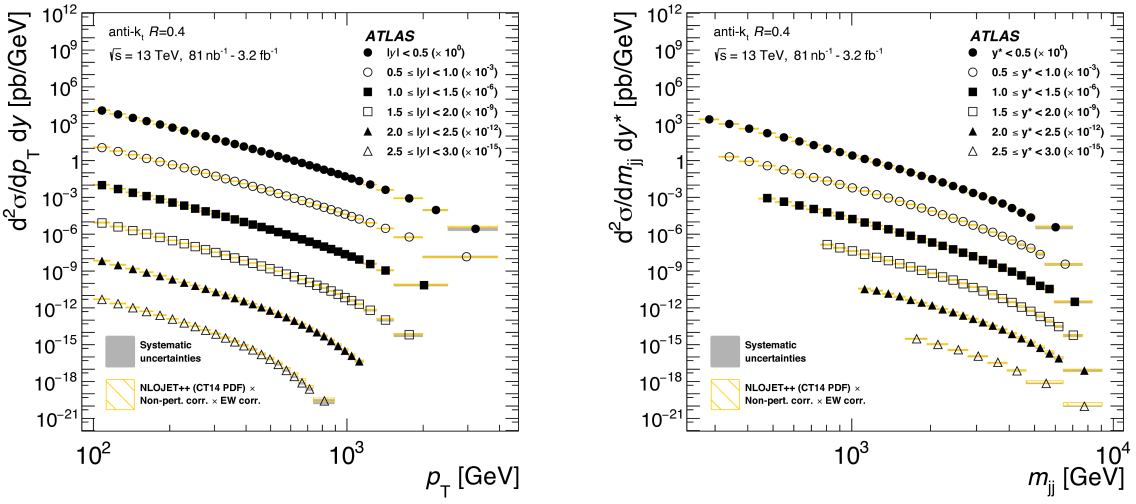


(a) (b)

Fig. A.1 Cross section measurements of proton-proton interactions with (a) one jet and (b) two jets in the final state as a function of transverse momentum $p_T$ and rapidity $|y|$ [85].

or approximately $^1/_{10}{}^{\text{th}}$ of the total dataset expected after 10 years of running at the HL-LHC.

The detector simulation gives the energy deposited by the di-jet events in a HEC channel, called detector "hits", which is then converted to current using Equation 3.5. The distribution of the ionization current is shown in Figure A.2 as a function of $\eta$ and $\phi$ in terms of the fraction of hits in the di-jet sample. As expected, Figure A.2(a) shows that the distribution is approximately flat as a function of $\phi$ while Figure A.2(b) shows that higher energies are deposited at lower $\eta$. The sharp rise in number of hits at $|\eta| = 2.5$ that is seen in Figure A.2(c) comes from the doubled $\Delta\eta$ size of the HEC readout pads at $|\eta| > 2.5$ (see Section 3.2.3).

In order to estimate the fraction of hits that are expected to lead to currents above 1 mA, fits are done to the current distributions in bins of $|\eta|$ where the fraction of hits is integrated in $\phi$ and $z$. The function used for the fit is:

$$f(x) = e^{p0+p1\cdot x} + e^{p2+p3\cdot x}, \tag{A.1}$$

where the fitting parameters are $p0$, $p1$, $p2$ and $p3$. The results for three $|\eta|$ bins are shown in Figure A.3 along with the parameters obtained, their uncertainties and the $\chi^2$ of the fit in terms of the number of degrees of freedom (ndf). Using the obtained fit parameters, the fitting function is integrated above 1 mA. The results are show in Figure A.4, giving the

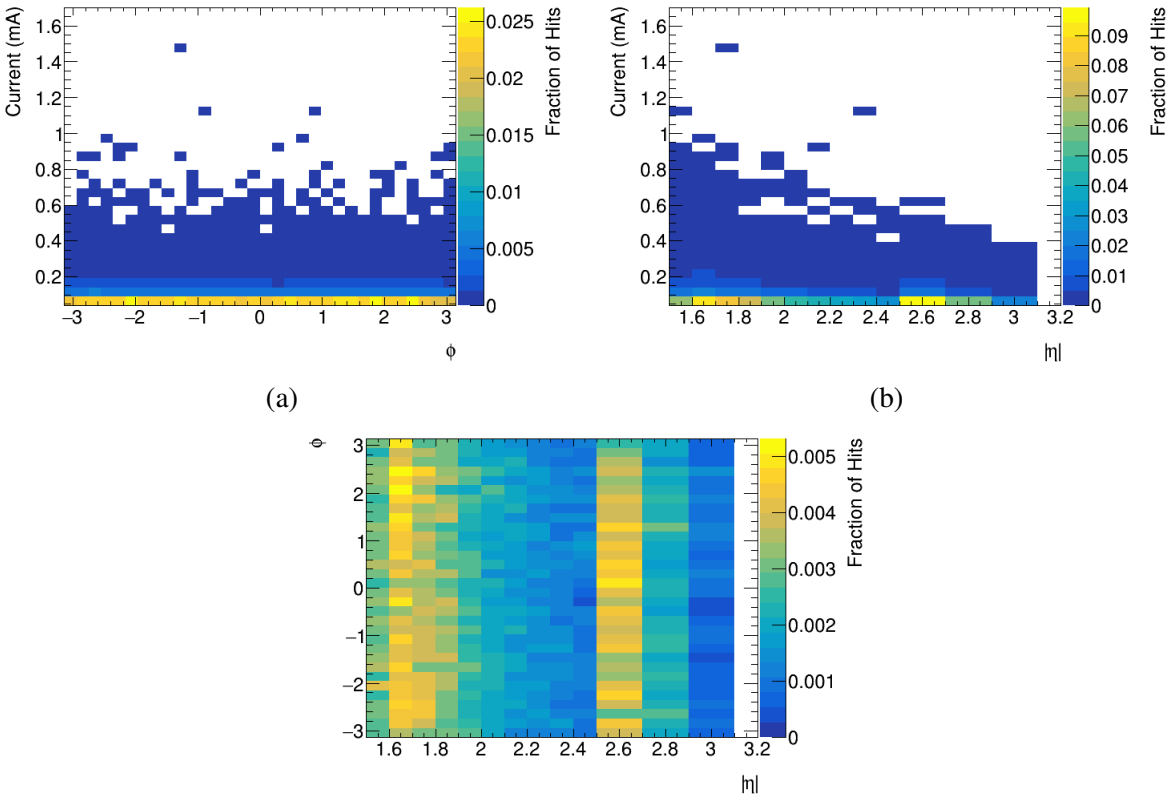


Fig. A.2 Fraction of di-jet event detector hits as a function of: (a) ionization current deposited in a HEC channel and $\phi$, (b) ionization current deposited in a HEC channel and $\eta$, and (c) $\phi$ and $\eta$.

fraction of di-jet event detector hits that lead to a current above 1 mA as a function of $|\eta|$.

Results show that overall, a fraction of less than $10^{-6}$ of di-jet detector hits should lead to currents that are high enough to cause non-linearity in the HEC's preamplifiers. This, along with the radiation hardness study discussed in Section 3.3.3, shows that the HEC preamplifiers should remain linear and operational over the course of the full data-taking period of the ATLAS detector at the the HL-LHC.

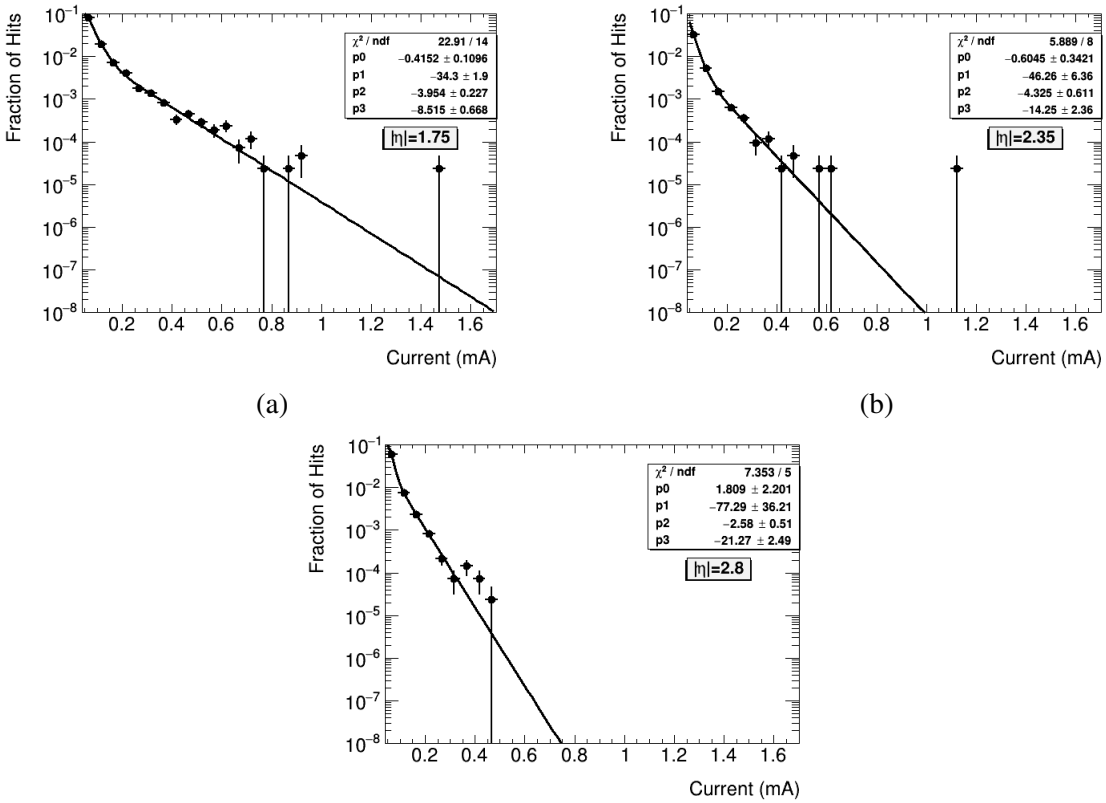


Fig. A.3 Fits to the distribution of ionization current deposited by di-jet event detector hits in three different $|\eta|$ bins.

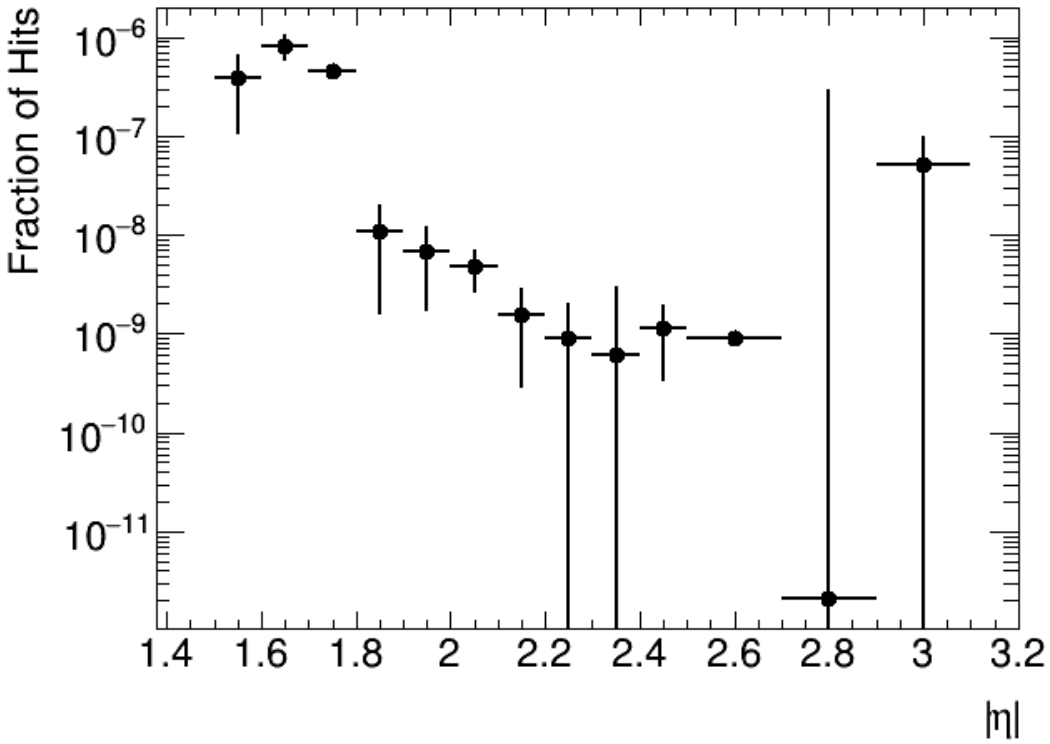


Fig. A.4 Fraction of di-jet event detector hits that lead to ionization currents above 1 mA in the HEC GaAs drivers as a function of $|\eta|$ regions.

# List of Terms an Abbreviations

| | |
|---|---|
| ADC | Analog to Digital Converter |
| ASIC | Application Specific Integrated Circuits |
| ATLAS | Formerly A Toroidal LHC ApparatuS |
| BC | Bunch Crossing |
| BSM | Beyond the Standard Model |
| CERN | Center for European Nuclear Research |
| CMS | Compact Muon Solenoid |
| CPU | Central Processing Unit |
| DSP | Digital Signal Processor |
| DTFT | Discrete-Time Fourier Transform |
| EF | Event Filter |
| EM | Electromagnetic |
| ENOB | Effective Number Of Bits |
| EYETS | Extended Year-End Technical Stop |
| FEB | Front-End Board |
| FIR | Finite Impulse Response |
| FPGA | Field-Programmable Gate Array |
| GaAs | Gallium Arsenide |

| | |
|---|---|
| GUT | Grand Unification Theory |
| HEC | Hadronic End-Cap |
| HL-LHC | High Luminosity Large Hadron Collider |
| HLT | High Level Trigger |
| IDTFT | Inverse Discrete-Time Fourier Transform |
| IIR | Infinite Impulse Response |
| IP | Interaction Point |
| L0 | Level-0 |
| L1 | Level-1 |
| L2 | Level-2 |
| LAr | Liquid Argon |
| LHC | Large Hadron Collider |
| LS1 | Long Shutdown 1 |
| LS2 | Long Shutdown 2 |
| LS3 | Long Shutdown 3 |
| LSB | Layer Summing Board |
| lsb | Least Significant Bit |
| LTI | Linear and Time-Invariant |
| PS | Proton Synchrotron |
| PSB | Preamplifying and Summing Boards |
| PSD | Power Spectral Density |
| QCD | Quantum Chromodynamics |
| RMS | Root Mean Square |

| | |
|---|---|
| ROD | Readout Driver |
| SM | Standard Model |
| SPS | Super Proton Synchrotron |
| TDB | Trigger Driver Board |

# List of figures

# List of tables

# References


[1] C. P. Burgess and G. D. Moore. *The Standard Model: A Primer*. Cambridge University Press, 2006.

[2] M. E. Peskin and D. V. Schroeder. *An Introduction to Quantum Field Theory; 1995 ed.* Westview, Boulder, CO, 1995.

[3] D. J. Griffiths. *Introduction to Elementary Particles; 2nd rev. version*. Physics textbook. Wiley, New York, NY, 2008.

[4] Brian R Martin and Graham Shaw. *Particle Physics*. John Wiley & Sons, 2017.

[5] F. Englert and R. Brout. Broken Symmetry and the Mass of Gauge Vector Mesons. *Physical Review Letters*, 13:321–323, Aug 1964.

[6] P. W. Higgs. Broken Symmetries and the Masses of Gauge Bosons. *Physical Review Letters*, 13:508–509, Oct 1964.

[7] G. S. Guralnik, C. R. Hagen and T. W. B. Kibble. Global Conservation Laws and Massless Particles. *Physical Review Letters*, 13:585–587, Nov 1964.

[8] P. W. Higgs. Broken Symmetries, Massless Particles and Gauge Fields. *Physics Letters*, 12(2):132 – 133, 1964.

[9] P. W. Higgs. Spontaneous Symmetry Breakdown without Massless Bosons. *Physical Review*, 145:1156–1163, May 1966.

[10] T. W. B. Kibble. Symmetry Breaking in Non-Abelian Gauge Theories. *Physical Review*, 155:1554–1561, Mar 1967.

[11] A. Purcell. Go on a particle quest at the first CERN webfest. Le premier webfest du CERN se lance à la conquête des particules. (BUL-NA-2012-269. 35/2012):10, Aug 2012.

[12] A. S. Kronfeld and C. Quigg. Resource Letter: Quantum Chromodynamics. *American Journal of Physics*, 78:1081–1116, 2010.

[13] M. L. Perl et al. Evidence for Anomalous Lepton Production in $e^+ - e^-$ Annihilation. *Physical Review Letters*, 35:1489–1492, Dec 1975.

[14] G. Arnison et al. Experimental observation of isolated large transverse energy electrons with associated missing energy at $\sqrt{s} = 540GeV$. *Physics Letters B*, 122(CERN-EP-83-13):103–116. 31 p, Jan 1983.

[15] G. Arnison et al. Experimental observation of lepton pairs of invariant mass around $95GeV/c^2$ at the CERN SPS collider. *Physics Letters B*, 126(CERN-EP-83-073):398–410. 17 p, Jun 1985.

[16] F. Abe et al. Observation of top quark production in $\bar{p}p$ collisions. *Physical Review Letters*, 74:2626–2631, 1995.

[17] G. Aad et al. Observation of a new particle in the search for the Standard Model Higgs boson with the ATLAS detector at the LHC. *Physics Letters B*, 716(arXiv:1207.7214. CERN-PH-EP-2012-218):1–29. 39 p, Aug 2012.

[18] S. Chatrchyan et al. Observation of a new boson at a mass of 125 GeV with the CMS experiment at the LHC. *Physics Letters B*, 716(CMS-HIG-12-028. CMS-HIG-12-028. CERN-PH-EP-2012-220):30–61. 32 p, Jul 2012.

[19] The ATLAS Collaboration. Summary plots from the ATLAS Standard Model physics group. March 2018.

[20] S. Abe et al. Precision Measurement of Neutrino Oscillation Parameters with KamLAND. *Physical Review Letters*, 100:221803, 2008.

[21] S. M. Bilenky and S. T. Petcov. Massive neutrinos and neutrino oscillations. *Reviews of Modern Physics*, 59(3):671, 1987.

[22] G. Bertone, D. Hooper and J. Silk. Particle Dark Matter: evidence, candidates and constraints. *Physics Reports*, 405(5):279 – 390, 2005.

[23] P. J. E. Peebles and N. Ratra. The cosmological constant and dark energy. *Reviews of Modern Physics*, 75:559–606, Apr 2003.

[24] H. M. Georgi and S. L. Glashow. Unity of all elementary-particle forces. *Physical Review Letters*, 32(8):438–441, 1974.

[25] L. Evans and P. Bryant. LHC Machine. *Journal of Instrumentation*, 3(08):S08001, 2008.

[26] K. A. Olive et al. Review of Particle Physics. *Chinese Physics*, C38:090001, 2014.

[27] The ALICE Collaboration. The ALICE experiment at the CERN LHC. *Journal of Instrumentation*, 3(08):S08002, 2008.

[28] The LHCb Collaboration. The LHCb Detector at the LHC. *Journal of Instrumentation*, 3(08):S08005, 2008.

[29] The ATLAS Collaboration. The ATLAS Experiment at the CERN Large Hadron Collider. *Journal of Instrumentation*, 3(08):S08003, 2008.

[30] The CMS Collaboration. The CMS experiment at the CERN LHC. *Journal of Instrumentation*, 3(08):S08004, 2008.

[31] The ATLAS Collaboration. ATLAS Luminosity Public results Run 1. March 2018.

[32] The ATLAS Collaboration. ATLAS Luminosity Public results Run 2. March 2018.

[33] J. Haffner. The CERN accelerator complex. Complexe des accélérateurs du CERN. Oct 2013.

[34] C.-Y. Wong. *Introduction to High-Energy Heavy-Ion Collisions*. World Scientific, Singapore, 1994. Erratum.

[35] The ATLAS Collaboration. ATLAS inner detector: Technical design report. Vol. 1. Technical report, 1997.

[36] The ATLAS Collaboration. ATLAS inner detector: Technical design report. Vol. 2. Technical report, 1997.

[37] The ATLAS Collaboration. ATLAS liquid-argon calorimeter: Technical Design Report. Technical report, Geneva, 1996.

[38] *ATLAS tile calorimeter: Technical Design Report*. Technical Design Report ATLAS. CERN, Geneva, 1996.

[39] The ATLAS Collaboration. ATLAS muon spectrometer: Technical design report. Technical report, 1997.

[40] The ATLAS Collaboration. ATLAS first level trigger: Technical design report. Technical report, 1998.

[41] P. Jenni, M. Nessi, M. Nordberg and K. Smith. ATLAS high-level trigger, data-acquisition and controls: Technical Design Report. Technical report, Geneva, 2003.

[42] A. Ruiz-Martinez on behalf of the ATLAS Collaboration. The Run-2 ATLAS Trigger System. Technical Report ATL-DAQ-PROC-2016-003, CERN, Geneva, Feb 2016.

[43] J. Bremer. The Cryogenic System for the ATLAS Liquid Argon Detector. (LHC-Project-Report-393. CERN-LHC-Project-Report-393):5 p, Jun 2000.

[44] L. Kurchaninov. Modeling of the HEC Electronics Chain. Technical Report ATLAS HEC Note-109, Max Planck Institute for Physics, Munich, Mar 2001.

[45] L. Kurchaninov. High Rate Effects in the ATLAS HEC Calorimeter. Technical Report ATLAS HEC Note-170, TRIUMF, Vancouver, Jul 2009.

[46] J. Thomas, D. A. Imel and S. Biller. Statistics of charge collection in liquid argon and liquid xenon. *Physical Review A*, 38:5793–5800, Dec 1988.

[47] J. Ban et al. Cold electronics for the liquid argon hadronic endcap calorimeter of ATLAS. In *IEEE Symposium Conference Record Nuclear Science 2004.*, volume 3, pages 1687–1691 Vol. 3, Oct 2004.

[48] H. Brettel, W. D. Cwienk, R. Huber, L. Kurchaninov, H. Oberlack, P. Schacht. QC Test of GaAs Preamplifier Chips. Technical Report ATLAS HEC Note-101, Max Planck Institute for Physics, Munich, Nov 2001.

[49] E. Ladygin[1], W.-D. Cwienk, L. Kurchaninov, P. Strizenec. Preshaper for the Hadronic End-Cap Calorimeter. Technical Report ATLAS HEC Note-124, Joint Institute for Nuclear Research[1] & Max Planck Institute for Physics, Dubna[1] & Munich, Mar 2002.

[50] A. Bazan et al. ATLAS liquid argon calorimeter back end electronics. *Journal of Instrumentation*, 2(06):P06002, 2007.

[51] N. J. Buchanan et al. ATLAS liquid argon calorimeter front end electronics. *Journal of Instrumentation*, 3(09):P09003, 2008.

[52] J. B. Johnson. Thermal Agitation of Electricity in Conductors. *Physical Review*, 32:97–109, Jul 1928.

[53] H. Nyquist. Thermal Agitation of Electric Charge in Conductors. *Physical Review*, 32:110–113, Jul 1928.

[54] D. Gabor. Theory of communication. Part 1: The analysis of information. *Electrical Engineers - Part III: Radio and Communication Engineering, Journal of the Institution of*, 93(26):429–441, November 1946.

[55] G. Apollinari, O. Brüning, T. Nakamoto and L. Rossi. Chapter 1: High Luminosity Large Hadron Collider HL-LHC. High Luminosity Large Hadron Collider HL-LHC. *CERN Yellow Report*, (arXiv:1705.08830. 5):1–19. 21 p, May 2017.

[56] A. Hoecker. Physics at the LHC Run-2 and Beyond. (arXiv:1611.07864):153–212. 61, Nov 2016.

[57] The ATLAS Collaboration. Physics at a High-Luminosity LHC with ATLAS. In *Proceedings, 2013 Community Summer Study on the Future of U.S. Particle Physics: Snowmass on the Mississippi (CSS2013): Minneapolis, MN, USA, July 29-August 6, 2013*, 2013.

[58] The ATLAS Collaboration. Letter of Intent for the Phase-I Upgrade of the ATLAS Experiment. Technical Report CERN-LHCC-2011-012. LHCC-I-020, CERN, Geneva, Nov 2011.

[59] The ATLAS Collaboration. ATLAS Phase-II Upgrade Scoping Document. Technical Report CERN-LHCC-2015-020. LHCC-G-166, CERN, Geneva, Sep 2015.

[60] N. J. Buchanan et al. Radiation qualification of the front-end electronics for the readout of the ATLAS liquid argon calorimeters. *Journal of Instrumentation*, 3(10):P10005, 2008.

[61] F. Ahmadov. Upgrade plans for the Hadronic-Endcap Calorimeter of ATLAS for the high luminosity stage of the LHC. Technical Report ATL-LARG-PUB-2015-001, CERN, Geneva, Jul 2015.

[62] H. Oberlack et al. Upgrade of the cold electronics of the ATLAS HEC calorimeter for sLHC generic studies of radiation hardness and temperature dependence. In *2009 IEEE Nuclear Science Symposium Conference Record (NSS/MIC)*, pages 758–762, Oct 2009.

[63] The ATLAS Collaboration. Technical Design Report for the Phase-II Upgrade of the ATLAS LAr Calorimeter. Technical Report CERN-LHCC-2017-018. ATLAS-TDR-027, CERN, Geneva, Sep 2017.

[64] M. Aleksa et al. ATLAS Liquid Argon Calorimeter Phase-I Upgrade Technical Design Report. Technical Report CERN-LHCC-2013-017. ATLAS-TDR-022, Sep 2013.

[65] A. V. Oppenheim, A. S. Willsky and S. H. Nawab. *Signals &Amp; Systems (2Nd Ed.)*. Prentice-Hall, Inc., Upper Saddle River, NJ, USA, 1996.

[66] A. Papoulis. *Signal analysis*. McGraw-Hill Electrical and Electronic Engineering Series. McGraw-Hill, 1977.

[67] A. V. Oppenheim and R. W. Schafer. *Discrete-Time Signal Processing*. Pearson Education, 2011.

[68] J. Bird. *Electrical Circuit Theory and Technology; 5th ed.* Routledge, London, 2014. SI units used.

[69] H. Nyquist. Certain Topics in Telegraph Transmission Theory. *Transactions of the American Institute of Electrical Engineers*, 47(2):617–644, April 1928.

[70] C. E. Shannon. Communication in the Presence of Noise. *Proceedings of the IRE*, 37(1):10–21, Jan 1949.

[71] J. P. Grohs and S. Stärz. AREUS. Technical Report ATL-LARG-INT-2014-003, CERN, Geneva, Jul 2014.

[72] J. P. Grohs and A. Straessner. *Simulation of the upgraded Phase-1 Trigger Readout Electronics of the Liquid-Argon Calorimeter of the ATLAS Detector at the LHC*. PhD thesis, Jun 2015.

[73] S. Stärz and A. Straessner. *Energy Reconstruction and high-speed Data Transmission with FPGAs for the Upgrade of the ATLAS Liquid Argon Calorimeter at LHC*. PhD thesis, Feb 2015.

[74] B. Dowler et al. Performance of the ATLAS Hadronic End-Cap Calorimeter in Beam Tests. Technical Report ATL-LARG-2001-019, Max-Planck Inst., München, Oct 2001.

[75] Wolfram Research, Inc. Mathematica, Version 11.3. Champaign, IL, 2018.

[76] R. Ciesielski and K. Goulianos. MBR Monte Carlo Simulation in PYTHIA8. Technical Report arXiv:1205.1446, May 2012.

[77] S. Agostinelli et al. Geant4—a simulation toolkit. *Nuclear Instruments and Methods in Physics Research Section A: Accelerators, Spectrometers, Detectors and Associated Equipment*, 506(3):250 – 303, 2003.

[78] G. Aad et al. The ATLAS Simulation Infrastructure. *The European Physical Journal C*, 70(3):823–874, Dec 2010.

[79] A. Kiryunin, L. Kurchaninov, P. Stavina. Reconstruction of Signal Parameters in the HEC Readout Driver. Technical Report ATLAS HEC Note-110, Max Planck Institute for Physics, Munich, Mar 2001.

[80] W. E. Cleland and E. G. Stern. Signal processing considerations for liquid ionization calorimeters in a high rate environment. *Nuclear Instruments and Methods in Physics Research Section A: Accelerators, Spectrometers, Detectors and Associated Equipment*, 338(2):467 – 497, 1994.

[81] N. Wiener. *Extrapolation, interpolation, and smoothing of stationary time series: with engineering applications*. MIT, Cambridge, MA, 1949.

[82] H. Xu, D. Gong and Y. Chiu. On the performance of linear optimal filter and Wiener filter for signal detection in liquid ionization calorimeters. In *2014 IEEE Nuclear Science Symposium and Medical Imaging Conference (NSS/MIC)*, pages 1–6, Nov 2014.

[83] L. M. de A. Filho, B. S. Peralva, J. M. de Seixas and A. S. Cerqueira. Calorimeter Response Deconvolution for Energy Estimation in High-Luminosity Conditions. *IEEE Transactions on Nuclear Science*, 62(6):3265–3273, Dec 2015.

[84] R. Iguchi, Y. Enari and K. Uno and J. Tanaka. Development of New Optimal Filter for Future High Luminosity Environment. Technical Report ATL-COM-LARG-2017-015, CERN, Geneva, May 2017.

[85] M. Aaboudet al. Measurement of inclusive jet and dijet cross-sections in proton-proton collisions at $\sqrt{s} = 13$ TeV with the ATLAS detector. *Journal of High Energy Physics*, 2018(5):195, May 2018.